Chapter 1
Introduction

The past few decades have seen a significant reduction in jet noise due to adoption of high-by-pass ratio turbofan engines. Airframe noise sources such as high-lift devices and landing gear are seen as major contributors to the overall fly-over noise signature during approach due to turbofan engines operating at low thrust. With further improvement in engine technology due to the adoption of even higher-by-pass ratio turbofan engines, the contribution of noise from the air-frame is expected to be more significant. Also, aviation authorities in United States, Europe and Japan are imposing stricter regulations that require reduction in noise. In Europe, where many cities have grown and surround airports, aircraft noise is a major concern and noise reduction technology is being actively pursued. In the United States, government sponsored past and current programs such as STAR (Subsonic Transportation Aeroacoustic Research), QAT (Quiet Airframe Technologies), RAIN (Reduction of Airframe and Installation Noise), AST (Advanced Subsonic Technology), QTD (Quiet Technology Demonstrator) and more recently QTD II have been undertaken to reduce airframe noise.

1.1 Background and Motivation

The gear noise signature has a spectral peak at mid to low frequencies [1] and is considered to be a dominant airframe noise source for modern aircrafts such as Boeing 777. Flow over large elements corresponds to noise at lower frequency while high frequency noise corresponds to small components. Most of the high frequency noise can be reduced either by streamlining or by shielding the small elements from high flow areas. The wheels were considered to be a major source of gear noise due to the large diameter and the inability to streamline them [2]. Heller [3-5] shows that multiple-wheel-set configurations are noisier than single-wheel-set configurations. Several experiments conducted in the German-Dutch Wind Tunnel point out to the possibility of the tire-wake/tire interaction or the developed flow structure over the wheels being a significant

noise producer. Lazos [10-12] used a 31% scaled model of the four wheel Boeing 757 landing gear with zero degrees truck angle in the Basic Aerodynamics Research Tunnel at NASA Langley Research Center. Digital Particle Image Velocimetry measurements were acquired over the wheels of the gear at a Reynolds number based wheel diameter of 600,000. The tire-wake/tire interaction was clearly visible and a mid wheel vortex was discovered changing stream-wise location. The translating motion of the vortex and its rubbing with the wheels was considered to be a noise source for noise radiated towards the ground side.

In the past, aircraft landing gears were often lumped together as a single component, while in reality they consists of a number of wheels, struts, braces, lock links, hydraulic lines, brake components, etc. Research conducted on landing gears to identify various noise sources used scale models of isolated landing gears in a wind tunnel. The landing gear stripped of its small components such as oleo lines, hydraulic cylinders, cable harness, gear door, etc. is considered to be a low fidelity model and is shown in Figure 1.1. The fully dressed landing gear which includes all the small components (made using stereo-lithography up to an accuracy of 3mm) is called as a high fidelity model and is shown in Figure 1.2. Stoker and Sen [6] conducted an airframe noise investigation of a 0.063 scale Boeing 777 model using different main gear configurations (high and low fidelity models) and found that main high-fidelity landing gear was a significant contributor to airframe noise at higher frequencies as compared to a low fidelity model. Flow survey of an isolated 777 main landing gear wake was conducted by Horne et al. [7] to investigate the gear aerodynamics in the NASA Ames 7- by 10- foot wind tunnel. Pitot-static pressure measurements along with hot-wire turbulence measurements were taken to understand the change in flow using two different gear configurations (namely high and low fidelity models). Experimental results proved that high fidelity landing gear model showed wake region deficit of total pressure and velocity to be twice as compared to the low fidelity model. Although maximum turbulence intensity levels were comparable, it was considered necessary to test the high-fidelity landing gear in the future for accurate results.

Figure 1.1: Low Fidelity 26% Scale Model of the 777 Main Landing Gear (Truck Angle = 0 deg.)

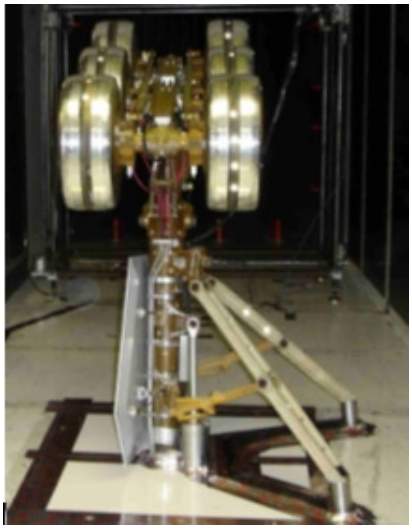

Figure 1.2: High Fidelity 26 % Scale Model of the 777 Main Landing Gear (Truck Angle = 13 deg.)

Aeroacoustic tests were conducted on a 26% high-fidelity 777 main landing gear in the Virginia Tech Stability Wind Tunnel (VT-SWT). The purpose of the investigation was to identify and reduce the major noise sources. For this purpose, Microphone phased array technology was developed at Virginia Tech [8] and by using them individual noise sources were identified and their individual contribution to the overall noise was quantified.

Ravetta [9] introduced the concept of elastic membrane based fairings called Noise Control Devices (NCD) to reduce noise by either shielding elements of the gear from higher flow speeds or by reducing wake interactions. Noise Control Devices were applied to three different locations, namely: strut fairings, braces fairings and truck fairings and are shown with the high fidelity 26 % landing gear in Figure 1.3. Noise Control Devices were tested and satisfactory results in terms of noise reduction were obtained.

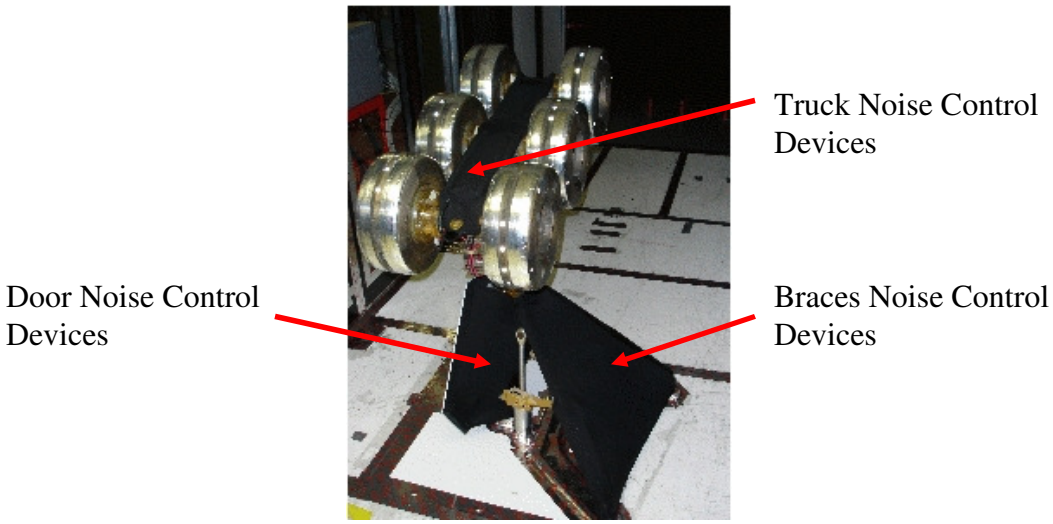

Figure 1.3: High Fidelity Model of the 777 Landing Gear showing Noise Control Devices (NCD)

To correlate reduction in noise from the landing gear to changes in flow (due to NCD), aerodynamic measurements such as hot-wire anemometry and Pitot-static pressure measurements in the wake of the landing gear and flow visualization using tufts over the landing gear were conducted. PIV measurements were also conducted as a part of this investigation to understand the interaction of the flow with the gear elements.

The primary objective of this investigation is to understand the fluid interactions between the gear elements (braces, wheels, etc) and to understand changes in flow due to Noise Control Devices. Some of the secondary objectives include; compare baseline results for high fidelity landing gear with the NASA Ames study, to quantify and relate the flow measurements to acoustic measurements for the high fidelity landing gear model with and without Noise Control Devices (NCD) and to compare PIV results with NASA Langley

results presented by Lazos [10-12]. For the first time, flow visualization using tufts was performed to help visualize the flow over the entire landing gear. Tufts were also used over NCD to have some idea about the effectiveness of the Noise Control Devices.

The report explains the experimental set-up, data reduction and results from each experiment performed over the scaled landing gears. Hot-film and Pitot-static measurements are discussed first, followed by flow visualization using tufts, and finally PIV measurements over selected planes are explained to give a general idea of the flow field and relate it to acoustic results.

Chapter 2
Experimental Setup

Time resolved PIV measurements were taken at six different planes over the 13% semi-high fidelity landing gear without the gear door at a truck angle of 0 degrees. Hot-film anemometry and Pitot-static probe measurements along with flow visualization using tuft were made on the 26% high fidelity landing gear at a truck angle of 13 degrees. The experimental setup for each of the above mentioned tests are explained in this chapter along with a brief overview of the experimental facility.

2.1 Wind Tunnel Test Facility

Aerodynamic measurements were performed on the main landing gear at the Virginia Tech Stability Wind Tunnel (VT-SWT) to have a better understanding of the flow around the landing gear and relate it to acoustic measurements. The subsonic tunnel shown in Figure 2.1 is a continuous closed loop facility, housing a 24 ft long and 6- by 6-ft wide test section, powered by a 600 hp DC motor and capable of reaching maximum speeds of Mach 0.23. The motor drives air through an air exchange tower and then through an 18- by 18-ft settling chamber which employs seven anti-turbulence screens. The anti-turbulence screens each have an open area ratio of 0.6 and are separated by 6 inches from each other. The exiting flow is accelerated before entering the test section using a 9:1 contraction. The dense anti-turbulence screens and the contraction result in uniform velocity and low turbulence intensity (less than 0.05 %) in the test section. The facility was capable of reaching maximum speeds of Mach 0.16 and 4% blockage with a baseline 26% high fidelity landing gear model.

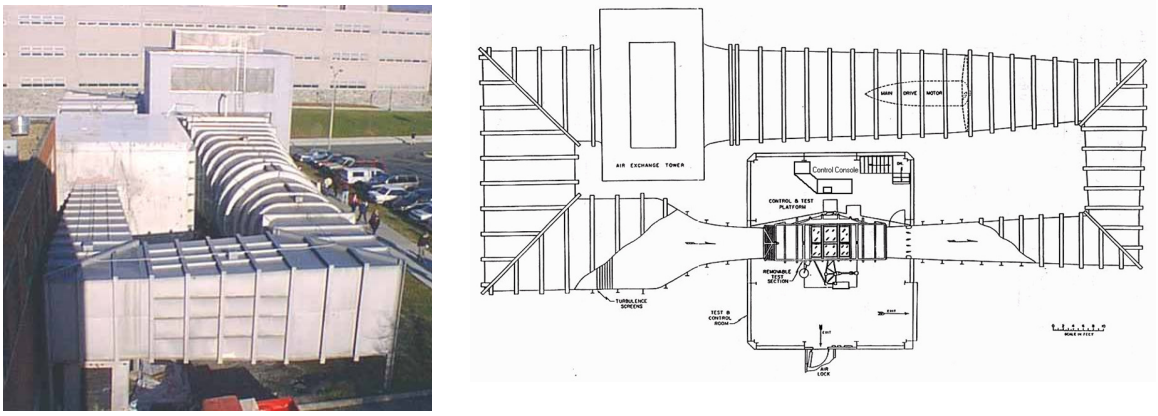

Figure 2.1: Virginia Tech Stability Tunnel

2.2 Test Configurations

During landing approach the Boeing 777 main landing gear typically operates at an angle of 13 degrees with front wheels closest to the ground while back wheels closest to the wings. This typical approach setting is of utmost importance for testing purposes and the gear is referred to as having a truck angle of 13 degrees. Sometimes, an alternate setting in which the wheels are parallel to the ground is used and the gear is referred to as having a truck angle of 0 degrees. This alternate setting is used with low fidelity models or to understand simple fluid / acoustic interactions with the parallel wheels.

Two configurations of the 26% landing gear were tested and measurements were taken with hot-film, Pitot-probe and flow visualization using tuft. The fully dressed (high fidelity) landing gear model (as shown in Figure 2.2) with a truck angle of 13º (front wheels closest to wing) was called as 'Baseline'. The second configuration used the same landing gear but involved the use of all the noise control devices (NCD); in the truck region, the brace region and around the main strut and door. Figure 2.3 shows the landing gear with all three NCD installed in the Virginia Tech Stability Wind Tunnel (VT-SWT). Flow visualization was accomplished by using tuft over the landing gear for both the baseline and NCD configurations at Mach 0.17.

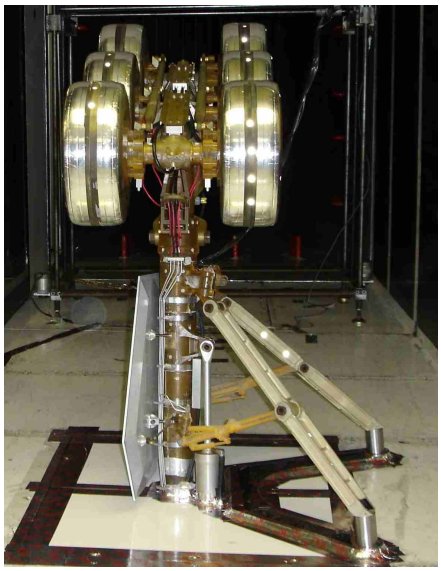

Figure 2.2: 26% High Fidelity Landing Gear (Baseline Configuration) in the VT-SWT

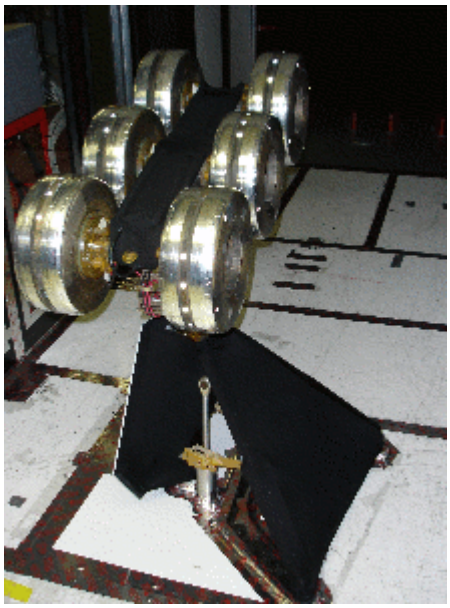

Figure 2.3: 26% High Fidelity Landing Gear (NCD Configuration) in the VT-SWT

For ease of comparison with the NASA Ames study, hot-film anemometry and Pitot-static pressure data were taken at a plane 64 inches downstream from the main strut of the landing gear. The distance was equal to sixteen times the main strut diameter (4 inches) where Horne et al. [7] noticed that the turbulence was diffused (isotropic). The grid

resolution for hot-film and Pitot-static probe was 2- by 1-inch and the dimensions of the scanning grid was 45- by 47-inch.

2.3 Hot-film Measurements

Time resolved velocity measurements were performed using a single sensor hot-film probe in the wake of the 26% landing gear. Hot-film anemometry measurements were performed to characterize the turbulence levels and look at the changes in levels of turbulence with and without the NCD. Also, mean velocity measurements can be calculated from the data. A novel technique of reducing hot-film data as acoustic data to compare with Microphone Phased-Array (MPA) results was developed and will be explained in the next chapter.

2.3.1 Anemometer Probe Design and Setup

A TSI 1201-20 disposable hot-film probe was used for hot-film anemometry measurements. It had a cylindrical Platinum wire as the sensing element having diameter of 50.8 μm. The length of the sensing area was 1.02 mm and the supports were 1.65 mm apart. The maximum allowable ambient temperature was 150^{o}C and the recommended maximum sensor operating temperature was 425^{o}C (from TSI catalog, [17]). Figure 2.4 shows a schematic of the probe used.

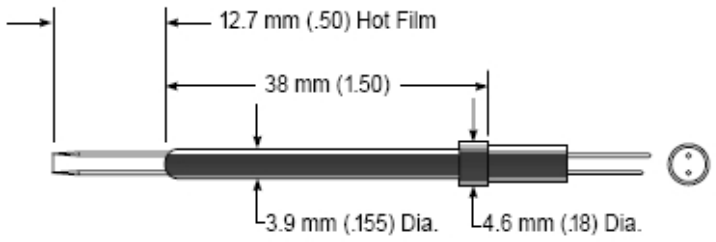

Figure 2.4 Model 1201 Cylindrical Hot-film Probe

The hot-film probe was mounted on a 14 in. long probe holder (shown in Figure 2.5) in such a way that the sensing element (film) was parallel to the ground. The probe support was held by a small fixture which was connected to a 1m long hollow square aluminum

cylinder. The aluminum cylinder was attached to a traverse which was placed downstream of the landing gear. The entire assembly (consisting of the traverse, the probe support and the probe) was placed in such a way that the hot-film sensing element could be traversed along a plane which was 64 inches downstream of the main strut. The traverse was secured firmly in the tunnel and care was taken to keep the measurement plane perpendicular to the flow and the tunnel walls during operation.

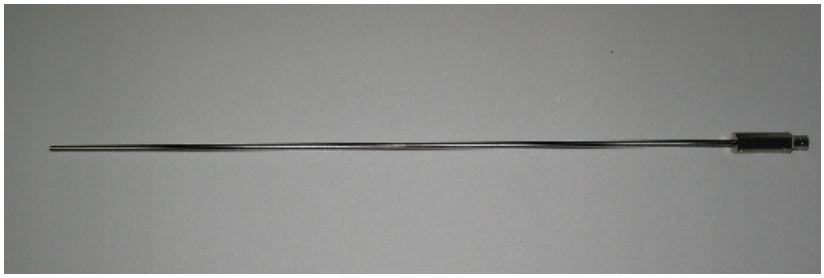

Figure 2.5: Hot-film Probe Support

The two-dimensional automatic traverse was controlled using LabVIEW and was capable of moving about 45 inches in the horizontal direction and about 49 inches in the vertical direction. The interrogation plane was 44 inches by 48 inches; starting 14 inches above the floor of the tunnel and 12 inches from the tunnel wall on the braces side of the landing gear as shown in Figure 2.6.

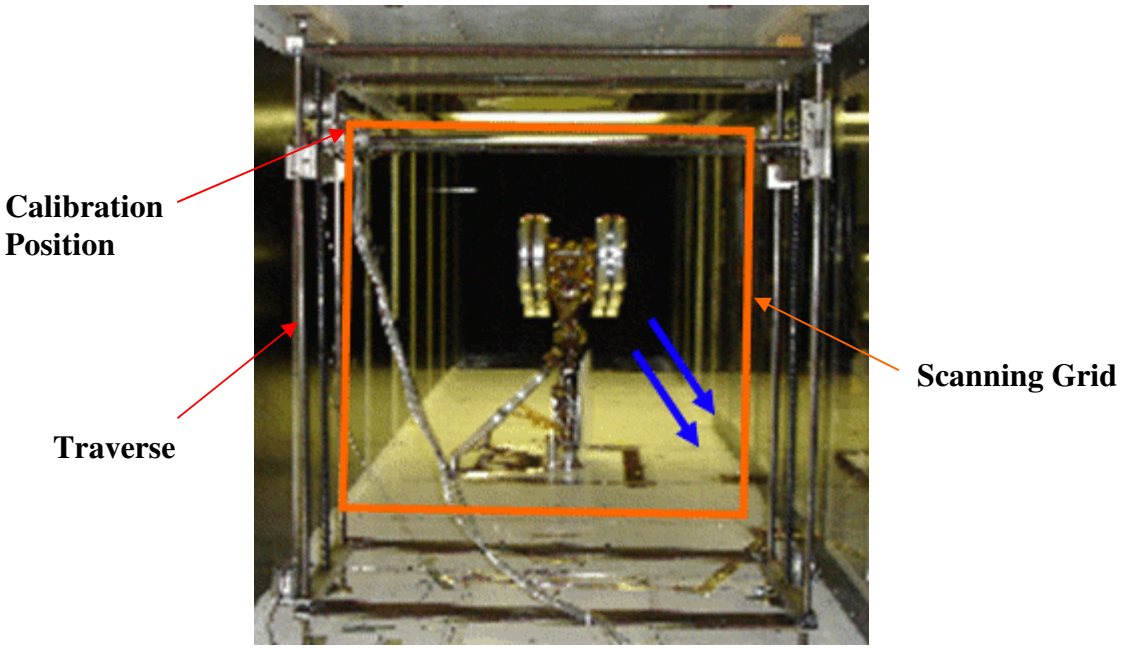

Figure 2.6: Traverse Installed in the VT-SWT.

2.3.2 Anemometer

The hot-film measurements were taken in the constant temperature anemometry mode (CTA) using a Dantec 55M01 CTA hot-wire anemometer shown in Figure 2.7. A 3 KHz square wave was used to tune the frequency response which was monitored using an oscilloscope and the over-heat ratio was 1.5. The hot-film sensor response was recorded after frequency tuning to calculate the cut-off frequency of the sensor. The frequency response of the sensor was found out to be about 30 KHz.

The probe was calibrated before and after each (Baseline and NCD) test condition. Thus, four different calibration data sets were obtained. During calibration, the tunnel was run at eight different speeds and the probe was placed in the free-stream away from the gear wake. Figure 2.6 shows the probe position for all the calibration runs.

Figure 2.7: Dantec 5501 CTA Hot-wire Anemometer

2.3.3 Data Acquisition System (High Frequency)

The output from the anemometer was fed to a signal conditioner which was connected to a four channel Nicolet BE-256 LE (shown in Figure 2.8) data acquisition system capable of recording data up to 1 MHz. A unit gain and an offset of 4 volts were used and the hot-film data was filtered using an anti-aliasing low pass filter set at 40 KHz. The data was sampled at 100 KHz using the Nicolet system which recorded 262144 samples per run. The data acquisition was triggered using a 2 volt DC input which was provided by the low frequency data acquisition system (explained in the next section). A computer connected to the data acquisition system was used to record the data in binary format which was then converted to ASCII format using TEAMCONV software provided by LDS Test and Measurement of Middleton, WI.

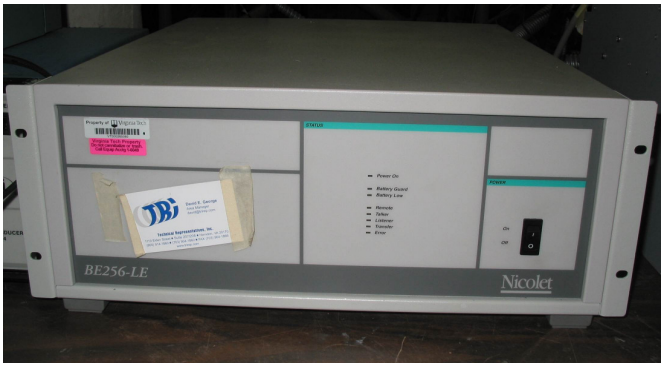

Figure 2.8: Nicolet BE 256-LE Data Acquisition System

2.4 Pitot-static Probe Measurements

Steady pressure measurements were made at the same time as the hot-film measurements at the same plane downstream of the landing gear. The same probe support mounting was used and the Pitot-static probe was placed one inch below the hot-film sensor.

2.4.1 Pitot-static Probe

The Pitot-static probe used in the experiment was manufactured by United Sensor Corporation of Amherst, NH. The PAE-12-M straight Pitot-static probe, shown in Figure 2.9 had an outside diameter (O.D.) of 1/4" and an internal diameter (I.D.) of 3/32" and was 12" long. The static pressure ports were 1" downstream from the measuring plane of the total pressure port. The Pitot probe was mounted one inch below the hot-film probe support on the same mounting in such a way that the measuring planes for the hot-film and the Pitot-static probes were at the same stream-wise location but one inch below the hot-film scanning plane.

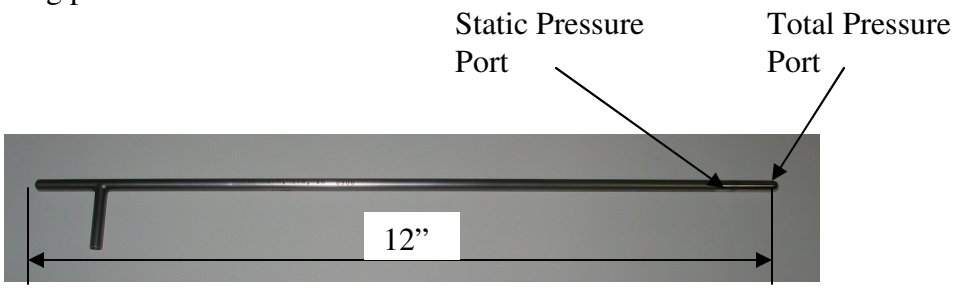

Figure 2.9: United Sensor Corporation PAE-12-M Pitot-static Probe

To measure the pressure upstream of the landing gear a Pitot-static probe already installed in the tunnel was used. The 0.5" O.D. probe measures the flow speed of the tunnel and was measuring total and static pressures at the entrance to the test section immediately after the contraction. The differential across the total and static ports of the tunnel Pitot probe was the dynamic pressure of the tunnel and was measured in inches of water.

The differential across the total pressure port and the static pressure ports of the Pitot-static probe in the wake was measured and was called as local (wake) dynamic pressure which can be converted into wake velocity. The differential between the total upstream pressure and the total pressure in the wake was called as the total pressure loss. Both the differential pressures were measured using two steady pressure transducers.

2.4.2 Pressure Transducer

Figure 2.10 shows two MKS Baratron Type 223B pressure transducers which were used to calculate wake total pressure loss and dynamic pressure in the wake of the landing gear. The bi-directional pressure transducers had a range of 0-100 mm of Hg and an accuracy of 0.5% of the full scale reading and the measuring ports had an O.D. of 3/16". The transducers had the ability to measure the gage pressures by keeping one of the ports open to atmosphere or to measure the differential pressures across the transducer element. The transducer output varied between 0-1 VDC which was recorded in a computer via a low frequency data acquisition system.

Figure 2.10: MKS Baratron Type 223 Pressure Transducers and Display Box

The pressure transducers were calibrated using a dead weight tester. The dead weight tester was connected to the pressure or positive side of the transducer while the other end was kept open to the atmosphere. Both the transducers were calibrated at the same time by supplying them with the same line pressure from the dead weight tester. The pressure was raised to 3 PSI (full scale) in steps of 0.5 PSI and then decreased in steps of 0.5 PSI

to check for hysteresis. The same steps were repeated when the line pressure was supplied to the ambient (negative) side of the transducers.

2.4.3 Data Acquisition System (Low frequency)

A 12-bit National instruments USB-6008 data acquisition card shown in Figure 2.11 was used to record data at low frequency. The multifunction data acquisition had eight analog inputs and two analog outputs and a maximum sampling frequency of 10000 Hz. The data acquisition system was controlled by a computer via National Instruments LabVIEW software. A Virtual Instrument (VI) was developed specifically to sample data at 10 Hz for 2 seconds from the 5 input channels and provide a 2 volt analog output. Out of the 5 input channels; channels 1 and 2 were dedicated to measure the local (wake) dynamic pressure and the total pressure loss behind the landing gear; channel 3 measured the low frequency hot-film anemometer output; and channel 4 and 5 were used to record the operating tunnel (flow) temperature and ambient pressure (measured by tunnel manometer) acquisition system, analog output channel 1 was used to provide a constant 2 volt output for 1 second. The VI was written such that every time data was taken, a 2 volt output was supplied which triggered the high frequency data acquisition (Nicolet) system.

Figure 2.11: National Instruments USB-6008 Data Acquisition System

For every grid point, the low speed data acquisition system recorded total wake pressure loss, wake dynamic pressure, tunnel operating temperature, anemometer output and

ambient pressure at 10 Hz for 2 seconds. The 2 volt analog output triggered the high speed data acquisition system which recorded the anemometer output at 100 KHz for 2.5 seconds.

Thus for every test configuration, a grid of 45"x 48" gave a total of 1104 grid points. The data files were arranged in folders representing (grid) columns and files representing (grid) rows. This led to a total of 23 folders each containing 48 files.

2.5 Tuft Flow Visualization

Flow visualization using tufts was performed over the 26% landing gear at Mach 0.17. Flow visualization was performed on both configurations (Baseline and NCD) and tuft was also used over the noise control devices to help understand the flow field.

Fluorescent green colored tufts were used along with hand-held UV light for better visualization. Aluminum tape was used to attach small pieces of tuft (about 2 to 3 inches) uniformly over the landing gear. The VT-SWT tunnel test section with Plexiglas windows (to provide for optical access) was illuminated using UV light and a hand-held Canon digital camcorder was used to take images. Figure 2.28 shows a picture of the raw video acquired during flow visualization using tuft over the braces region of the landing gear in 'Baseline' configuration and Figure 2.29 shows a picture of the braces region of the landing gear in the VT-SWT in 'NCD' configuration.

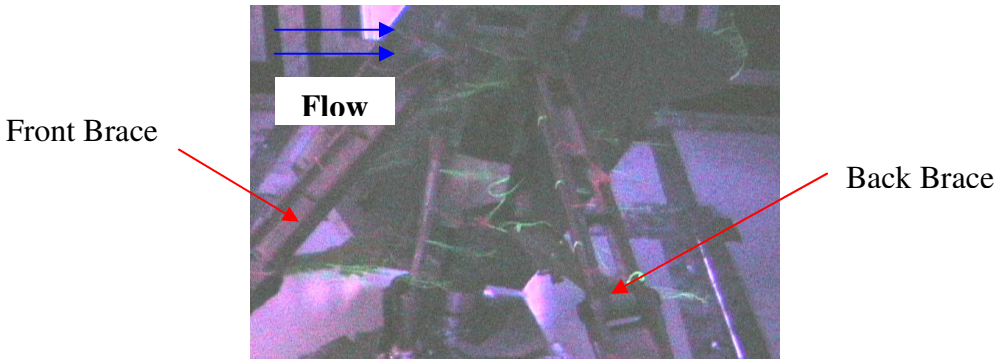

Figure 2.12: Flow Visualization over the Braces Region with Gear in 'Baseline' Configuration

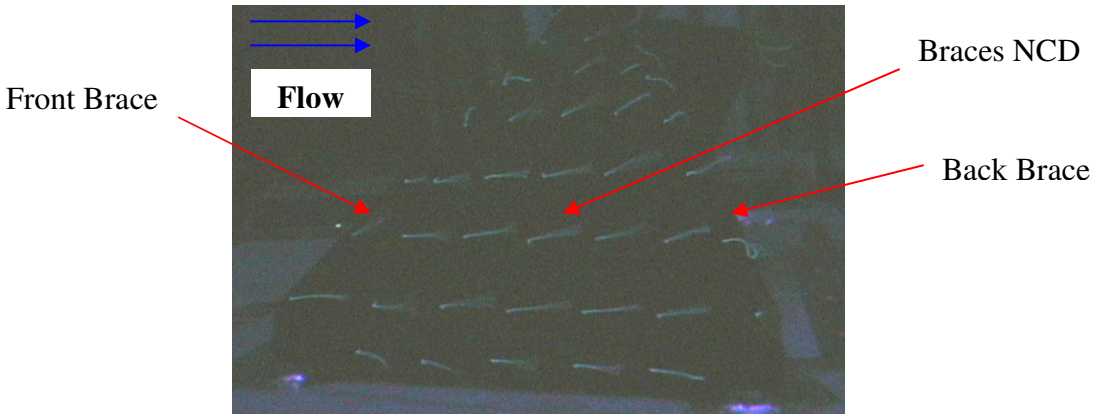

Figure 2.13: Flow Visualization over the Braces Region with Gear in 'NCD' Configuration

2.6 Particle Image Velocimetry

In 1970's Particle Image Velocimetry (PIV) was born out of Laser Speckle Velocimetry which was used in the field of solid mechanics, where scattered laser light was used to measure displacement of the surface of samples subjected to strain. In 1977, three different research groups, Barker and Fourney [13], Dudderar and Simpkins [14], and Grousson and Mallick [15], independently demonstrated the feasibility of applying the laser speckle phenomenon to fluid flow by measuring the parabolic profile in laminar tube flow. Rapid development continued in the 1980's and the field is now believed to be in its adult age where several systems are commercially available and flow measurements are accomplished on a variety of different test conditions.

PIV is based on the measurement of velocity of micron-sized tracer particles which are carried by the flow; the process is shown in Figure 2.14. An entire plane area is illuminated by a laser sheet and images of tracer particles (seeding) are captured by a high speed camera. These recordings either contain successive images of single tracers in time or successive frames of instantaneous images of the whole flow field. The displacement of the tracer particles is calculated by correlating the images and the time information is retrieved by calculating the time lag between the pair of images. Thus the actual measurement is performed in two steps: recording of images in the lab and

correlating or processing these images on a computer to determine flow velocities. A detailed understanding of the workings of PIV is not discussed in this report but can be found in Particle Image Velocimetry [16].

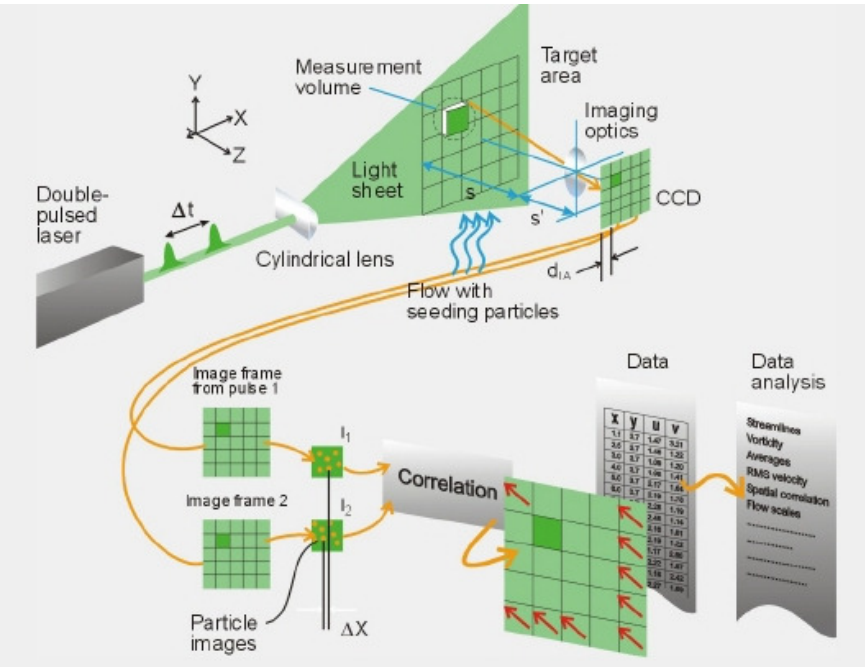

Figure 2.14: Measurement Principles of a PIV System (Dantec Dynamics)

Particle Image Velocimetry measurements were recorded by Dr. Jordi Estevadeordal of Innovative Scientific Solutions Inc. (ISSI) of Dayton, OH which specializes in optical diagnostic techniques for the aerospace industry. PIV measurements were taken at six different locations over the 13% landing gear without the door and a truck angle of zero degrees. A general experimental setup for the six planes is discussed briefly in this report.

Figure 2.15: New Wave Research Nd:YAG Laser

PIV measurements were taken in the Virginia Tech Stability Wind Tunnel (VT-SWT) which had the ability for optical access from three of the four tunnel walls (except the floor). Figure 2.15 shows the New Wave Research Nd:YAG laser with dual cavity which was placed in the control room. The power for the laser-sheet illumination was about 10-20 mJ/pulse. For the present experiments the magnification for the views were about 5 pixels/mm for the large views and about 25 pixels/mm for the closer views. A set of mirrors, lenses and prisms were used to orient and focus the laser sheet at the requisite locations. Optical deviations produced by the Plexiglass wall had no effect since magnifications were measured with the views from the behind the glass. The resulting laser sheet was about one millimeter thick and exposed the seed particles within a two-dimensional slice of the flow field. An ES1.0 Kodak CCD camera was placed outside the tunnel and connected to a computer to capture digital images. A 60-mm and 105-mm Nikon lenses set at an F stop of 5.6 were used. The camera would record black and white images with 8 bit pixel depth and a resolution of 1008 x 1012 pixels at a frequency of 15 Hz. A dry particle air seeder was fabricated here at Virginia Tech and was used during the investigation. Aluminum dioxide was used as the seed (0.3 microns in diameter) and bottled air was used to pressurize the seeder up to a maximum of 120 PSI. After one run (acquiring 300 pairs of images) the seeder had to be cleaned and refilled for subsequent use. The seeder was placed underneath the floor of the tunnel and seeding was done via a perforated half inch stainless tube shown in Figure 2.16. The tube was placed about 20" upstream of the landing gear so that the seed was diffused in the flow at the required

locations and the wake shed from the seeder rod was not influencing the flow field at the measurement planes. Swagelok fittings were used to firmly secure the seeder rod to the tunnel floor during operation.

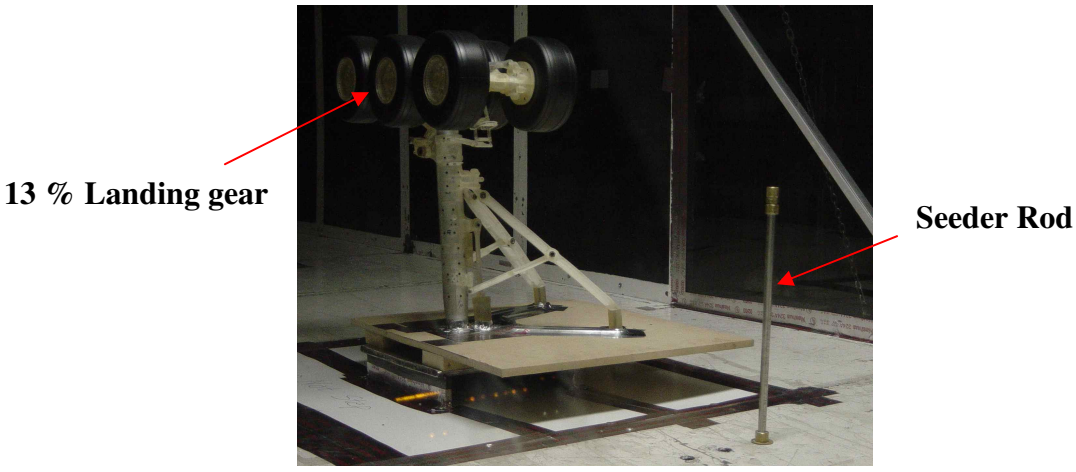

Figure 2.16: Seeder Rod in the VT-SWT with 13% Gear

For every run, 300 pairs of images were recorded and correlated to give the velocity field. Table 2.1 lists the different investigation planes and their corresponding run numbers.

Table 2.1 Six Measurement Planes and their Corresponding Run Numbers

View Number	View Name	Run Numbers
1	Large View between Braces	A – H
2	Vertical Plane Close View behind Front Brace	14 – 16
3	Vertical Plane Wheels View	17 – 21
4	Back Wheel View Vertical Plane	23 – 24
5	Inclined Plane 13 deg Front	25 - 27
6	View From Top	36 - 41

2.6.1 Plane 1: Large View between Braces

Figure 2.17 shows the experimental setup for 'Large View between Braces'. The 8- by 8-inch vertical square plane investigates flow between the two braces. The plane was

illuminated by shining the laser from the top of the tunnel and the camera was placed on the braces side (outside the tunnel).

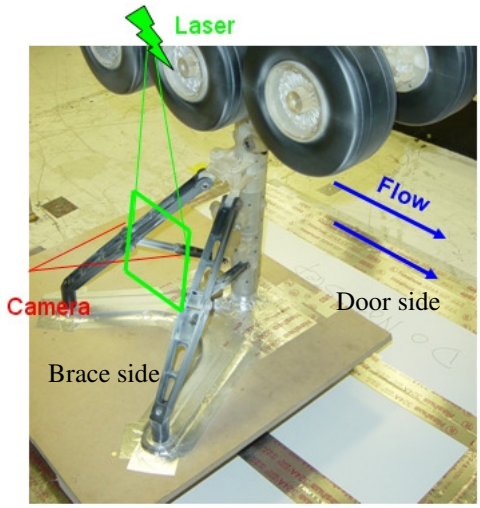

Figure 2.17: Experimental Setup for 'Large View between Braces'

Figure 2.18 shows a pair of superimposed images recorded by the CCD camera which are correlated to obtain instantaneous vectors. Upon careful observation, the front and the back brace can be seen on the right and left side of the image. Aluminum dioxide powder used as seeding is clearly visible in the laser sheet.

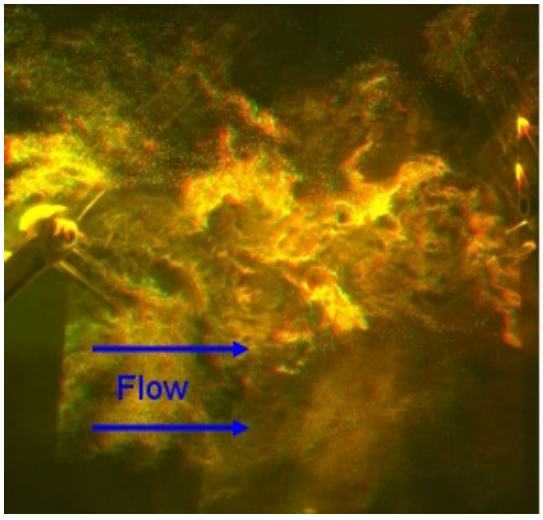

Figure 2.18: Superimposed Pair of Recorded Images for 'Large View between Braces'

2.6.2 Plane 2: Vertical Plane Close View behind Front Brace

Figure 2.19 shows the experimental setup for 'Vertical Plane Close View behind Front Brace' which was behind the front brace. The 2- by 2-inch vertical plane parallel to the flow investigates the flow behind the front brace. The laser sheet was introduced from the top of the tunnel and the camera was placed at the same location (outside the tunnel on the braces side) as for the previous view.

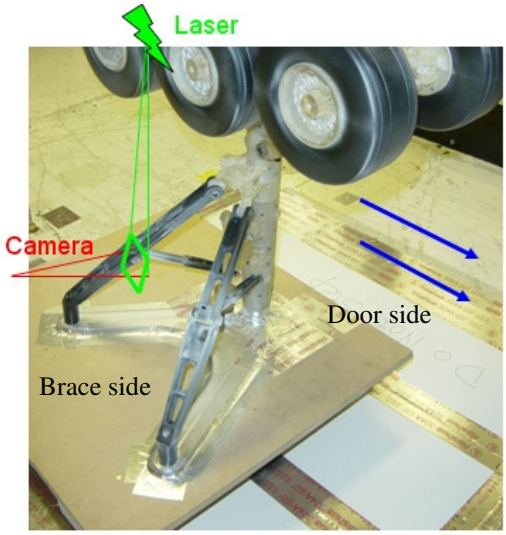

Figure 2.19: Experimental Setup for 'Vertical Plane Close View behind Front Brace'

Figure 2.20 shows the pair of superimposed image recorded by the CCD camera. The front brace connection with the lock link is clearly visible.

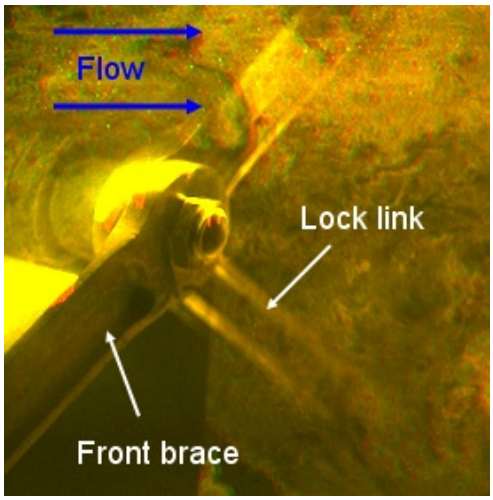

Figure 2.20: Pair of Superimposed Images for 'Vertical Plane Close View behind Front Brace'

2.6.3 Plane 3: Vertical Plane Wheels View

Figure 2.21 shows the experimental setup for the 'Vertical Plane Wheels View' in which the 3.5- by 3.5-inch plane is illuminated by directing the laser from the top and the camera is placed outside the tunnel on the braces side. The laser sheet was focused on the center of the wheel span, between the first and the second wheel and was parallel to the flow.

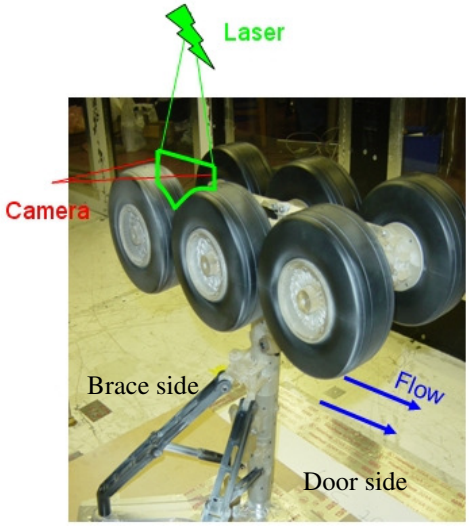

Figure 2.21: Setup for 'Vertical Plane Wheels View'

Figure 2.22 shows the 3.5- by 3.5-inch, 1000- by 1000-pixels image captured by the CCD camera and used for correlations to obtain flow information. The flow is from left to right and Aluminum dioxide seeding is visible between the first and the second wheels.

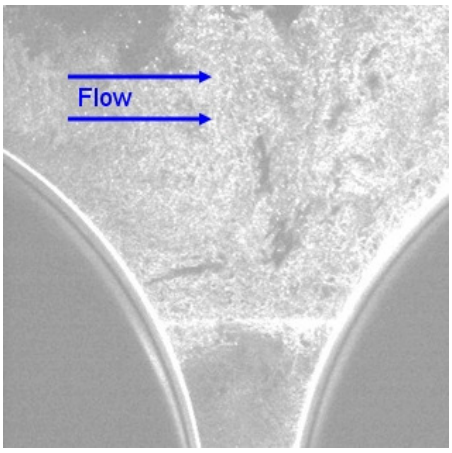

Figure 2.22: Image Captured by CCD camera for 'Vertical Plane Close View'

2.6.4 Plane 4: Back Wheel View Vertical Plane

Figure 2.23 shows the experimental set-up for 'Back Wheel View Vertical Plane'. The investigated plane (3.5- by 3.5-inch) was illuminated from the top of the tunnel and the CCD camera was focused from outside the tunnel on the braces side. The laser plane sheet was incident at the back end of the right back wheel, on the center of the wheel span and was parallel to the flow.

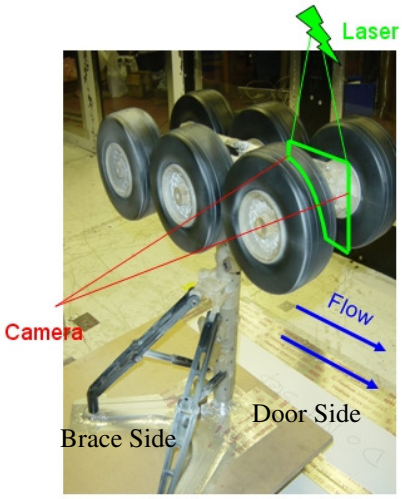

Figure 2.23: Setup for 'Back Wheel View Vertical Plane'

Figure 2.24 shows a grayscale 3.5- by 3.5-inch picture acquired by the CCD camera and recorded by the computer. The flow is from left to right and Aluminum dioxide seeding can be clearly noticed in the plane illuminated by the laser sheet.

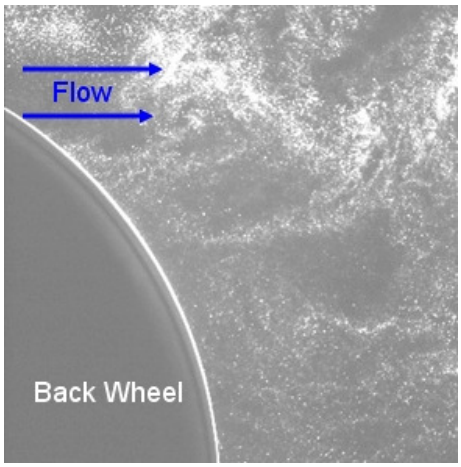

Figure 2.24: Image captured for 'Back Wheel View Vertical Plane'

2.6.5 Plane 5: Inclined View 13 Degrees Front

Figures 2.25 and 2.26 show the experimental set-up for 'Inclined Plane 13 Degrees Front'. For this plane, the laser sheet was introduced from the top of the tunnel at an angle of 13 degrees from the vertical. The CCD camera acquired 3.5- by 3.5-inch images and was placed outside the tunnel on the braces side.

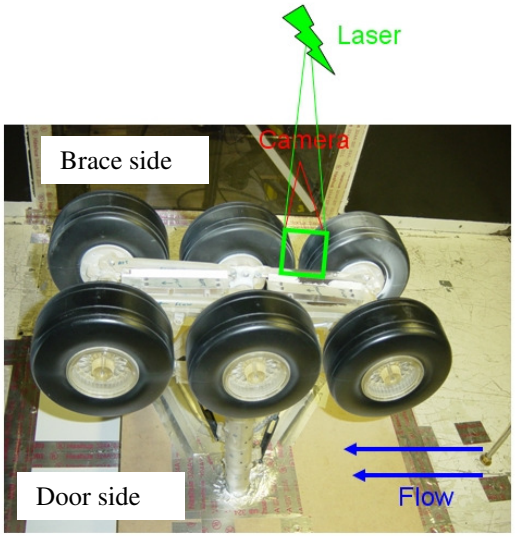

Figure 2.25: Experimental Setup for 'Inclined Plane 13 Degrees Front' (Top View)

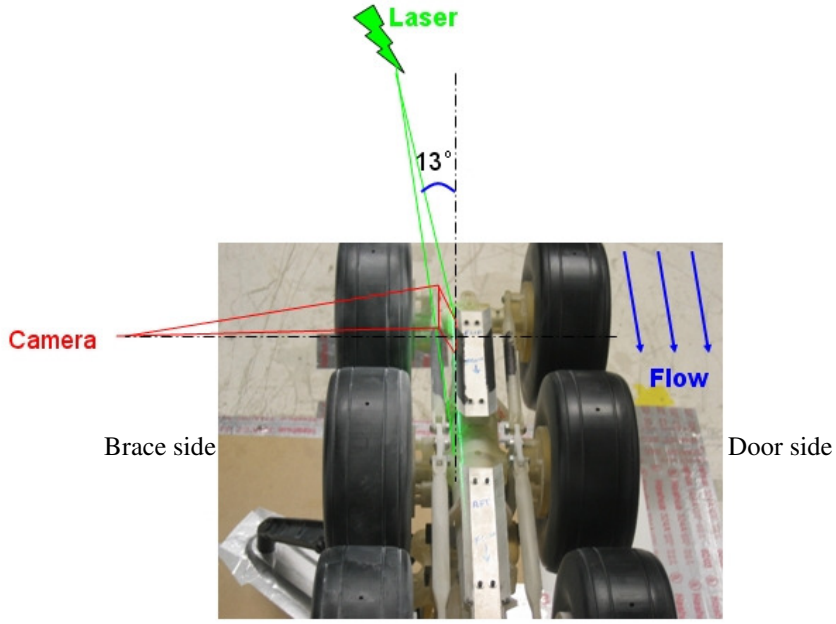

Figure 2.26: Experimental Setup for 'Inclined Plane 13 Degrees Front' (Back View)

Figure 2.27 shows the 3.5- by 3.5-inch image captured by the CCD camera. Part of the truck on the bottom, small part of the right front wheel on the bottom right corner and a very small part of the right middle wheel of the bottom left corner are clearly visible in the image.

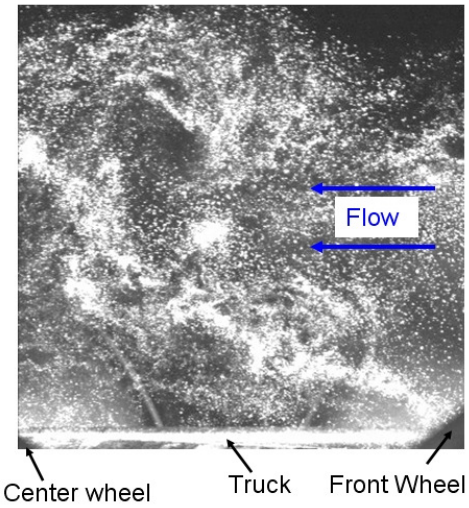

Figure 2.27: Image Captured for 'Inclined Plane 13 Degrees Front'

2.6.6 Plane 6: View from Top – Horizontal Plane

The experimental set-up for 'View from Top – Horizontal Plane' (shown in Figure 2.28) involved placing the CCD camera on the Plexiglas roof of the tunnel and the laser optics were placed inside the tunnel about 60 inches upstream of the landing gear. The optical mirrors and prism were secured strongly to the floor of the tunnel with the help of mounting plates.

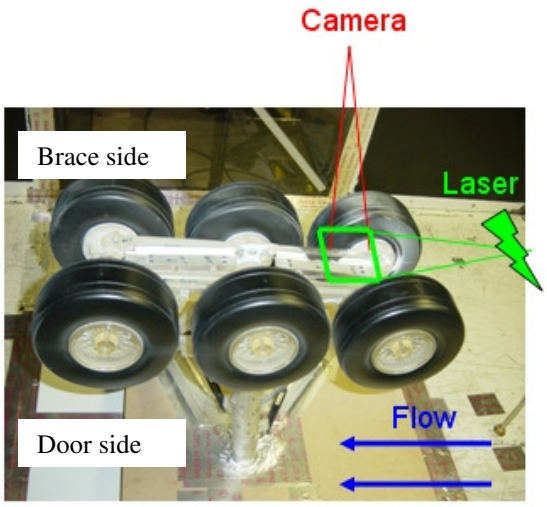

Figure 2.28: Experimental Setup for 'View from Top – Horizontal Plane'

Figure 2.29 shows the 3.5- by 3.5-inch image captured by the CCD camera. The image shows the left and right front wheels and Aluminum dioxide seeding illuminated by the laser sheet is clearly visible.

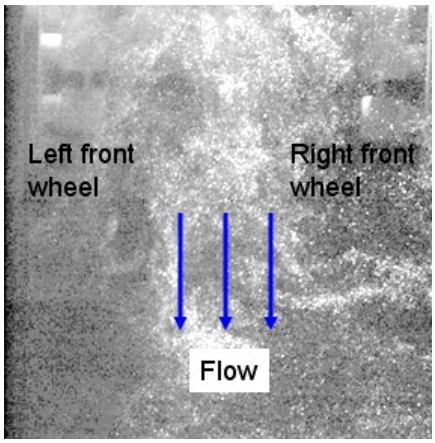

Figure 2.29: Image Captured by CCD Camera for 'View from Top – Horizontal Plane'

Chapter 3
Data Reduction

Aerodynamic measurements which included hot-wire anemometry, Pitot-static pressure, Particle Image Velocimetry and flow visualization using tufts were conducted as a part of an aeroacoustic investigation at the Virginia Tech Stability Wind Tunnel (VT-SWT). This chapter describes the data reduction techniques for aerodynamic measurements. A novel technique to process hot-film measurements as acoustic Microphone Phased Array (MPA) measurements (developed at Virginia Tech as a part of this investigation) is also presented in this chapter.

3.1 Hot-film Measurements

Hot-wire measurements were taken at a plane 64" downstream of the main strut in the wake of the landing gear. The dimensions of the scanning grid were 45" x 47" and the grid resolution was 2" x 1". Two configurations of the gear were tested namely; Baseline and Noise Control Devices (NCD). Both the configurations employed a fully dressed isolated 26% high fidelity landing gear at a truck angle of 13 degrees.

A MATLAB code was written to process the data. The voltage recorded by the data acquisition system was converted into actual anemometer output (E_W) by using the equation:

$$E_W(m) = 1/G * E_G(m) + E_{off}$$

Where, E_G was the recorded voltage, G was the gain and E_{off} was the offset used during data acquisition. An offset of 4 volts and a unit gain were used during data acquisition.

3.1.1 Temperature effects

Tunnel (flow) temperature was also measured while data was recorded and it was noticed that the tunnel temperature varied from a minimum of 8 degrees Celsius during survey of baseline configuration to a maximum of 15 degrees Celsius during NCD configuration. For the sake of ease of comparison the hot-film data was referenced to a common temperature (10 degrees Celsius). Bearman [18] uses the relationship between the ambient (flow) temperature and the wire temperature to convert anemometer output into voltage at a referenced temperature at constant velocity. The relationship is given by;

$$E_w (T_w - T_{a,r})^{1/2} = E_{w,r} (T_w - T_a)^{1/2}$$

Where, E_w is the anemometer output voltage,

T_w is the operating wire resistance,

$T_{a,r}$ is the referenced flow temperature,

T_a is the recorded flow temperature and

$E_{w,r}$ is the referenced output voltage.

For each configuration run, temperature was recorded for every column traversed and the anemometer output voltage was converted to voltage at the referenced temperature.

3.1.2 Calibration

Calibration of the hot-film probes was done before and after every configuration run. Thus, four sets of calibration were performed on the same sensor (which was held in the free-stream, shown in Figure 2.6), during which the tunnel speeds were also recorded. The referenced anemometer output voltage for all the calibration runs agreed with each other at similar free-stream velocities. Figure 3.1 shows the 4^{th} order curve fit which was used to convert referenced output voltage into velocity for both configurations. Thus, the voltage recorded by the A/D converter was converted into velocity referenced at 10 degrees Celsius.

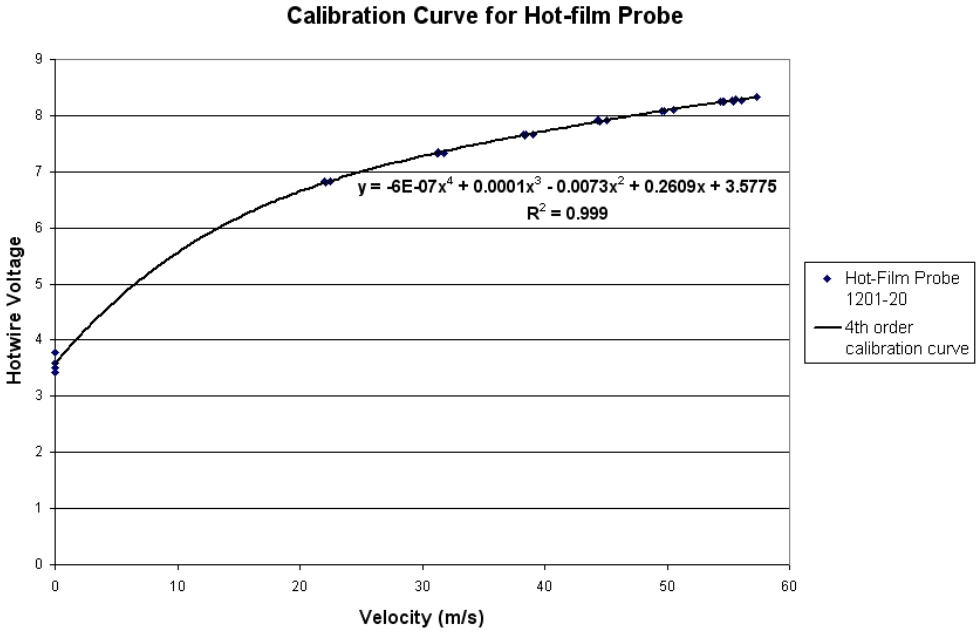

Figure 3.1: 4th Order Calibration Curve for Hot-film Probe

3.1.3 Time Domain Analysis

Time domain analysis involving calculation of the mean velocity, the root mean square of the velocity and the turbulence intensity were carried out using the hot-film data.

The total velocity, *X(t),* obtained after applying the calibration can be expressed as a sum of the fluctuating component (unsteady velocity), *x'(t)*, and a steady component also called as the mean velocity $\overline{X}$.

$$X(t) = \overline{X} + x(t)$$

The mean value $\overline{X}$ is simply the average of all the values of an infinitely long time history record and is given by:

$$\overline{X} = \lim_{T \to \infty} \frac{1}{T} \int_0^T X(t)dt$$

It was not possible to acquire data for an infinitely long period of time and the velocity infinite time history, *X(t)*, is replaced by a corresponding digital sample record, *X(n)*. The

total sample time, T, and the number of samples, N, are related to the sampling rate, SR, by:

$$N = SR * T$$

And the time interval between samples, Δt, is given by

$$\Delta t = \frac{1}{SR} = \frac{T}{N}$$

Thus the mean value (velocity) for a sample of finite length was expressed as:

$$\overline{X} = \frac{1}{N} \sum_{n=1}^{N} X(n)$$

The root mean square velocity for a sample of finite length was calculated as:

$$X_{RMS} = \sqrt{\frac{(X(t) - \overline{X})^2}{N}}$$

The turbulence intensity was calculated by dividing the root mean square velocity by the mean free-stream velocity:

$$Tu = \frac{X_{RMS}}{\overline{X}_{\infty}}$$

The above calculations were done for each grid point and a value of mean velocity and turbulence intensity was obtained. Contour plots of the same were made for both the configurations.

3.1.4 Frequency Domain Analysis

One of the goals of this investigation was to compare acoustic Microphone Phased-Array (MPA) results to hot-film measurements. The MPA results were obtained by Ravetta (2005) using a beamforming algorithm which was processed in the frequency domain using $1/12^{th}$ octave bands. Similar steps (frequency domain analysis and $1/12^{th}$ octave bands) were followed for the reduction of the hot-film data.

3.1.5 1/12th Octave Bands

The 1/12th octave frequency bands can be obtained by first finding the center (f_c), upper (f_u) and lower (f_l) frequencies as:

$$f_{c,n} = 2^{n/12}$$

$$f_{l,n} = \frac{f_{c,n}}{2^{1/24}}$$

$$f_{u,n} = f_{c,n} * 2^{1/24}$$

Where n corresponds to the band number (BN). Appendix C lists the band number, the center, upper and lower frequencies for 1/12th octave bands used during processing of MPA data and hot-film data.

3.1.6 Velocity Spectra

The unsteady component of velocity in time domain, $x'(t)$, was converted to velocity in frequency domain by using the Fast Fourier Transform (FFT) algorithm. This was accomplished by breaking the velocity time series into 16 equal parts, performing FFT on each individual part and then averaging the results. The velocity spectrum can be calculated by taking the product of the velocity in frequency domain, $x'(f)$, with its conjugate, $x'(f)^*$.

$$Spectra = x'(f) \cdot x'(f)^*$$

Velocity spectra for each grid point were obtained and a sample collected in the wake is shown in Figure 3.2.

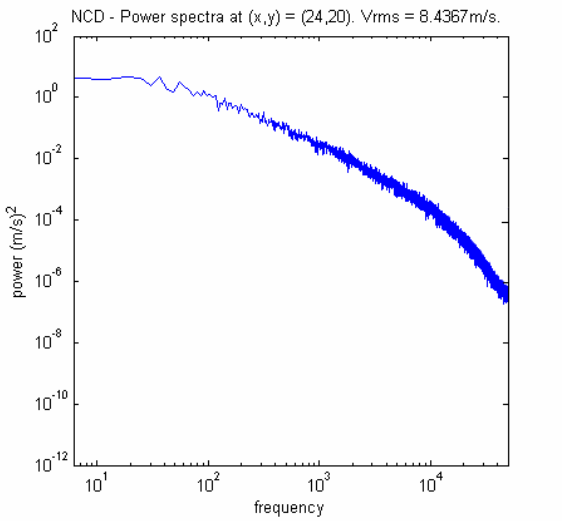

Figure 3.2: Sample Velocity Spectrum in the Wake of the Landing Gear

The spectra results (sample shown in Figure 3.4) were then broken into 1/12th octave band by adding the spectra value at every incremental frequency over the bandwidth. The frequency resolution was 6 Hz whereas the bandwidth for the first 80 1/12th octave bands was less than 6 Hz which led to zero spectra values for bands with center frequency (f_c) less than 104 Hz (the first 80 bands). Since MPA results were obtained for frequencies higher than 2000 Hz, the loss of 1/12th octave spectra results at lower frequencies was not of significance. Thus, the velocity spectra (sample shown in Figure 3.4) were broken into 1/12th octave bands to give a unique spectra value for every bandwidth at each grid point.

Spectra contour plots of each 1/12th octave bands were then plotted and one such example for f_c of 4.6 KHz corresponding to a Band Number (BN) equal to 146 is shown in Figure 3.3. By summing all of the 176 1/12th octave spectra contour plots (in frequency domain), the turbulence contour plots in time domain can be reconstructed (Figure 3.4). By applying the frequency domain decomposition to the hot-film data, turbulence was broken into 1/12th octave bands and can be compared to acoustic data.

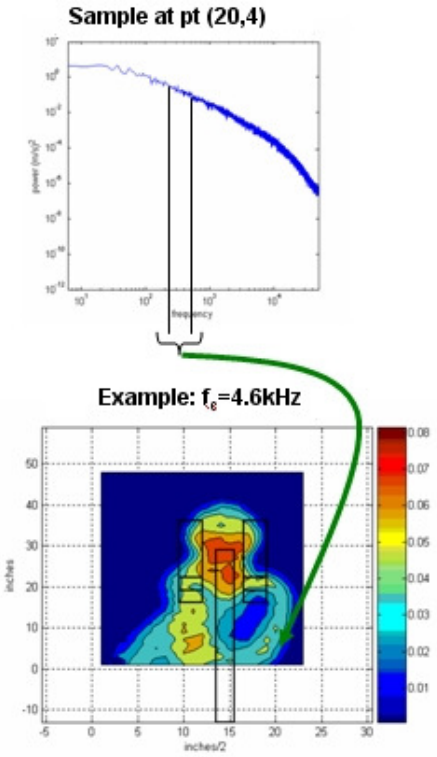

Figure 3.3: Sample Velocity Spectra Contour Plot for f_c=4.6 kHz (1/12th Octave Bands, BN =146)

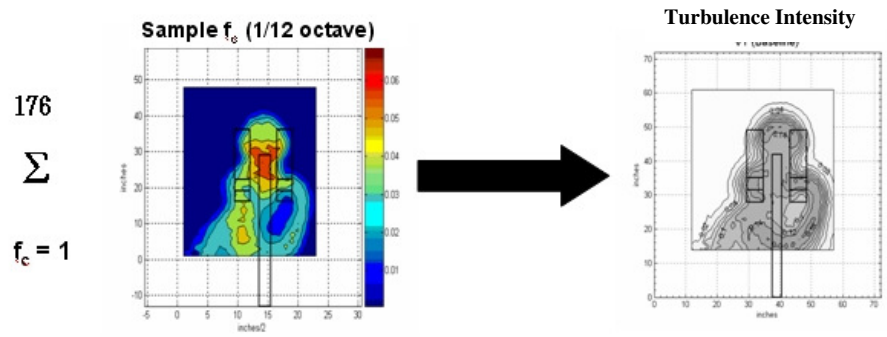

Figure 3.4: Sum of the 176 Spectra Contour Plots (Frequency Domain) is Proportional to the Turbulence Intensity (Time Domain)

To compare changes in the flow and the acoustics between the different configurations (Baseline and NCD) the projection of the beamforming grid (from Microphone Phased Array processing) on the hot-film survey plane was used (see Figure 3.5). For example, to quantify the effect of noise control devices on the truck, the area behind the truck

region was selected (shown in red box in Figure 3.5) and the velocity spectra value in each 1/12th octave band was integrated for both configurations (shown in Figure 3.6).

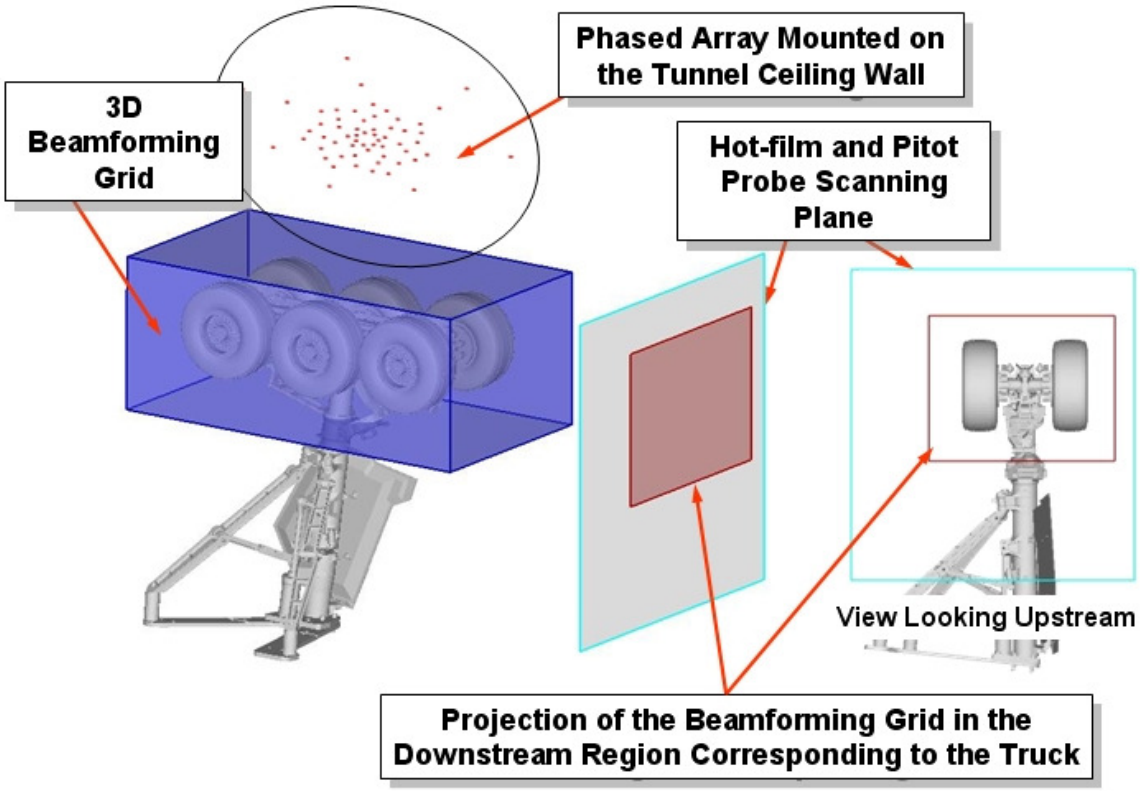

Figure 3.5: Projection of Beamforming Grid (Truck Region) on the Hot-film Scanning Grid

The area integrated spectra values for each band were converted into changes in decibels (dB) at every band by using:

$$\Delta dB_{BAND} = 10Log_{10}\left\{\sum_{Area}\frac{OctaveSpectra_{BASELINE}}{OctaveSpectra_{NCD}}\right\}$$

Figure 3.6 shows the comparison of spectra contour plots for f_c = 19.5 KHz. The velocity spectra values in the red box were used to calculate the reduction in decibels due to noise control devices by using the above formula.

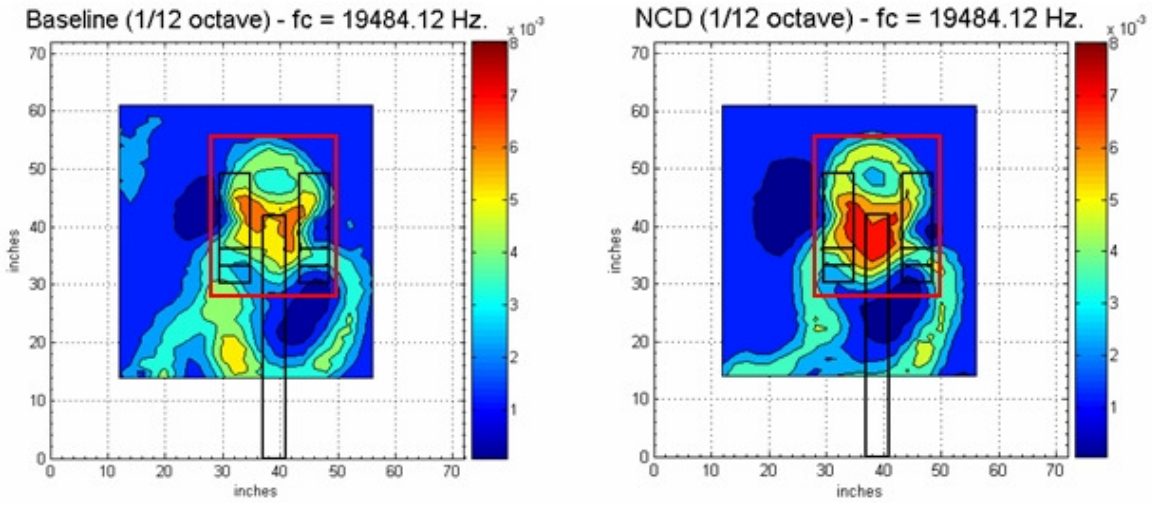

Figure 3.6: Contour Plots of Velocity Spectra Broken into 1/12th Octave Bands for 'Baseline' and 'NCD' Configurations. (Red box shows area behind the truck used to calculate reduction in noise)

3.2 Pitot-static Measurements

Low frequency pressure measurements (at 20 Hz) were taken in the wake of the landing gear using a Pitot-static probe at the same scanning plane as the hot-film probe. The two transducers recorded dynamic pressure and total pressure loss in the wake of the landing gear. The pressure transducers used to measure the pressures were calibrated using a dead weight tester. The calibration curves were linear and are shown in Figure 3.7.

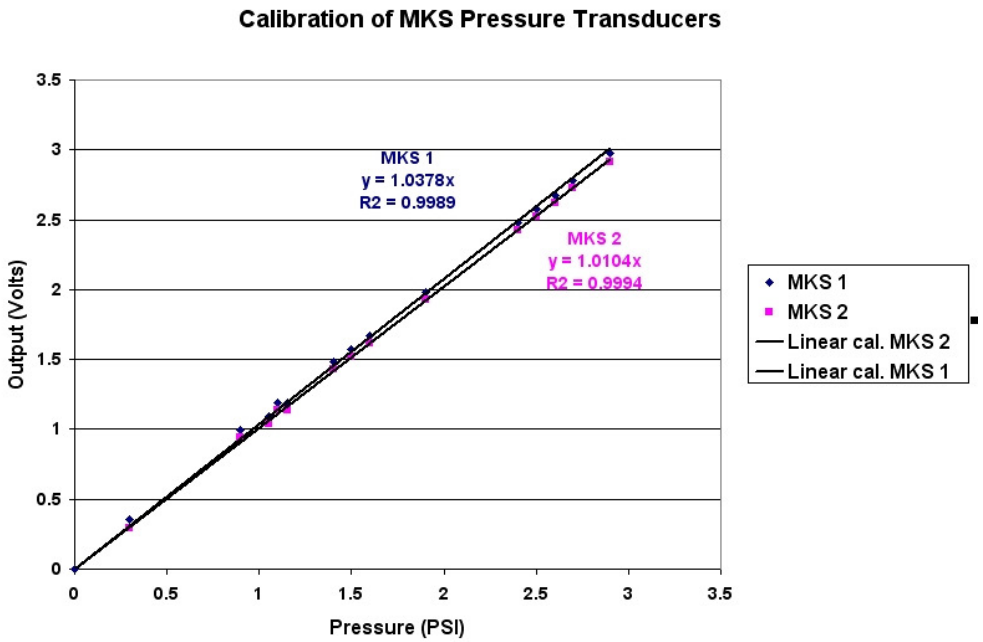

Figure 3.7: Linear Calibration Curve for MKS Transducers

The free-stream tunnel dynamic pressure from the tunnel Pitot-static probe was recorded and was used to normalize the wake velocity and the total pressure loss using the equations:

$$\text{Normalized Total Press. Loss} = \frac{\text{Survey Total Pressure} - \text{Free-stream Total Pressure}}{\text{Tunnel Free-stream Dynamic Pressure}}$$

$$\text{Normalized Wake Velocity} = \frac{\text{Wake Velocity}}{\text{Tunnel Free-stream Velocity}}$$

Contour plots of normalized wake velocity and normalized total pressure plots were made using the above formulae for both configurations.

3.3 Flow Visualization

Digital videos captured during flow visualization were studied carefully and tufts were drawn on a model landing gear using Tecplot software. The flow around the wheels,

truck, braces and lock link and gear door was analyzed and is discussed in the results section. Three different colors of tuft were used during analysis of flow. Blue tufts represent low or no turbulence, dark green tufts represent medium turbulence and red tufts represent high turbulence. The gear door is divided into zones representing different flow conditions. Dotted arrows are used around the model to portray the general flow direction.

The digital raw videos are saved and are available upon request. Flow visualization was performed on both ('Baseline' and 'NCD') configurations but results are only presented for 'Baseline' configuration. Most of the tuft results for 'NCD' configuration show smooth, steady, attached flow on the surface of the NCD as expected.

3.4 Particle Image Velocimetry

PIV measurements were taken at six different planes over the landing gear. The images acquired were correlated using double pass from the DPIV software provided by ISSI, Dayton, OH. Table 3.1 shows the calibration factors and the correlation factors used for converting pixel displacements per image pair into velocity for all the planes.

Table 3.1: Calibration Factors for PIV Data Reduction using DPIV software provided by ISSI

View Number	View Name	Pixels per mm	Dt (ms)
1	Large View Between Braces	4.91	35
2	Vertical Plane Close View	12.5	20
3	Vertical Plane Wheels View	11.6	20
4	Back Wheel View Vertical Plane	11.7	20
5	Inclined Plane 13 deg Front	11.2	20
6	View From Top	8.78	20

The pairs of 1000- by 1000-pixels images were correlated by double pass using the DPIV software. Each interrogation window measured 64- by 64-pixels with 75% overlap. A Gaussian fit was used to locate the correlation peaks within sub-pixel accuracy. Three

hundred pairs of images were averaged to calculate mean velocity for each image. The root mean square velocities were calculated using the same method explained in Section 3.1.3 in which hot-film data was analyzed in time domain. Vorticity can be physically interpreted as twice the angular velocity of the solid-body rotation and is given by;

$$\omega_i = \varepsilon_{ijk} \partial_j v_k$$

Where, w_i is the vorticity, ε_{ijk} is the alternating unit tensor, ∂_j is the differential with respect to the j co-ordinate and v_k is the velocity in the k direction.

Chapter 4
Experimental Results and Conclusions

This chapter presents the results and draws conclusions from aerodynamic measurements performed on a 777 main landing gear in the Virginia Tech Stability Wind Tunnel capable of reaching a maximum speed of Mach 0.16 with 6% blockage effects. Hot-film and Pitot-static pressure measurements and flow visualization using tuft were performed on an isolated 26% high fidelity model with a truck angle of 13 degrees. Particle Image Velocimetry (PIV) measurements were acquired over an isolated 13% high fidelity model with a truck angle of zero degrees and no gear door.

4.1 Results

Mean wake velocity and turbulence intensity were measured for both configurations (Baseline and NCD) using a hot-film probe, whereas total pressure loss was measured using a Pitot-static probe connected to a pressure transducer. Flow visualization using tufts was also performed for both configurations to look at the flow over the landing gear and the changes in the flow due to noise control devices. PIV measurements were taken at six different planes over the 13% landing gear for the 'Baseline' configuration.

4.1.1 Hot-film and Pitot-static Pressure Measurements

Hot-film anemometry and Pitot-static pressure measurements were taken in the wake of the landing gear at a plane 64" downstream of the main strut. The data was reduced and contours of normalized wake velocity, turbulence intensity and normalized total pressure loss were made. The results are compared to aeroacoustic investigation done by Horne et al. [7] in which the 26% isolated high fidelity models was used in the NASA Ames 7- by 10- foot wind tunnel which was capable of reaching speeds of 0.22 Mach and 4% blockage effects.

4.1.1.1 Comparison with NASA Ames

Figure 4.1 shows contours of wake velocity normalized with the tunnel free-stream velocity behind the high fidelity 777 landing gear (projected). The NASA Ames results for the high fidelity gear are on the left where as the Virginia Tech (VT) results for the high fidelity gear in 'Baseline' configuration are plotted on the right. The contours agree with each other appreciably given the differences in the flow speeds, the blockage and the dimensions of the tunnel. The minimum velocity in both the cases was calculated to be around 0.36 times the tunnel free-stream velocity.

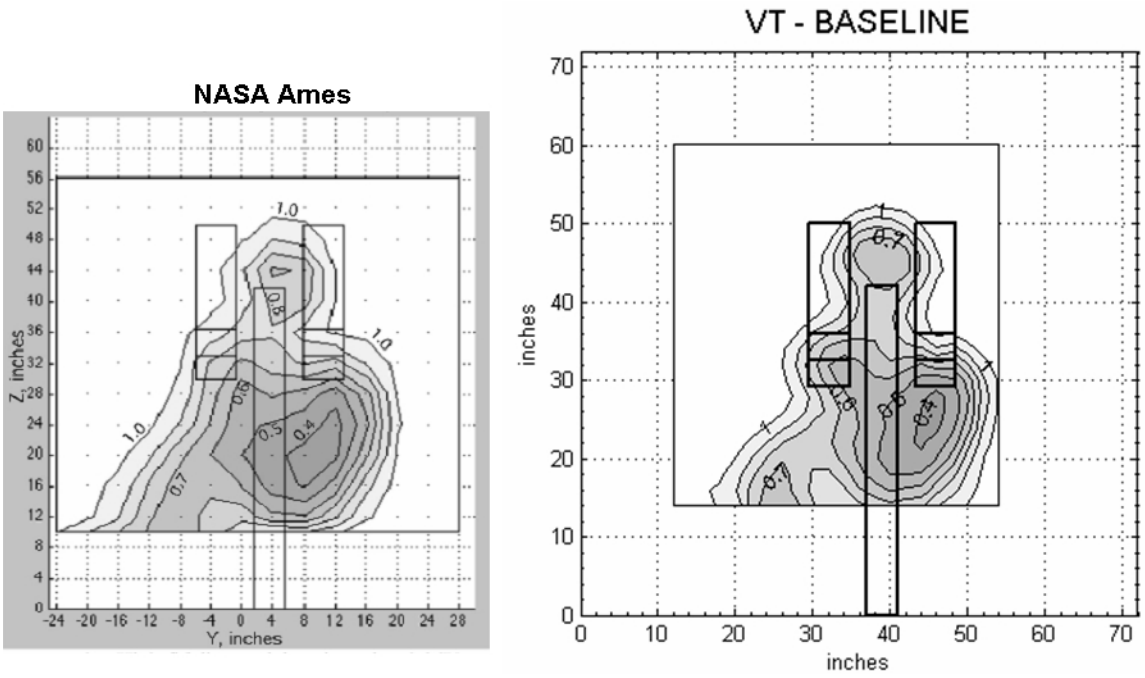

Figure 4.1: Contours of Normalized Wake Velocity; Comparison between NASA Ames [7] and VT-SWT

Figure 4.2 shows contour plots of normalized total pressure loss measured at the NASA Ames facility and the VT-SWT at a plane 64 inches downstream of the landing gear measured using a Pitot-static probe and normalized by the tunnel free-stream dynamic pressure. The VT-SWT results for the 'Baseline' 26% high fidelity gear compare well

with a similar model used during testing at NASA Ames. Both the measurements gave a similar peak loss value of 1.0 times the tunnel free-stream dynamic pressure given the difference in the test facilities.

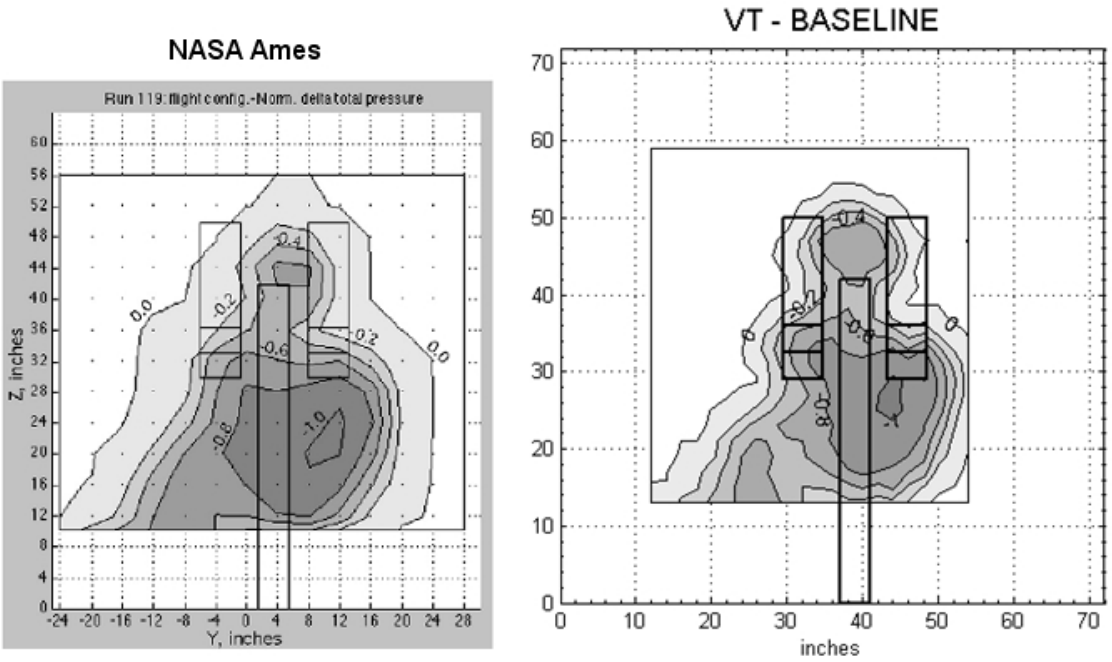

Figure 4.2: Contours of Total Normalized Pressure Loss; Comparison of NASA Ames [7] and VT-SWT

Figure 4.3 shows the contour plots for turbulence intensity which was calculated using hot-film measurements in the wake of the high fidelity 777 landing gear. The root mean square velocity was normalized by the tunnel free-stream velocity to give turbulence intensity contours on a percentage basis. The contour profiles are different but the maximum turbulence levels are comparable (12.7 % for NASA Ames to 16 % for VT-SWT). The differences in the contours can not be currently explained, but the turbulence contour is similar to the wake velocity contour from both the VT and NASA Ames results.

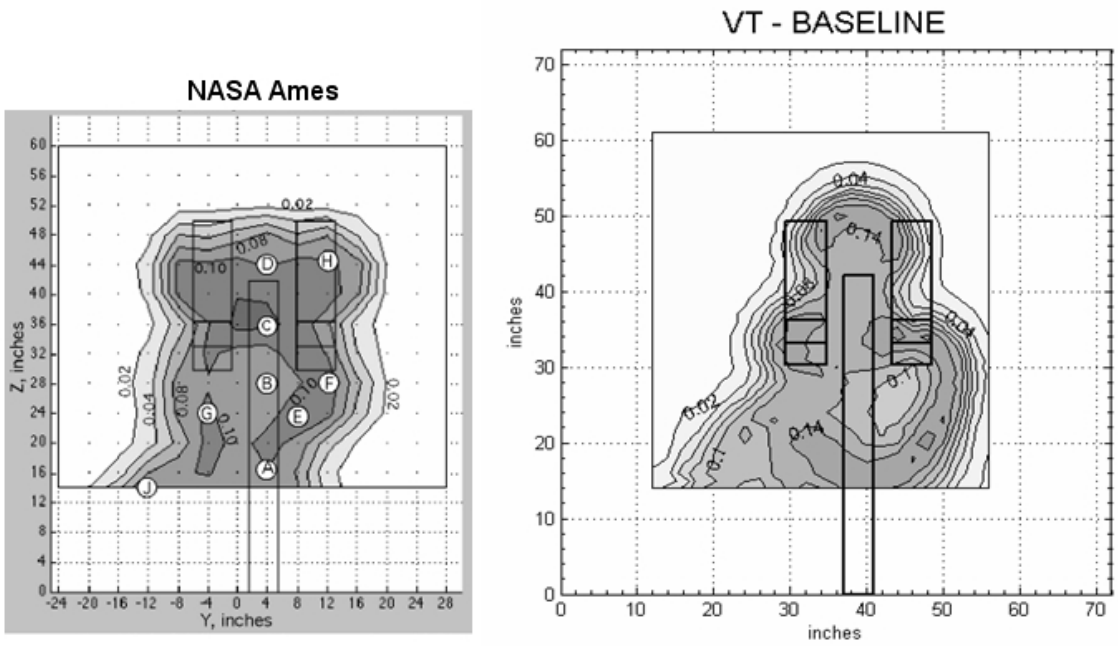

Figure 4.3: Contours of Turbulence Intensity (%); Comparison between NASA Ames [7] and VT-SWT

4.1.1.2 Comparison of Baseline and NCD Configurations

Hot-film and Pitot-static pressure measurements were taken for both 'Baseline' and 'NCD' configurations at the same location in the wake of the landing gear. Normalized wake velocity, normalized total pressure loss and turbulence intensity contours were used to compare the effects of noise control devices in terms of changes in gear wake. Cutouts of the landing gear for both configurations were projected over the contour plots to give a better understanding of the gear geometry and look at changes in flow behind the noise control devices.

Figure 4.4 shows contour plots of normalized wake velocity taken at a plane 64" downstream of the main strut in the wake of the landing gear. The isolated high fidelity 26% model of the landing gear shows some marked changes. The region behind the gear door (on the right side of the gear) shows regions of lower wake velocity whereas the region behind the braces noise control devices shows a change in the shape of the wake

velocity profile and hence a region of higher velocity. The truck noise control devices seem to have little or no effect on the normalized wake velocity of the gear.

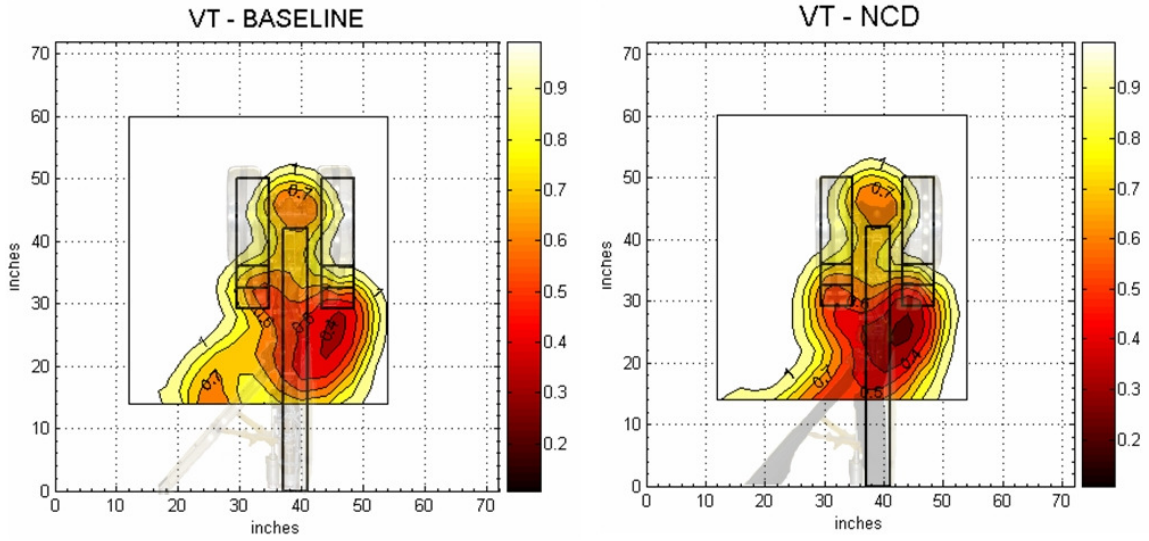

Figure 4.4: Contours of Normalized Wake Velocity; Comparison between VT-Baseline and VT-NCD

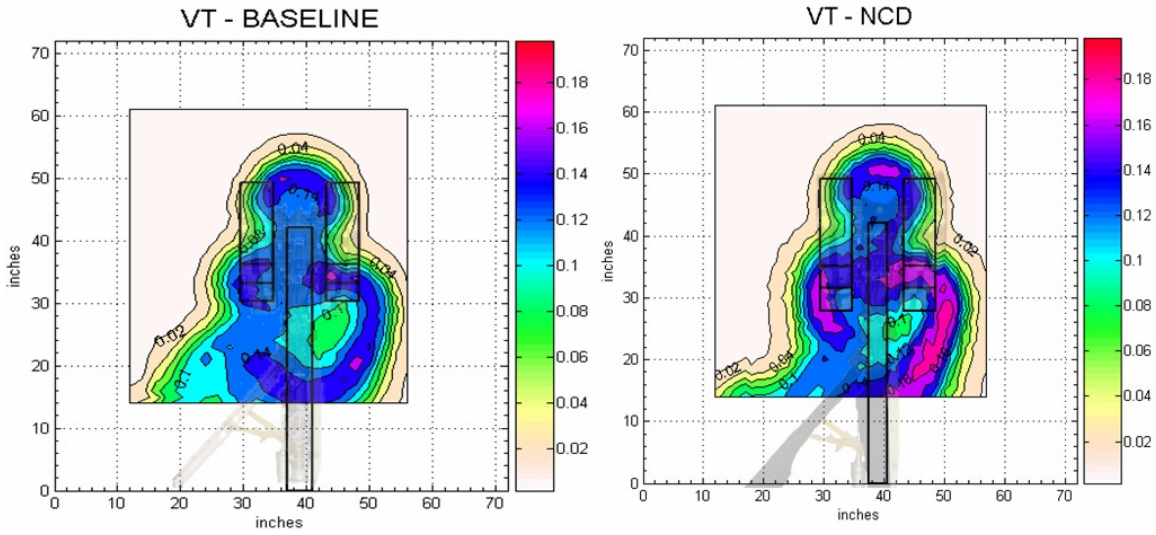

Figure 4.5: Contours of Turbulence Intensity (%); Comparison between VT-Baseline and VT-NCD

Figure 4.5 compares contours of turbulence intensity between 'Baseline' and 'NCD' configurations and shows areas of higher turbulence in the gear door region. Behind the braces region, the shape of the turbulence profile has changed and shows lower overall turbulence intensity due to streamlining of flow. There is a small increase in the

turbulence intensity behind the truck region which is within the uncertainty in measurement and hence considered insignificant.

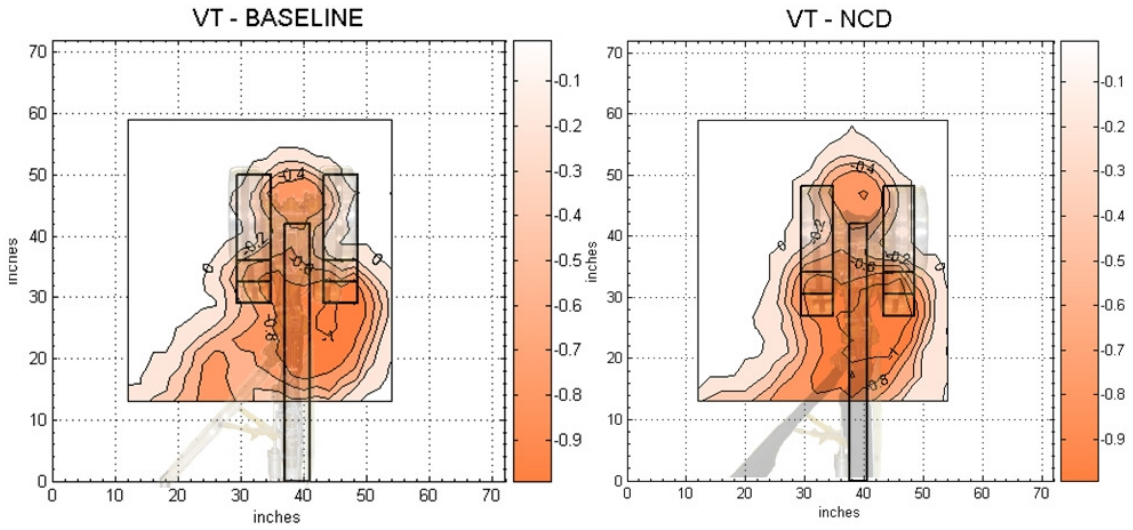

Figure 4.6: Contours of Normalized Total Pressure Loss; Comparison of VT – Baseline and VT-NCD

Figure 4.6 shows contours of normalized total pressure loss for both the configurations in the wake of the isolated 26% high fidelity landing gear. Normalized total pressure loss was calculated by subtracting the upstream (tunnel) total pressure from the local total pressure and normalized by the free-stream total pressure. Behind the gear door, areas of higher pressure loss are noticed whereas areas of lower pressure loss are noticed behind the braces noise control devices in the 'NCD' configuration as compared to the 'Baseline' configuration. There is no significant difference in pressure loss behind the truck region. After integrating the pressure loss contours, there was an increase in drag of 8 % for the 'NCD' configuration as compared to the 'Baseline' configuration.

4.1.1.3 Spectra in the Wake of the Gear

Velocity spectra were calculated for every grid point measurement taken with the hot-film probe. The turbulence in the wake of the gear can be broken into frequency domain and can be seen in terms of energy. Figure 4.7 shows contour plot of turbulence intensity in the wake of the landing gear in 'Baseline' configuration. The contour map is broken into five zones (shown in Figure 4.7), in which the grid points have similar spectra

characteristics. The sample spectra for each zone are plotted in Figures 4.8 to 4.12. Figure 4.8 shows the spectra in the free-stream which can also be interpreted as the noise floor of the tunnel at 55m/s.

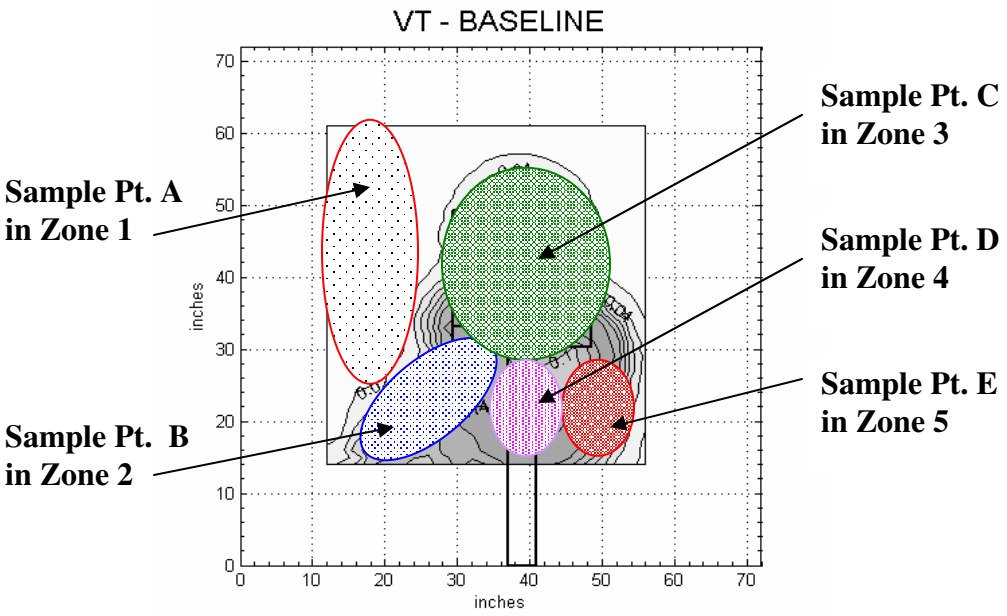

Figure 4.7: Turbulence Intensity Contours for VT-Baseline Showing Different Spectra Zones

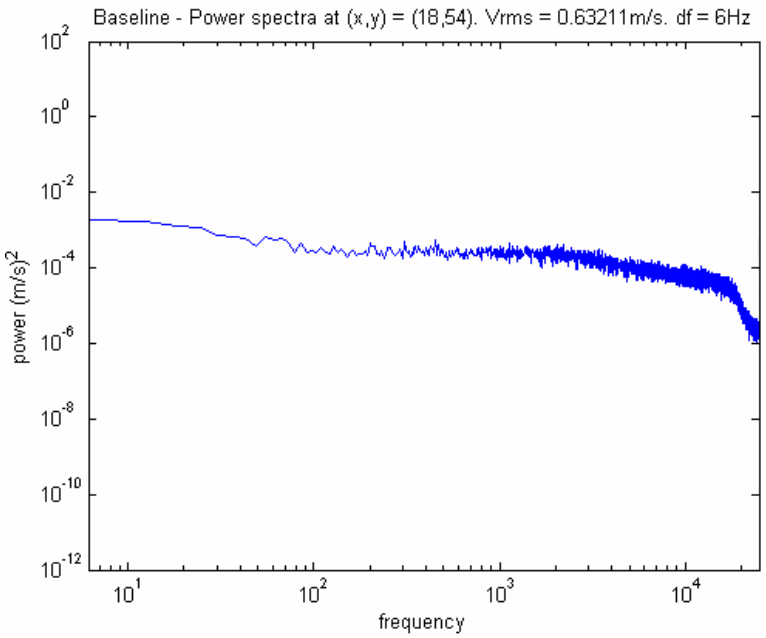

Figure 4.8: Velocity Spectra at Sample Point A in Zone 1 (in Free-stream)

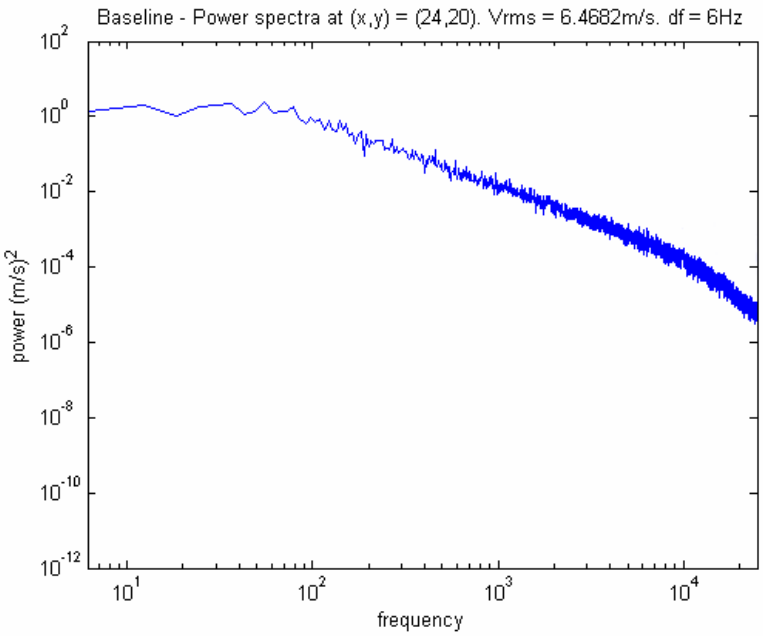

Figure 4.9: Velocity Spectra at Sample Point B in Zone 2 (Behind Braces)

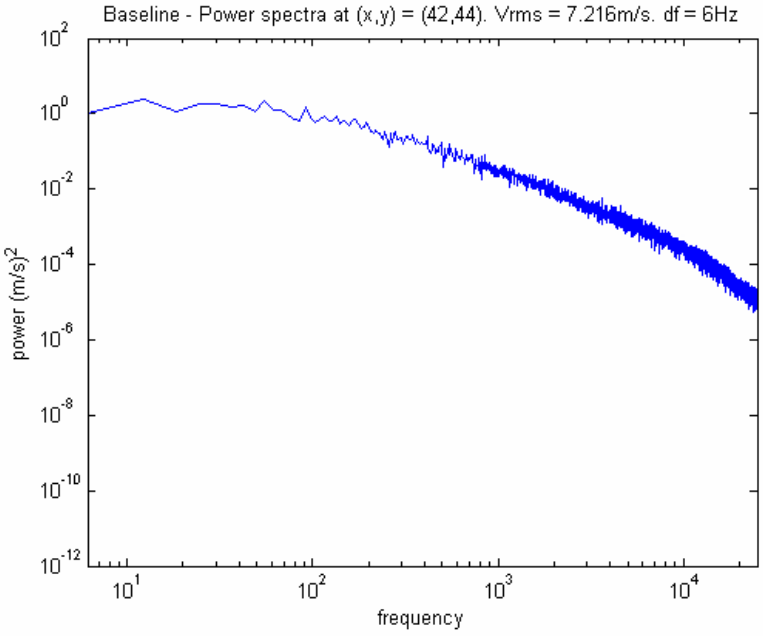

Figure 4.10: Velocity Spectra at Sample Point C in Zone 3 (Behind Truck)

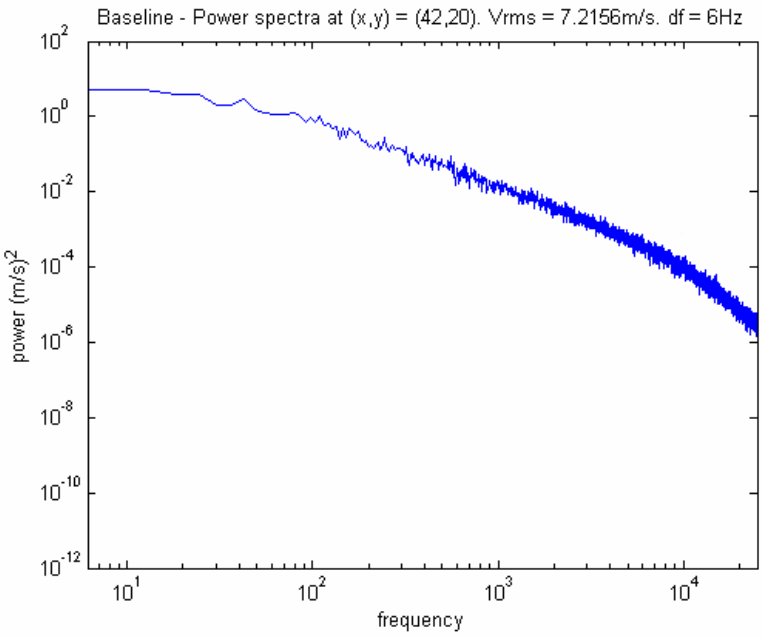

Figure 4.11: Velocity Spectra at Sample Point D in Zone 4 (Behind Door)

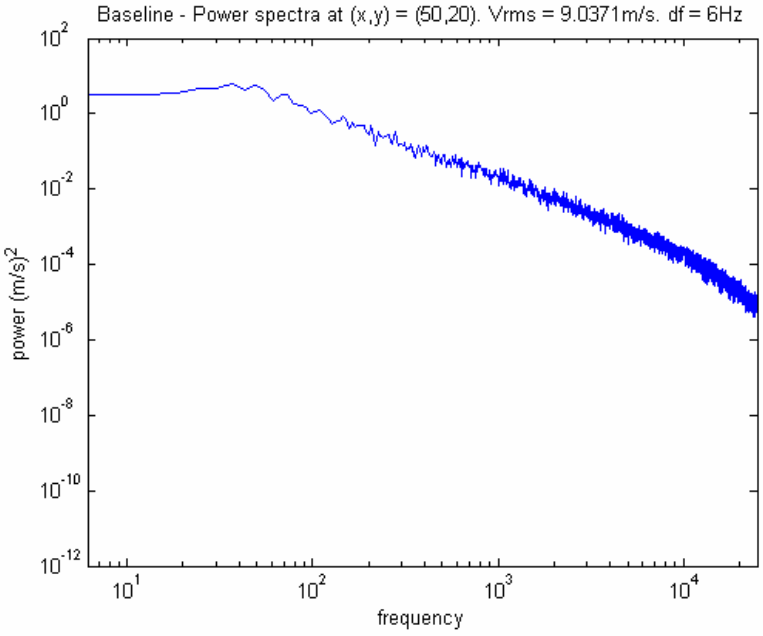

Figure 4.12: Velocity Spectra at Sample Point E in Zone 5 (Behind Main Strut)

4.1.1.4 Comparison of HWA / MPA Results

As explained in the previous chapter, velocity spectra for both configurations were broken into 1/12th octave bands and integrated over selected regions (behind noise control devices) to compare the hot-film measurements to Microphone Phased Array (MPA) results from Ravetta [9]. Figure 4.13 shows the change in dB between 'Baseline' and 'NCD' configuration from hot-film measurements and reduction in noise measured from MPA results behind the braces fairings. Results for frequencies lower than 2000 Hz were not compared since MPA data was not processed below that value and frequencies higher than 25000 Hz were not compared since they were considered to be outside the audible range. A consistent reduction in dB over the entire frequency range was noticed from the hot-film measurements whereas the reduction from acoustic MPA measurements shows frequency dependence. Since the hot-film measurements were taken at a plane 64" downstream of the landing gear where the turbulence was isotropic, the frequency history of the flow was lost as the vortices diffused. If the measurements were taken at plane closer to the landing gear where the turbulence was not isotropic, the reduction in dB due to hot-film measurements should show frequency dependence with a trend similar to the MPA results.

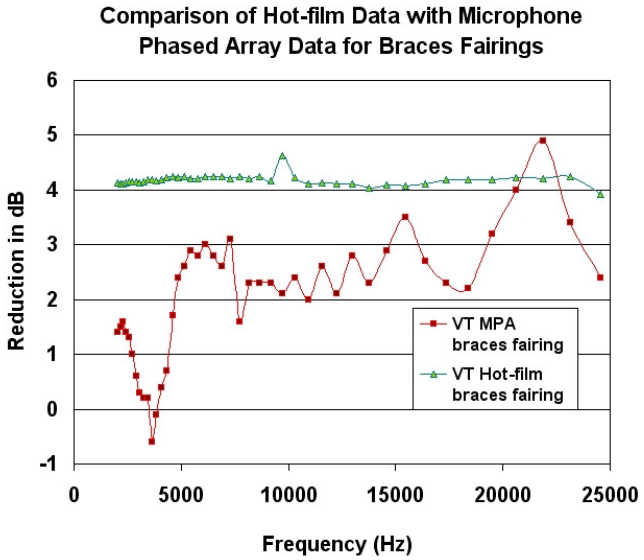

Figure 4.13: Comparison of Hot-film Data with MPA Data

Hot-film and MPA results were not compared behind the truck region since the difference in turbulence levels were not significantly (statistically) different.

4.1.2 Flow Visualization

Flow Visualization using tufts was performed on the 26% isolated high fidelity landing gear. The truck angle of the gear was 13 degrees and the free-stream Mach number in the test section was 0.16. Digital Videos of flow visualization were recorded and studied carefully using VLC media player. For better representation of the results, a Tecplot model of the landing gear for the 'Baseline' configuration was used and threads were drawn over the model representing tufts. The flow over a landing gear element was divided into three categories. Low or no turbulence represented was by blue colored threads, medium turbulence was represented by dark green threads and high turbulence or separation was represented by red color. The free-stream velocity is shown using three parallel arrows and the local velocity over an element is shown using single dotted arrow line in the direction of the flow. The results for the 'NCD' configuration are provided using still images of raw videos since no Tecplot model of the landing gear with noise control devices was available.

Figure 4.14 shows 26% landing gear Tecplot model with the flow moving from left to right. The blue threads show areas of flow attachment where as the red threads show areas of flow separation. The velocity arrows show the direction of flow over the wheel. High turbulence or separation was noticed on the wing side of the front wheel, whereas the ground side of the wheel did not show such high turbulence. The investigation by Lazos [10-12] the PIV experiments (VT-SWT) were performed with a truck angle of 0 degrees as compared to 13 degrees for the flow tuft visualization. The separation zone seems to have shifted from the ground side to the wing side of the wheels. The separated flow on the wing side of the first wheel was impinging on the wing side of the second wheel leading to a zone of attachment (low turbulence) there. The tuft on the side of the front part of the front wheel shows high turbulence since the back end of the tuft enters in

the hub region of the wheel where flow is expected to be unsteady. The tufts on the side of the ground and wing side of the front wheels show medium turbulence.

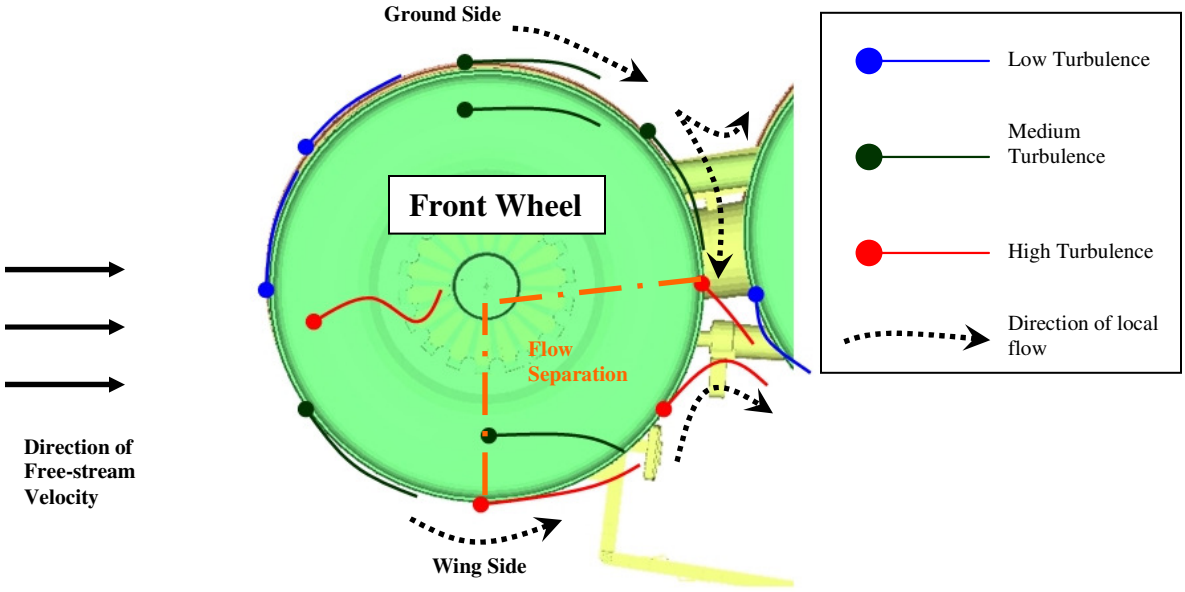

Figure 4.14: Flow Visualization over the Front Wheel

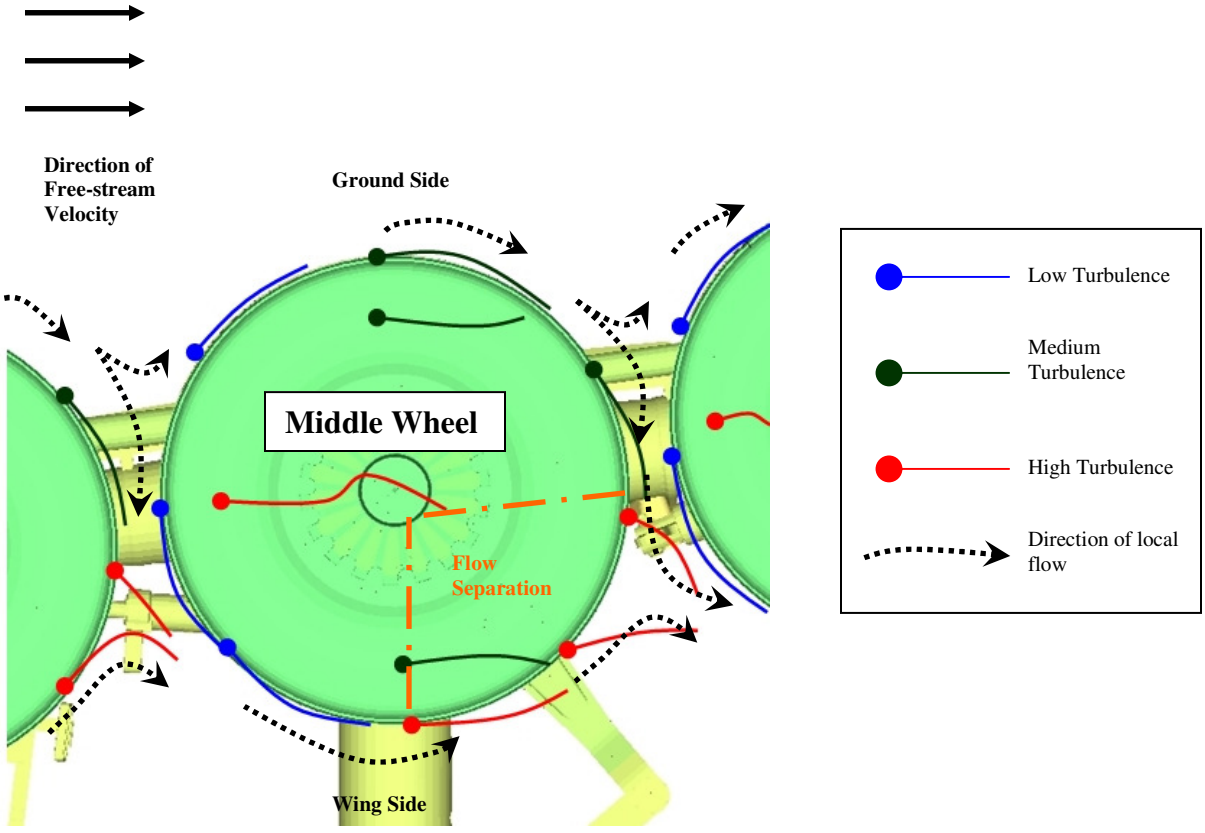

Figure 4.15: Flow Visualization over the Middle Wheel

Figure 4.15 shows flow visualization over the middle wheel. The separated flow over the wing side of the front wheel impinges on the wing side of the middle wheel and leads to attachment of flow. The ground side of the middle wheel shows areas of moderate turbulence. Some part of the flow ends up over the ground side of the back wheel and some ends up flowing towards the wing side of the back wheel. The flow on wing side of the middle wheel separates (see area of flow separation in Figure 4.15) and impinges on the back wheel. The tuft on the side of the front part of the middle wheel shows high turbulence and the tufts on the side of the ground and wing side show medium turbulence.

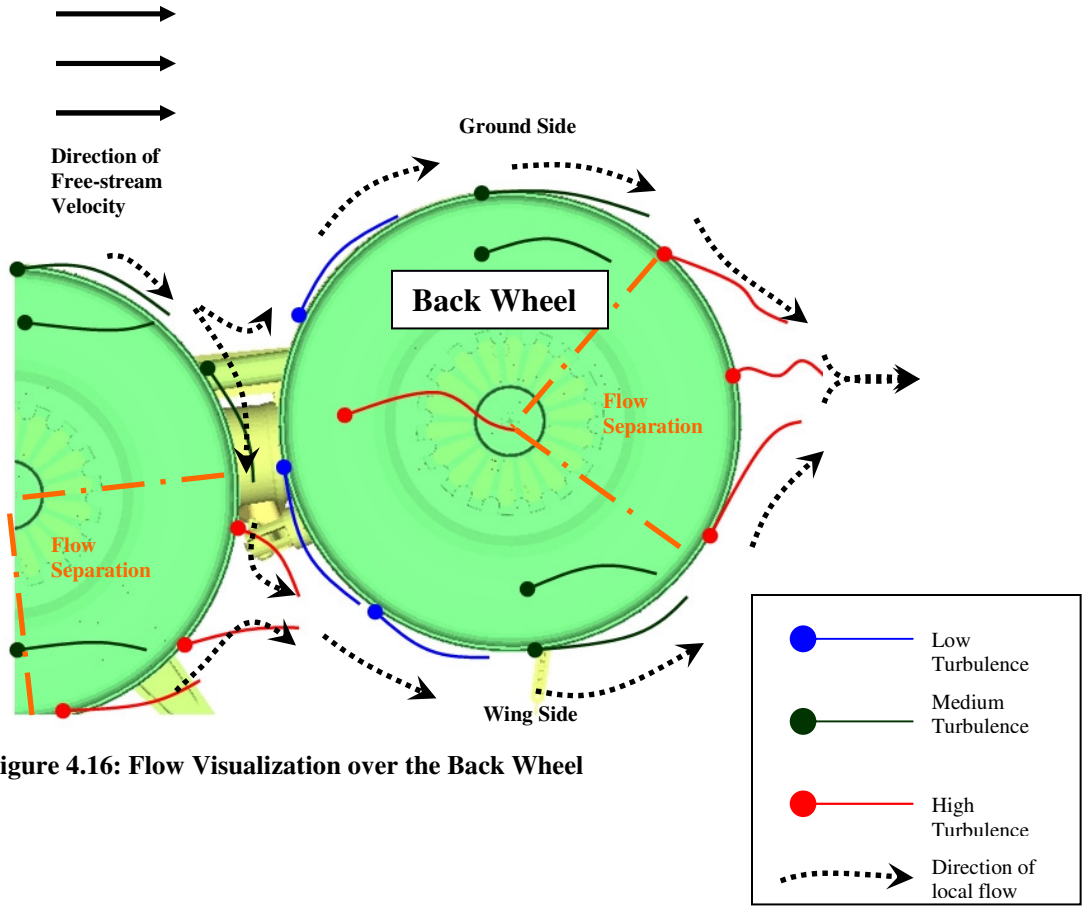

Figure 4.16: Flow Visualization over the Back Wheel

The separated flow from the middle wheel (wing side) causes the flow to attach on the wing side of the back wheel. The ground side of the back wheel sees low to moderate turbulent flow till it reaches the back side of the back wheel where it separates. The flow

from the wing side follows the same pattern. Between the wheels the flow is seen to be moving towards the wing side as shown in Figure 4.16. The highly turbulent flow (from the wing and the ground side) on the back end of the back wheel combines and can be noticed in the videos in form of entangled tufts. The tufts on the side of the front part of the back wheel show high turbulence and the tufts on the ground and wing side (on the side) show medium turbulence.

Thus in general, some part of the flow behind the front and the middle wheels on the ground side ends up towards the wing side of the next wheel. This flow ends up mixing with the incoming wing side flow and leads to higher turbulence levels behind the wheels (on the wing side). This area of higher turbulence was noticed in the wake of the gear behind the wheels on the wing side during hot-film turbulence measurements of both the 'Baseline' and 'NCD' configurations (Figure 4.5).

Figures 4.17 to 4.19 show flow visualization over the gear door. The top leading edge of the door has blue strings which were falling towards the ground while the threads on the other side (not seen in the picture) of the leading edge of the door were attached. After carefully observing the Tecplot model (Figure 4.18), it was found out that the gear door was at an angle to the incoming flow. Thus one side (not facing the brace) of the leading edge showed separation while the other side (facing the brace) had flow impinging on it and therefore the flow was attached. The side showing separation on the leading edge would face the ground when the gear was retracted. The bottom leading edge shows areas of high turbulence. In the center of the gear door, towards the wheels, an area of highly turbulent rotational flow was noticed and is shown using a curved flow arrow. The lower back end of the gear door shows areas of moderate to high turbulence. The middle and top portion of the trailing edge of the gear door show flow curling over the braces side and can be noticed in Figure 4.19.

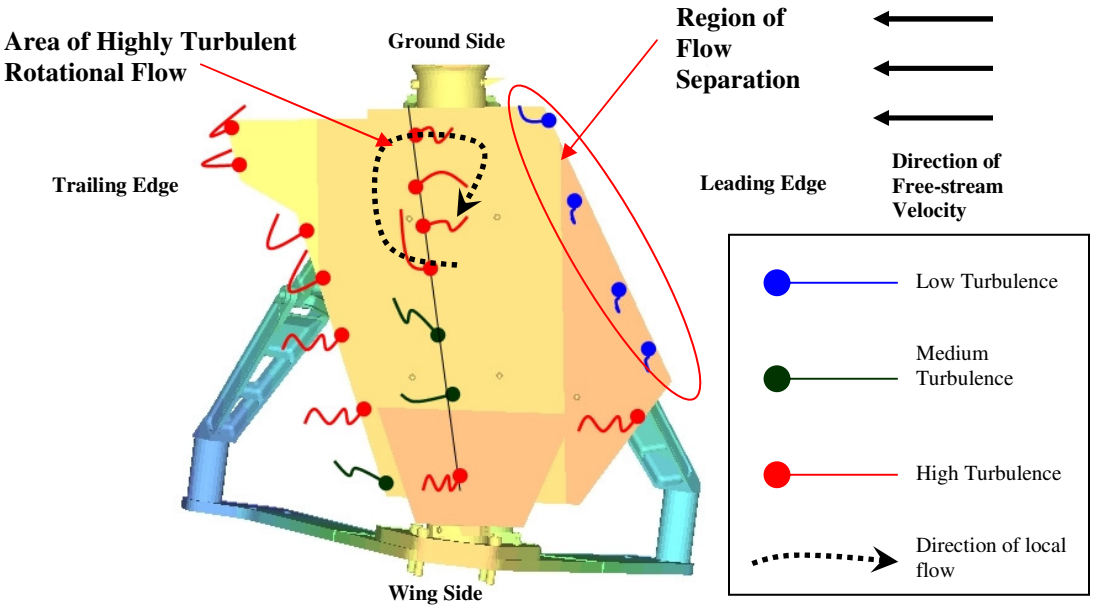

Figure 4.17: Flow Visualization over the Gear Door

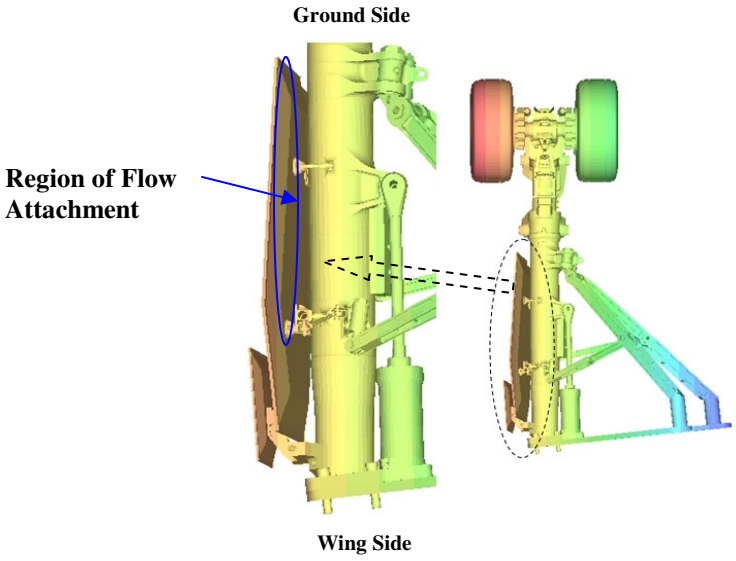

Figure 4.18: Tecplot Model of the Landing Gear (and Close-up of the Door) Looking Downstream (Flow in the Page)

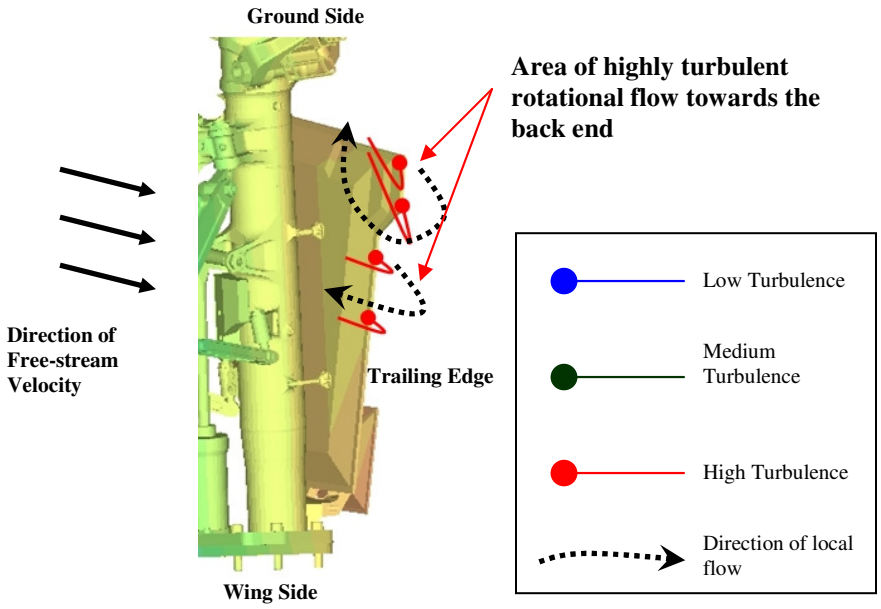

Figure 4.19: Flow Visualization over the Gear Door (Back End)

The highly turbulent flow over the back end of the gear door is also noticed in the turbulence contours (Figure 4.5) from hot-film measurements in the wake of the landing gear. Areas of lower wake velocity and higher pressure loss also correspond to this feature of the gear door.

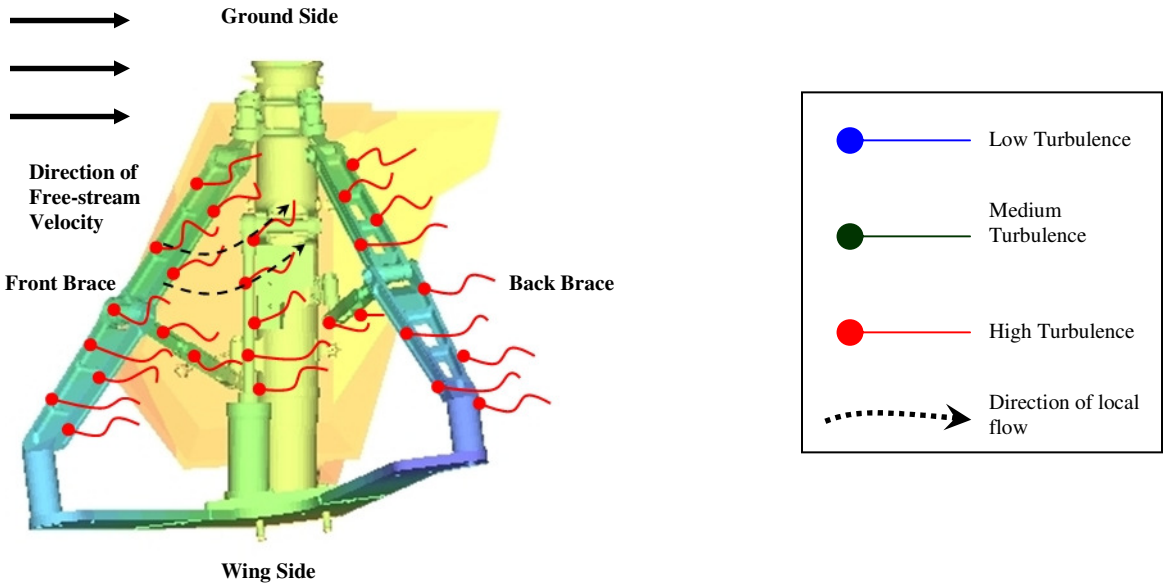

Figure 4.20: Flow Visualization over the Braces and the Lock Link

Figure 4.20 shows a schematic of flow visualization done over the braces and the lock link of the landing gear. The flow in general is highly turbulent with some flow over the cylinder-piston rod moving towards the ground side. The flow over the braces on the trailing edge was turbulent with tufts entangled with each other in adjacent pair.

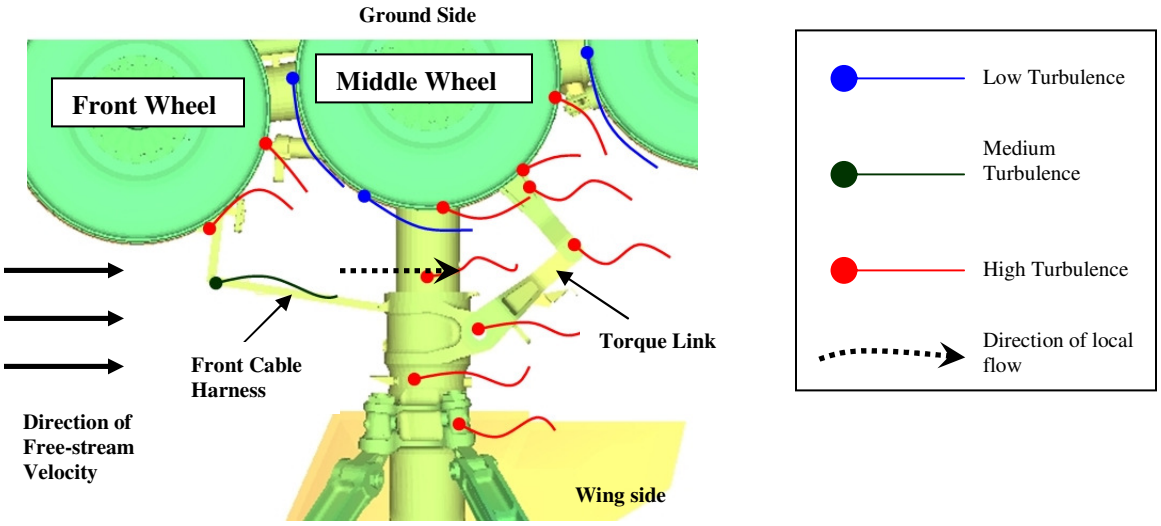

Figure 4.21: Flow Visualization using Tuft under the Wheels

Figure 4.21 shows a schematic of flow visualization using tuft for areas under the wheels. The flow over the front cable harness is moderately turbulent flow whereas flow over the torque link is highly turbulent.

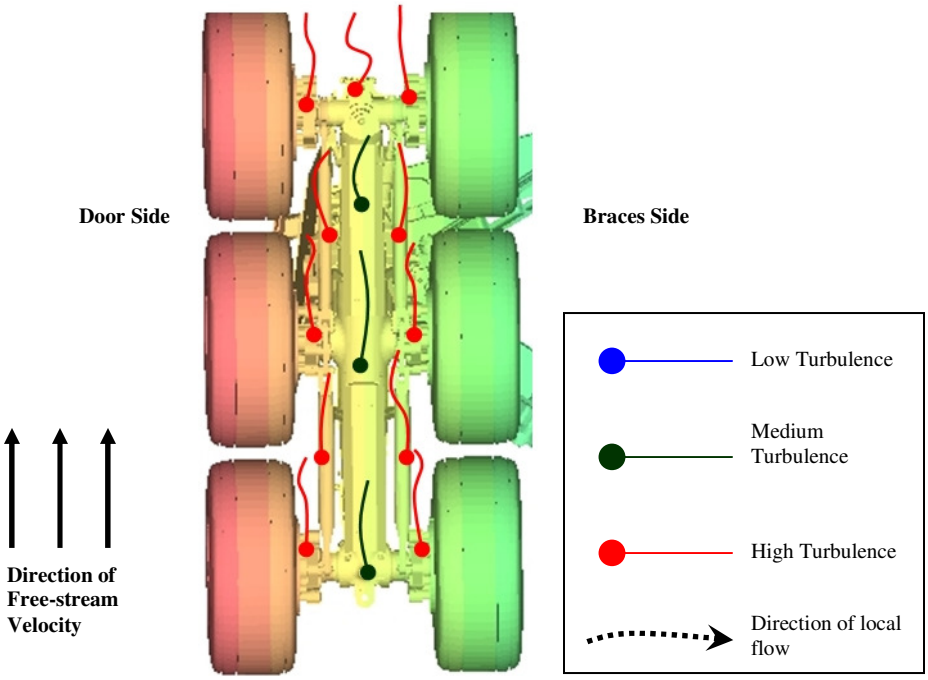

Figure 4.22: Flow Visualization over the Truck (View from ground looking towards the wing)

Figure 4.22 shows a schematic of the flow visualization over the truck of the 26% landing gear. The truck angle for the experiment was 13 degrees. The flow over the central part of the truck (front rock-guards and hydraulic valves, center truck and rear rock-guards and hydraulic valves) and the front truck was moderately turbulent. The flow over all the six brakes and axles, the brake rods and the rear truck was highly turbulent.

Figures 4.23, 4.24 and 4.25 show complete landing gear with arrows over different elements representing flow. Blue, green and red colored arrows are used to depict flow that causes attachment, some separation and separation respectively. Additionally, some elements are circled in color where the color depicts the type of flow leaving the circled elements.

Figure 4.23 shows the entire landing gear from the braces side. The free-stream flow is from left to right. On the ground side, flow impinges on the front wheel causing attachment on the front part (blue arrow). The flow on the ground side of the front wheel flows towards the back part of the front wheel, where some of it moves towards the wing side (through the space between the wheels) while the rest, impinges over the middle wheel (front part) on the ground side causing attachment. The attached flow from the ground side of the middle wheel moves towards the back part of the middle wheel where part of it moves towards the wing side (through the space between the middle and the back wheel), while the rest of it impinges on the front part of the ground side of the back wheel causing attachment. This attached flow then moves over the back part of the back wheel turning turbulent and causes separation.

On the wing side, the flow over the front part of the front wheel causes some attachment and turns turbulent as it flows towards the back part of the front wheel. This flow then mixes with the turbulent flow coming (between the wheels) from the ground side. Part of this mixed flow impinges on the front part of the wing side of the middle wheel causing attachment and the rest continues downstream without interacting with the gear wheels (since they are at an angle of 13 degrees). The part of the flow close to the wing side of the middle wheel moves over the back part of the middle wheel on the wing side while

turning turbulent and mixes with the incoming turbulent flow (between the middle and the back wheel). Part of the mixed flow then continues downstream without interacting with the gear wheels while some part causes attachment on the front part of the back wheel (wing side). The attached flow continues to flow over the back part of the back wheel and turns turbulent. This flow then mixes with the turbulent incoming flow from the ground side and flows downstream.

Over the braces, the incoming (laminar) flow interacts with the front brace causing attachment on the leading edge of the front brace. The flow leaving the trailing edge of the front brace is highly turbulent and impinges on the leading edge of the back brace. Part of the flow leaving the top portion of the front brace was noticed to flow upwards towards the center of the truck. The flow leaving the trailing edge of the back brace is highly turbulent and flows downstream without further interacting with the landing gear.

The gear door was at an angle to the incoming flow which impinges on the top part leading edge (circled in blue in Figure 4.23) causing flow attachment. The top part of the trailing edge of the door shows flow curling towards the braces side from the door side. The curled flow mixes with the inclined flow coming from the top part of the front brace.

The front cable harness which lies upstream of the main strut causes moderately turbulent flow to impinge on the main strut. The flow in the wake of the main strut is turbulent and impinges over the torque link and continues downstream to mix with the already mixed flow coming from the top part of the trailing edge of the door and the top part of the front brace.

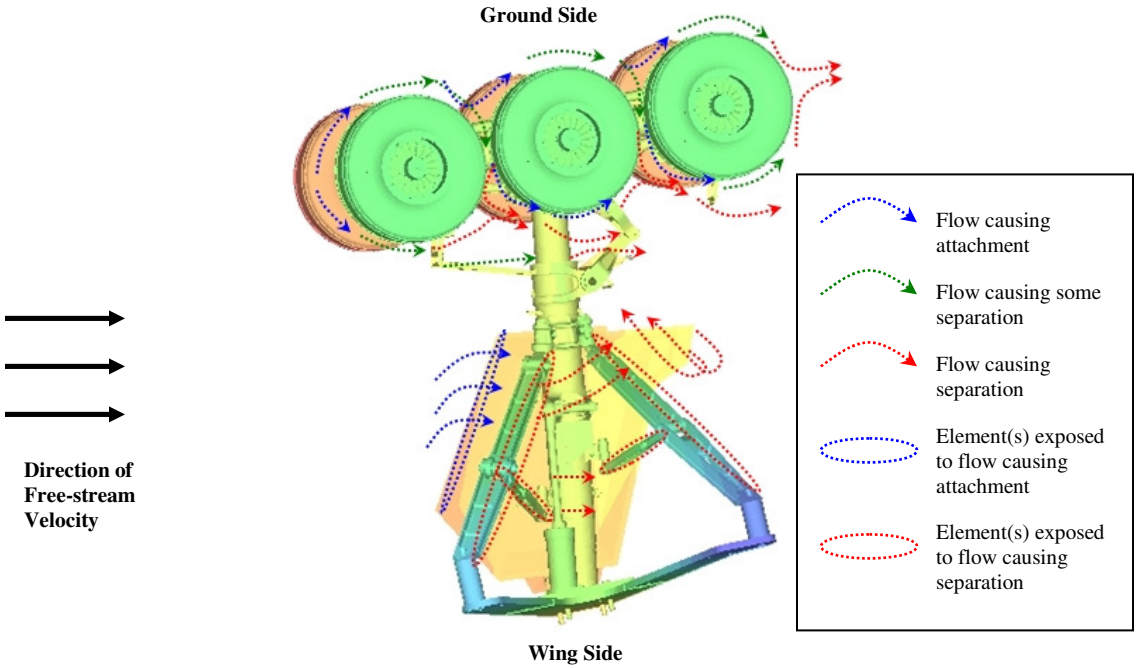

Figure 4.23: Landing Gear with Flow Vectors seen from the Braces Side

Figure 4.24 shows the landing gear with flow vectors from the door side. The flow over the door side wheels is similar to the flow over the wheels on the braces side (explained earlier). The ground side of the leading edge of the door on the door side shows regions of very low or no flow. This region is represented using a dotted red line. In the center of the gear door towards the ground side, regions of turbulent curved flow were noticed. This region of curved separated flow (represented using a curved red arrow) corresponds to regions of low wake velocity (or high pressure loss) seen in Figure 4.4 (or Figure 4.6) and regions of high turbulence seen in Figure 4.5 (behind the door). On the ground side of the trailing edge of the gear door, flow was noticed to curl on the back side of the door. The curled door interacts and mixes with the turbulent flow behind the main strut and the inclined flow coming from the ground side of the front brace (explained earlier).

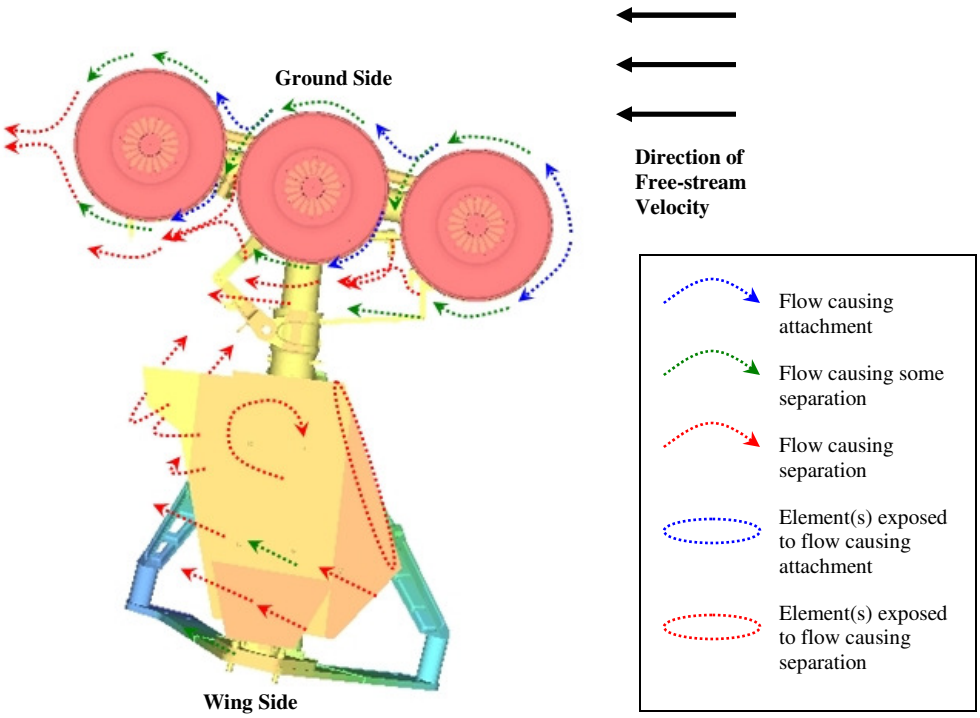

Figure 4.24: Landing Gear with Flow Vectors seen from the Door Side

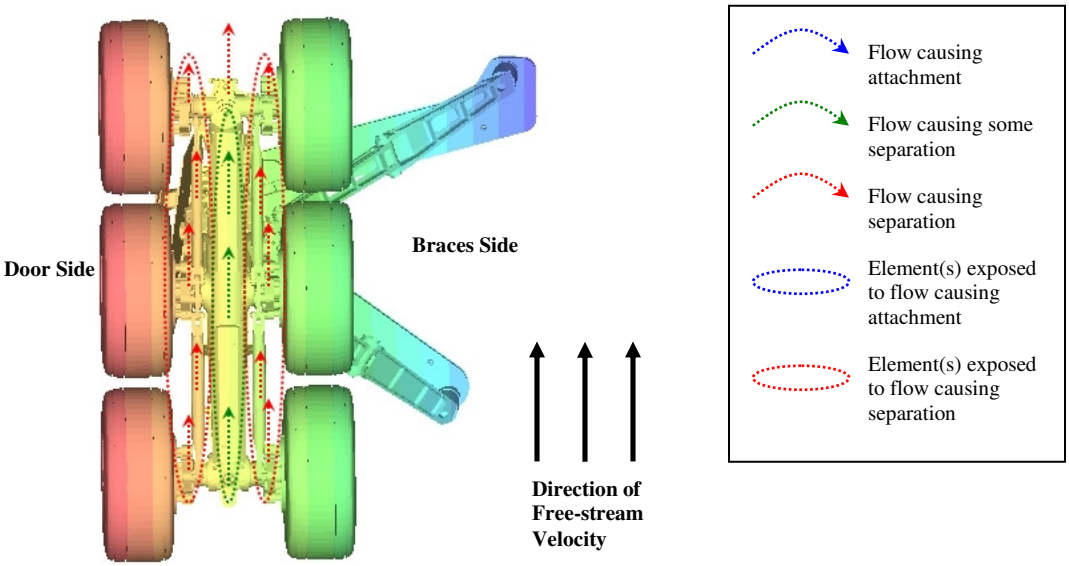

Figure 4.25: Landing gear with Flow Vectors seen from the Ground side

Figure 4.25 shows the landing gear with flow vectors as seen from the ground side. The free-stream velocity was from top to bottom. The center of the truck over the rock guards and hydraulic valves, center truck and rear rock-guards and hydraulic valves circled in

green show regions of medium turbulence (circled in green). The flow over all the six brakes and axles, the four brake rods and the rear truck were highly turbulent and are represented using red regions. The dotted arrows in each of the regions show the direction of the local velocities over the individual elements.

Figure 4.26 is a still from the raw video acquired during flow visualization using tuft over the braces noise control devices in the VT-SWT. The picture shows tuft (sewed over the membrane based fairings) which were steady, smooth and attached on the surface of the membrane indicating no or very little separation.

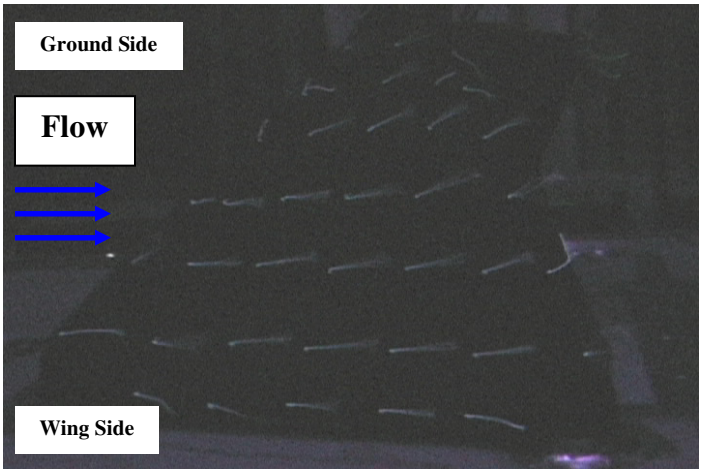

Figure 4.26: Flow Visualization using Tuft over Braces Noise Control Devices

Figure 4.27 shows a still image of the flow visualization using tuft over the braces noise control devices in the VT-SWT. The tuft over central portion of the noise control devices (over the front rock-guards and hydraulic valves, center truck and rear rock guards and hydraulic valves) shows smooth attached flow. The tuft towards the sides (six brakes and axles, the brake rods and rear truck) of the noise control device show some unsteadiness and separation.

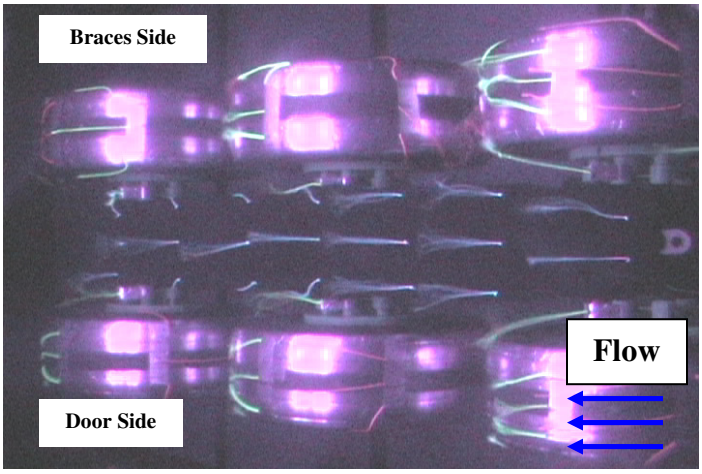

Figure 4.27: Flow Visualization using Tuft over Truck Noise Control Devices

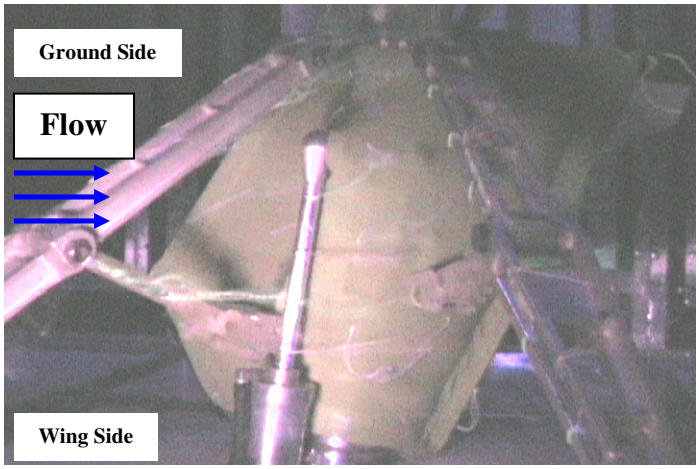

Figure 4.28: Flow Visualization using Tuft over Strut Noise Control Devices

Figure 4.28 shows a still image of the strut noise control devices on the landing gear in the VT-SWT. Flow visualization was performed using tuft on the strut noise control devices and a digital camera was used to capture the videos. The image shows attached, smooth flow on the leading edge of the noise control device. The strut region covered by the membrane shows some regions of unsteady flow towards the ground side (where the flow from the ground side of the leading brace was noticed to move towards the truck). Some of the tuft downstream of the main strut was noticed to fall towards the tunnel floor indicating the possibility of separation.

4.1.3 Particle Image Velocimetry

Particle Image Velocimetry measurements were taken at six different locations over the 13% landing gear without the door and a truck angle of 0 degrees. For every run, 300 pairs of images were collected and correlated by double pass using the DPIV software. Contours of average velocity, velocity vectors and velocity root mean square (U_{RMS} and V_{RMS}) contour maps for 300 samples are presented. Instantaneous velocity contours and instantaneous vectors for a sample image pair are also presented for all the images. Results from Lazos [10-12], who presents mean flow features around the inline wheels of a four wheel landing gear (conducted at NASA Langley) are compared with the results obtained from data acquired around the wheels with a truck angle of zero degrees (wheels inline) at VT-SWT.

The NASA Langley study was conducted in the Basic Aerodynamic Research Tunnel (BART) which is an open-circuit wind tunnel with a test section of 71- by 102-cm and a length of 305 cm. 31% scale model of only the wheels and the truck (Boeing 757) were used at a free-stream velocity of 29 m/s which led to a blockage of 15%. The absolute diameter of the wheels was 304 mm which led to a Reynolds number (based on wheels) of 6×10^5. The VT-SWT study was conducted on the 13 % model 777 main landing gear model with zero degrees truck angle at a free-stream velocity of 56 m/s and a blockage of 6%. The diameter of the wheels was 355 mm which led to a wheel based Reynolds number of 6.5×10^5.

Figure 4.29 shows contours of average velocity with streamlines and average velocity vectors for 'Large View between Braces'. The 8- by 8-inch, 300 pairs of 1000- by 1000-pixel images were correlated and a one-sigma filter was used for average results. Some areas of bad correlations and/or bad vectors due to reflections of the laser beam from the landing gear elements and/ or loss of laser sheet show missing data. The flow is from left to right and the two circles (one on the left and the other on the right) in the image plane representing the junctions between the lock link and the front or the rear brace. Contours of mean velocity show the front brace wake with velocity lower than free-stream incident

on the back brace. Figure 4.30 shows the root mean square of the velocity (contour map) calculated over 300 samples.

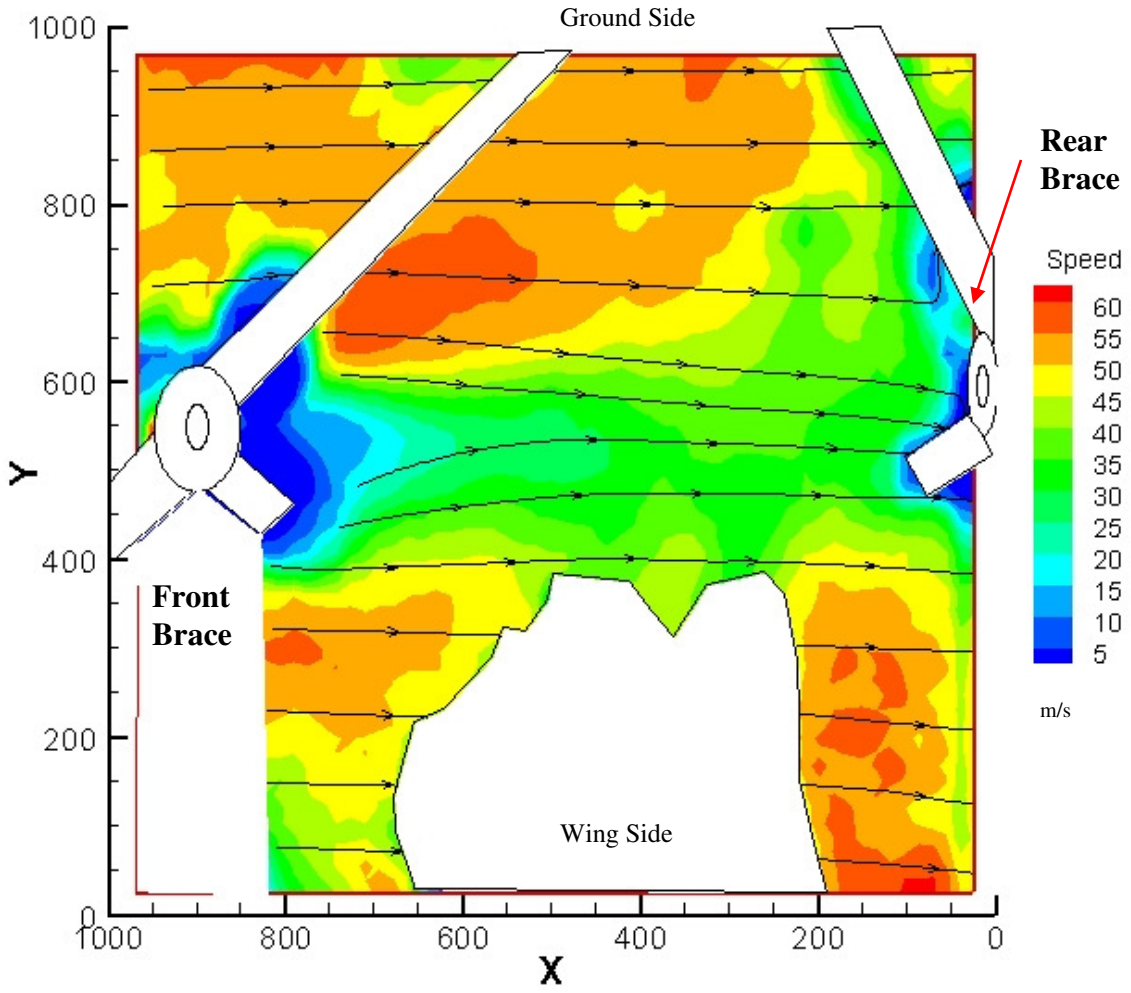

Figure 4.29: Average Velocity Contours (with Streamlines) for 'Large View between Braces' (8- by 8-inch Window)

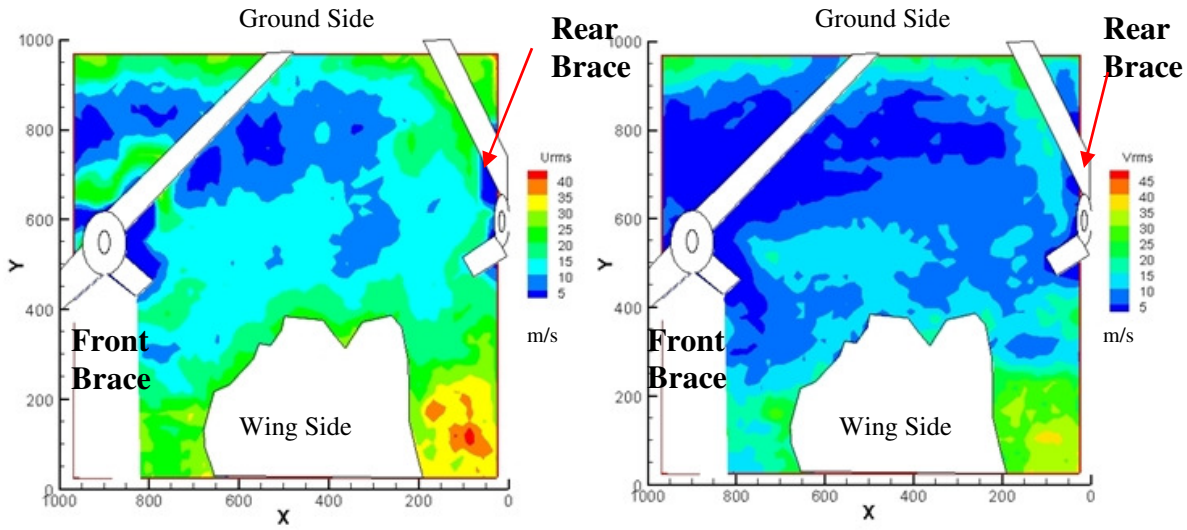

Figure 4.30: Root Mean Square Velocity Contours Calculated from 300 Samples. U_{RMS} (left) and V_{RMS} (right) for 'Large View between Braces' (8- by 8-inch Window)

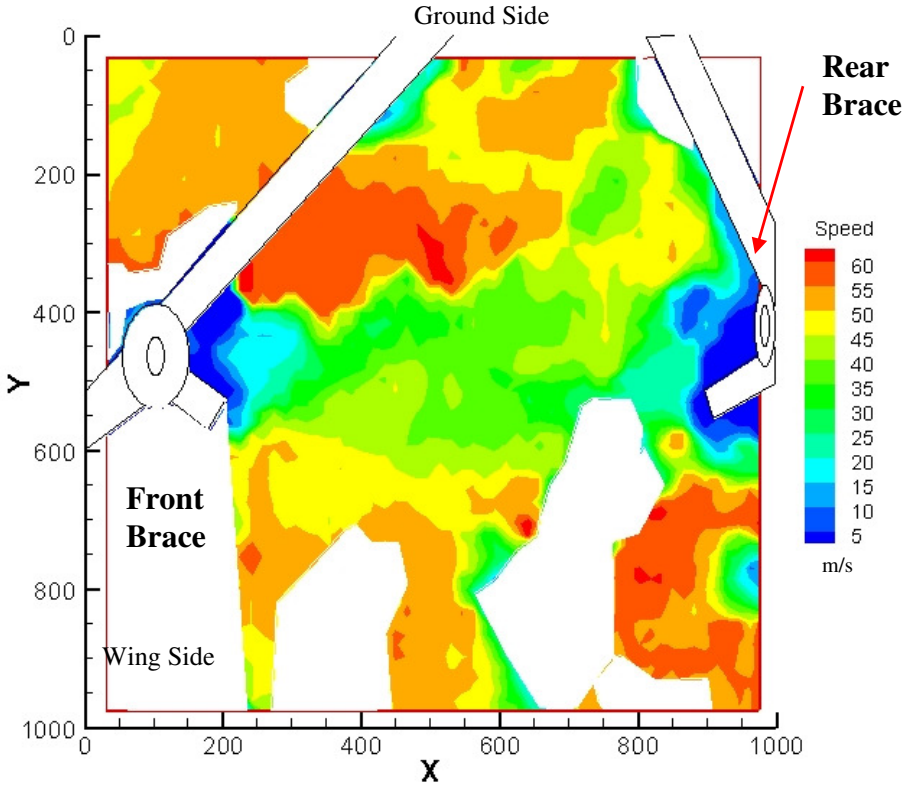

Figure 4.31: Instantaneous Velocity Contours for 'Large View between Braces' (8- by 8-inch Window)

Figure 4.31 and 4.32 show contours and vectors of instantaneous velocity for 'Large View between Braces'. The CCD camera acquired pairs of images which were correlated to give one such instantaneous velocity contours or vectors. The average results were obtained by using 300 similar instantaneous files.

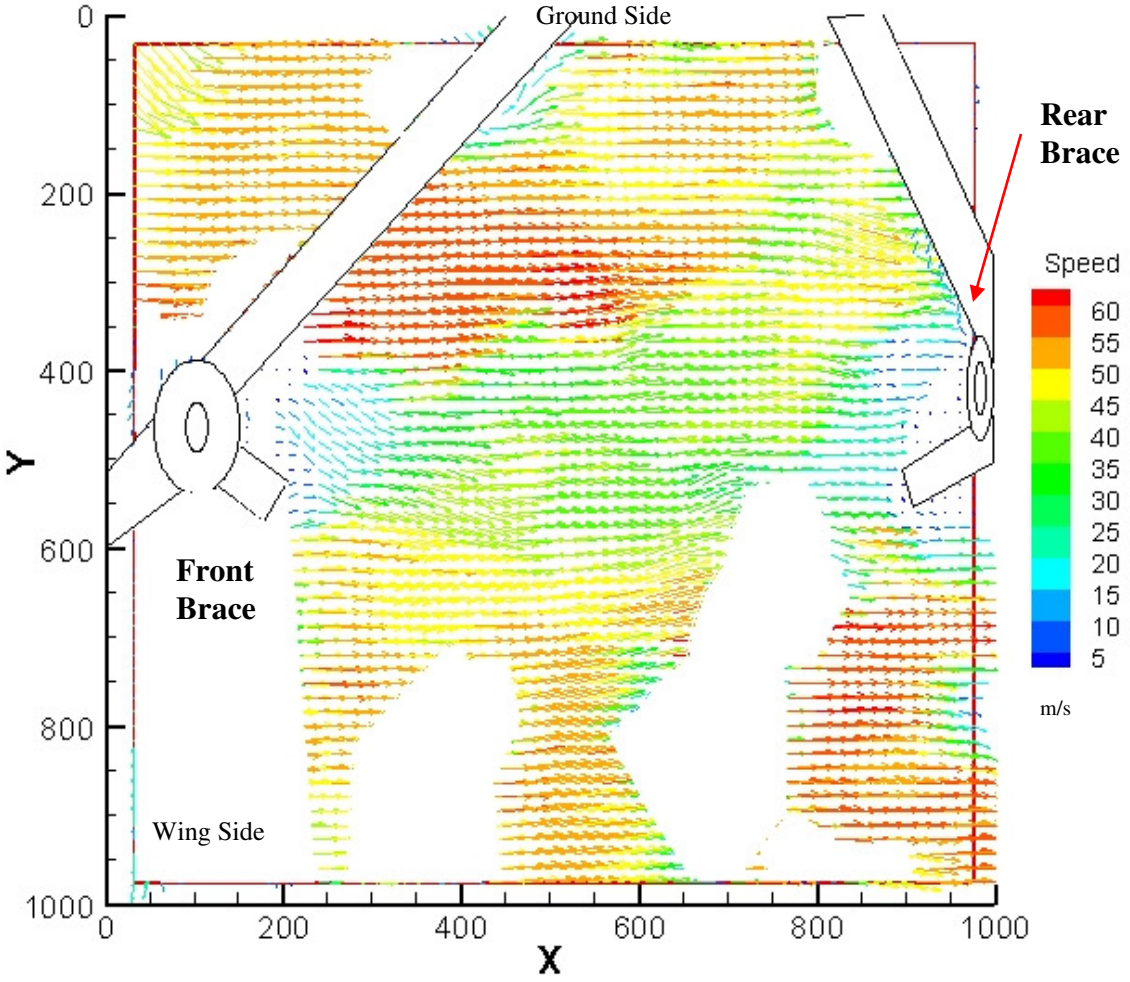

Figure 4.32: Instantaneous Velocity Vectors for 'Large View between Braces' (8- by 8-inch Window)

Figure 4.33 shows a set of images from 'Large View between Braces'. The free-stream flow in each image is from left to right and the front and back brace are labeled. Vortex visualization was accomplished by subtracting the convection velocity from the velocity field. Time independent (random) velocity fields were analyzed and each gave a vortex in the wake of the front brace. The images were then arranged according to the position of the vortex. The figure shows vortex (shown in black box) shed from the front brace travel in the wake (of the front brace) and collapse on the back brace. This phenomenon was

considered to be the main noise generating mechanism in the back brace by Ravetta [8] who showed that by removing the front brace (and therefore eliminating the wake interaction) the noise levels reduced.

Ground Side

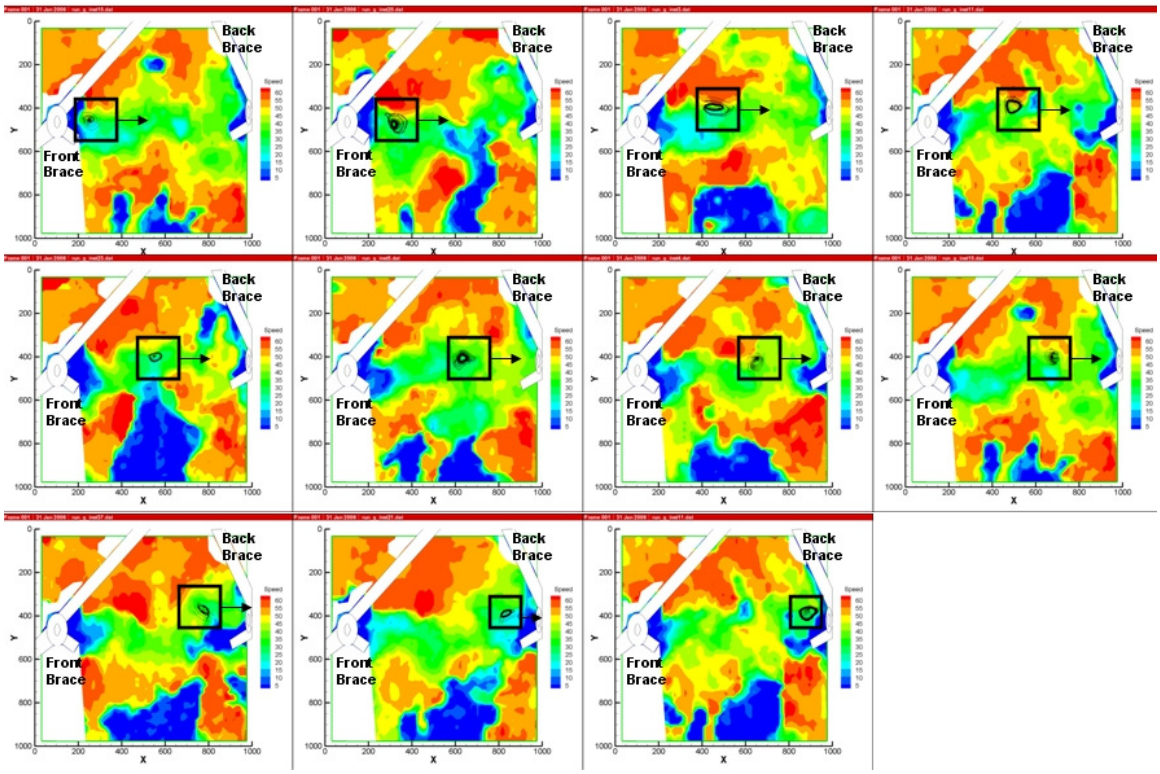

Wing Side

Figure 4.33: Vortex Shed from the Front Brace moving towards the Back Brace in 'Large View between Braces' (8- by 8-inch Window) determined from PIV Data

Figure 4.34 shows the average velocity contours with streamlines for 'Vertical Plane Close View' from instantaneous 300 samples. Six hundred 2- by 2-inch images taken by the 1000- by 1000-pixel resolution CCD camera were correlated and calibrated by the DPIV software to give 300 instantaneous velocity contours and vectors (shown in Figures 4.36 and 4.37). The free-stream flow is from left to right and the measurement plane is in the wake of the front brace and its junction with the front lock link. Figure 4.35 shows the root mean square velocity in the x and y directions. This velocity fluctuation (U_{RMS} and V_{RMS}) portrays the unsteady nature of the flow in the wake (behind the front brace and its junction).

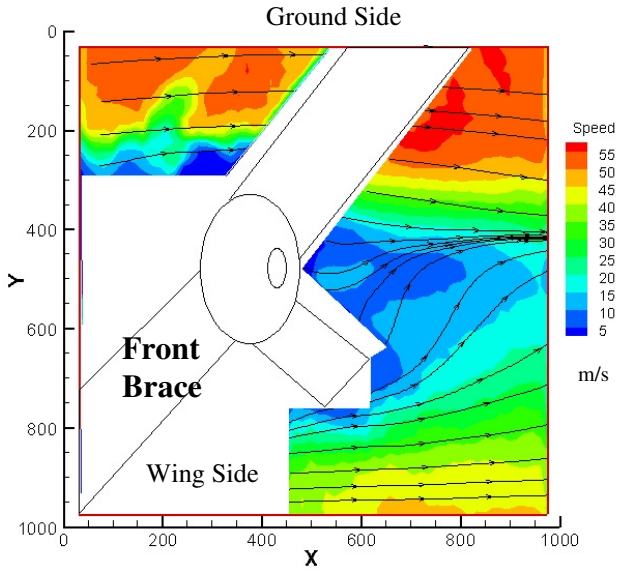

Figure 4.34: Average Velocity Contours (with Streamlines) for 'Vertical Plane Close View' (2- by 2-inch Window)

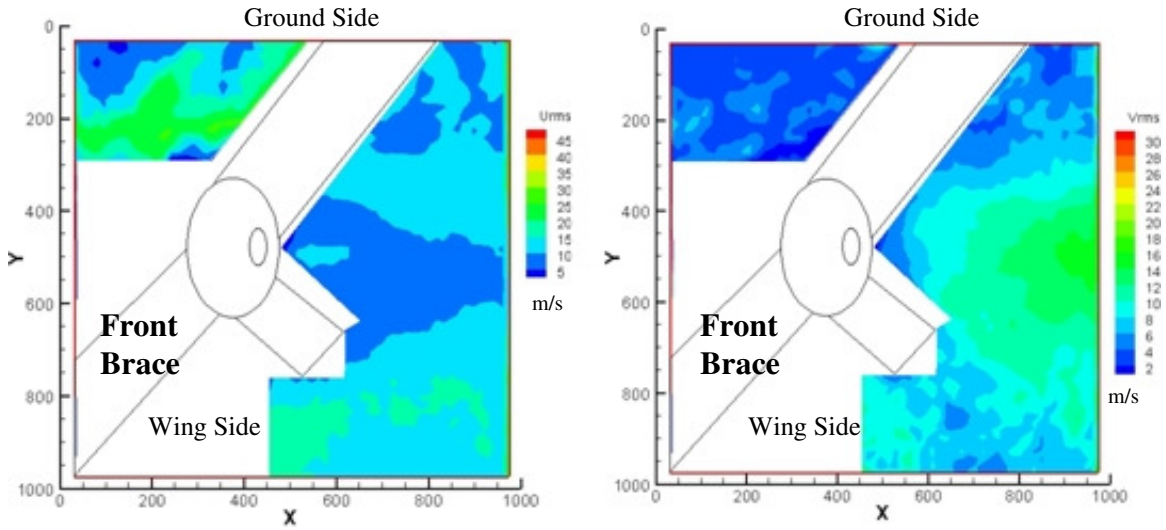

Figure 4.35: Root Mean Square Velocity contours calculated from 300 samples. U_{RMS} (left) and V_{RMS} (right) for 'Vertical Plane Close View' (2- by 2-inch Window)

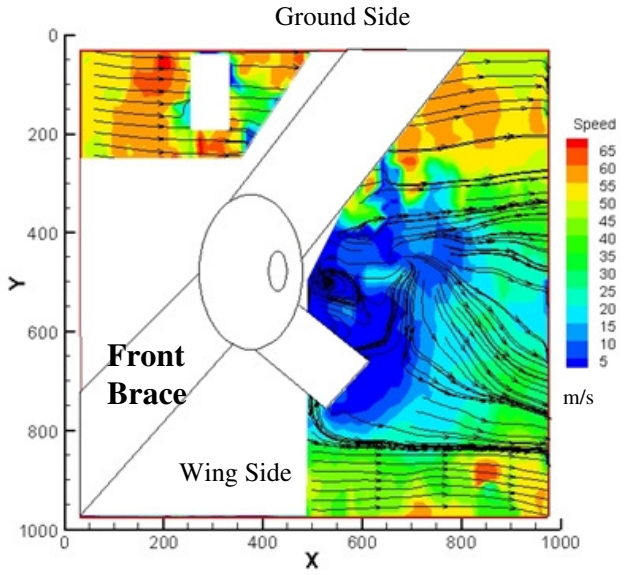

Figure 4.36: Instantaneous Velocity Contours (with Streamlines) for 'Vertical Plane Close View' (2- by 2-inch Window)

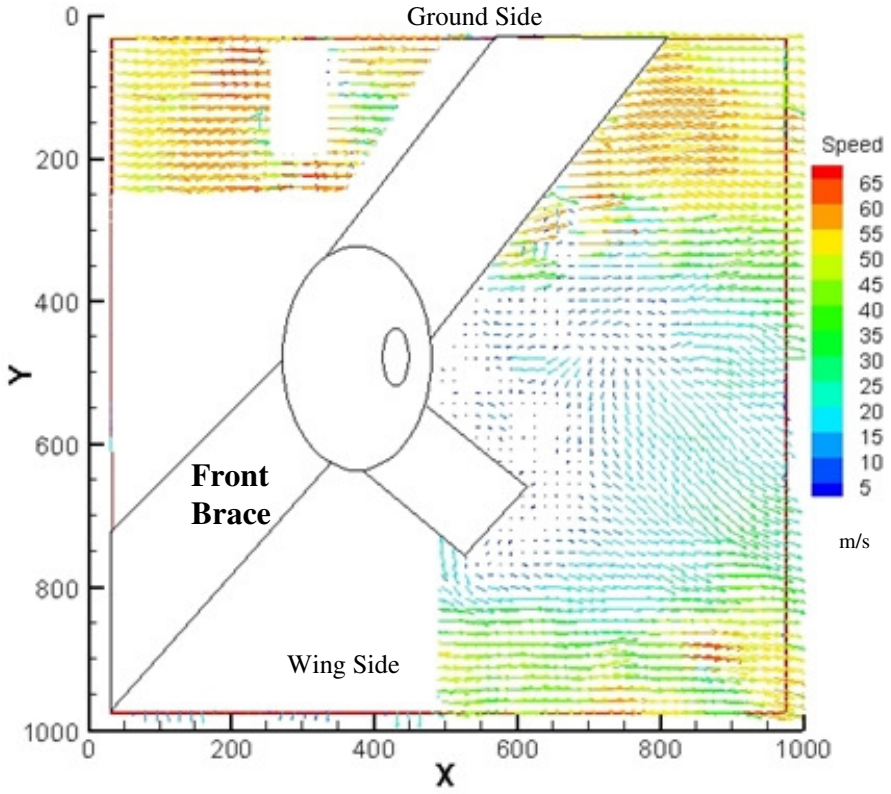

Figure 4.37: Instantaneous Velocity Vectors for 'Vertical Plane Close View' (2- by 2-inch Window)

Figure 4.38 shows an instantaneous vortex shed from the front brace. The visualization was done by choosing an instantaneous velocity field file and subtracting the convection velocity from it.

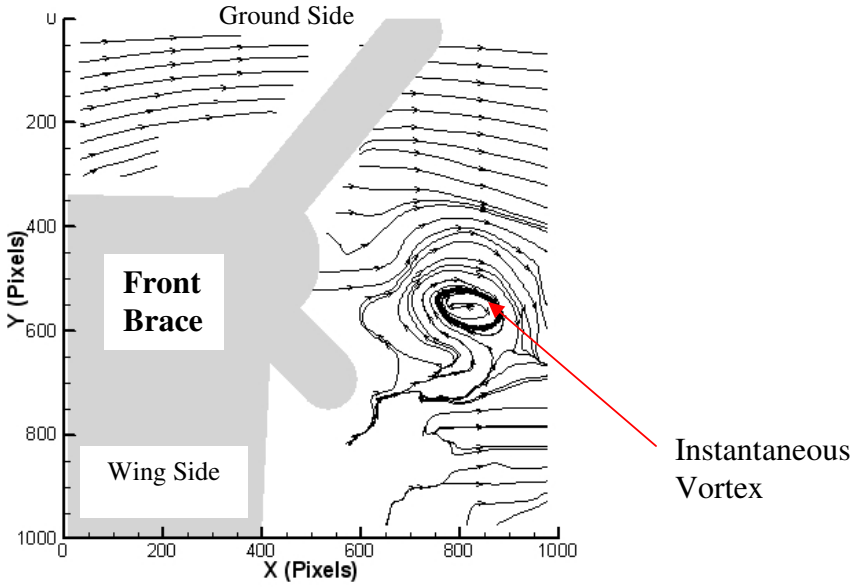

Figure 4.38: Instantaneous Vortex Shed from the Front Brace as seen in 'Vertical Plane Close View' (2- by 2-inch Window)

Figure 4.39 shows average velocity contour plot with streamlines for the 'Vertical Plane Wheels View' in which the free-stream flow is from left to right. The average of 300 samples was performed by using one-sigma rejection filter for the average velocity calculations. The separation and attachment regions were identified using streamline tracing. Figure 4.40 shows average PIV results presented by Lazos [10-12] during an investigation conducted around the inline wheels of a four wheel landing gear at the NASA Langley facility with a free-stream velocity of 29 m/s. PIV measurements were taken at VT-SWT with a free-stream velocity of 55 m/s over the 13% main landing gear and a truck angle of zero degrees (wheels inline). Red box in Figure 4.40 highlights the area used to compare with the VT-SWT results. Even though the dimensions of the facilities and the free-stream velocities differ, the results are noticed to be remarkably similar.

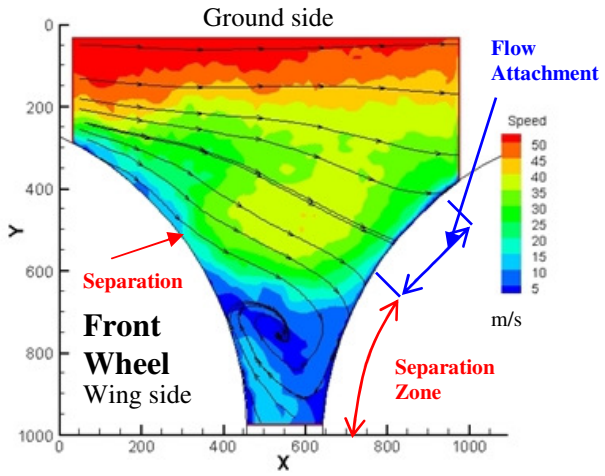

Figure 4.39: Average Velocity Contours (with Streamlines) for 'Vertical Plane Wheels View' (3.5- by 3.5-inch Window)

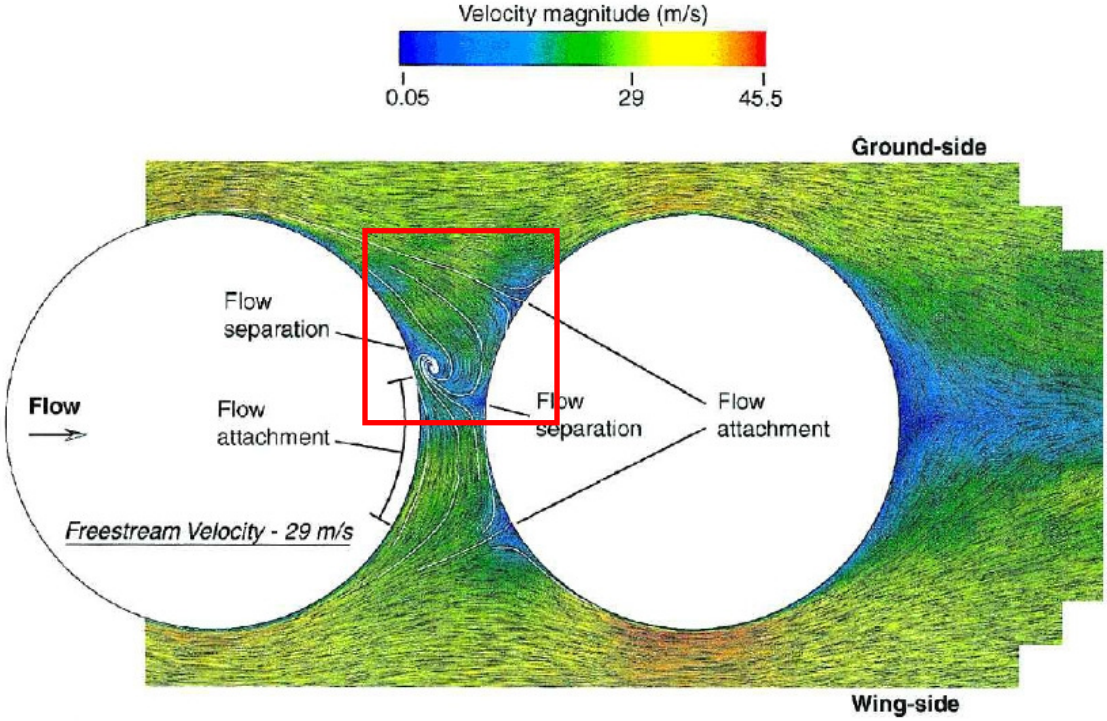

Figure 4.40: Average Velocity and Streamlines in the DPIV Plane from Lazos [10], (NASA Langley, 2002). Red Box shows the Area Analyzed in 'Vertical Plane Wheels View' (VT-SWT Data)

Contour maps for the root mean square of the velocities in the x- and y-directions are presented in Figure 4.41. The root mean square velocity results are also similar to the results presented by Lazos [11].

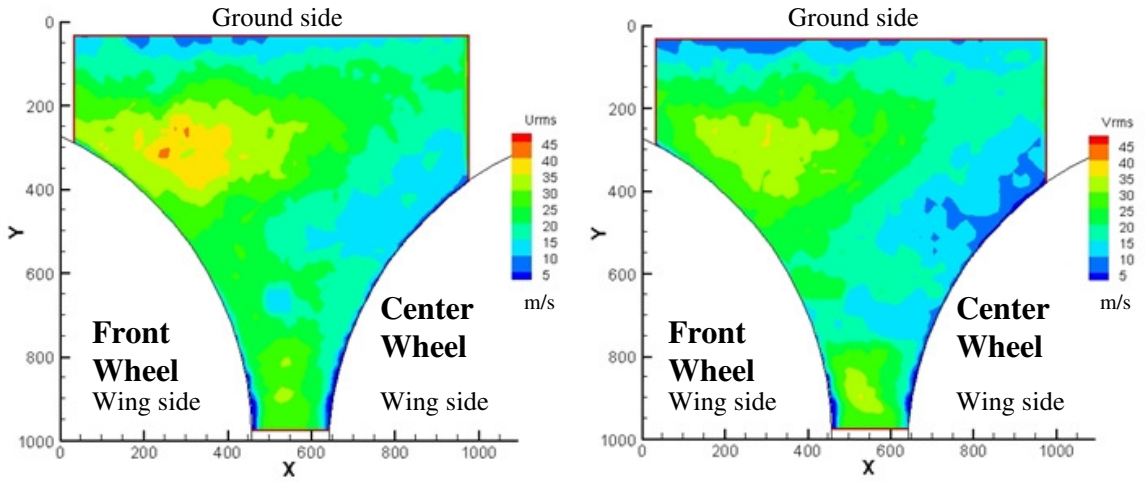

Figure 4.41: Root Mean Square Velocity contours calculated from 300 samples. U_{RMS} (left) and V_{RMS} (right) for 'Vertical Plane Wheels View' (3.5- by 3.5-inch Window)

A pair of 3.5- by 3.5-inch recorded images were correlated and calibrated to give an instantaneous velocity contour plot, which is shown in Figure 4.42. The instantaneous velocity fields (example in Figure 4.43) were analyzed and an instantaneous vortex was noticed between the two wheels. The vortex was noticed to translate between the front and the middle wheel and is shown in Figure 4.44. The collision of the vortex on the front and the back wheel, and its translation causes rubbing of turbulent eddies against the wheel surface. This non-stationary vortex was also noticed during the investigation conducted by Lazos [10-12] and was believed to be a contributor of noise radiated towards the ground.

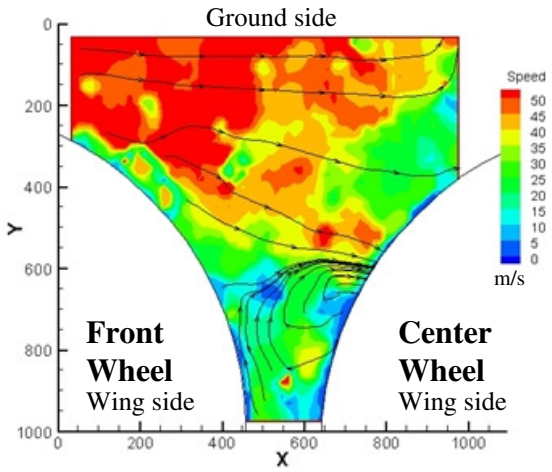

Figure 4.42: Instantaneous Velocity Contours (with Streamlines) for 'Vertical Plane Wheels View' (3.5- by 3.5-inch Window)

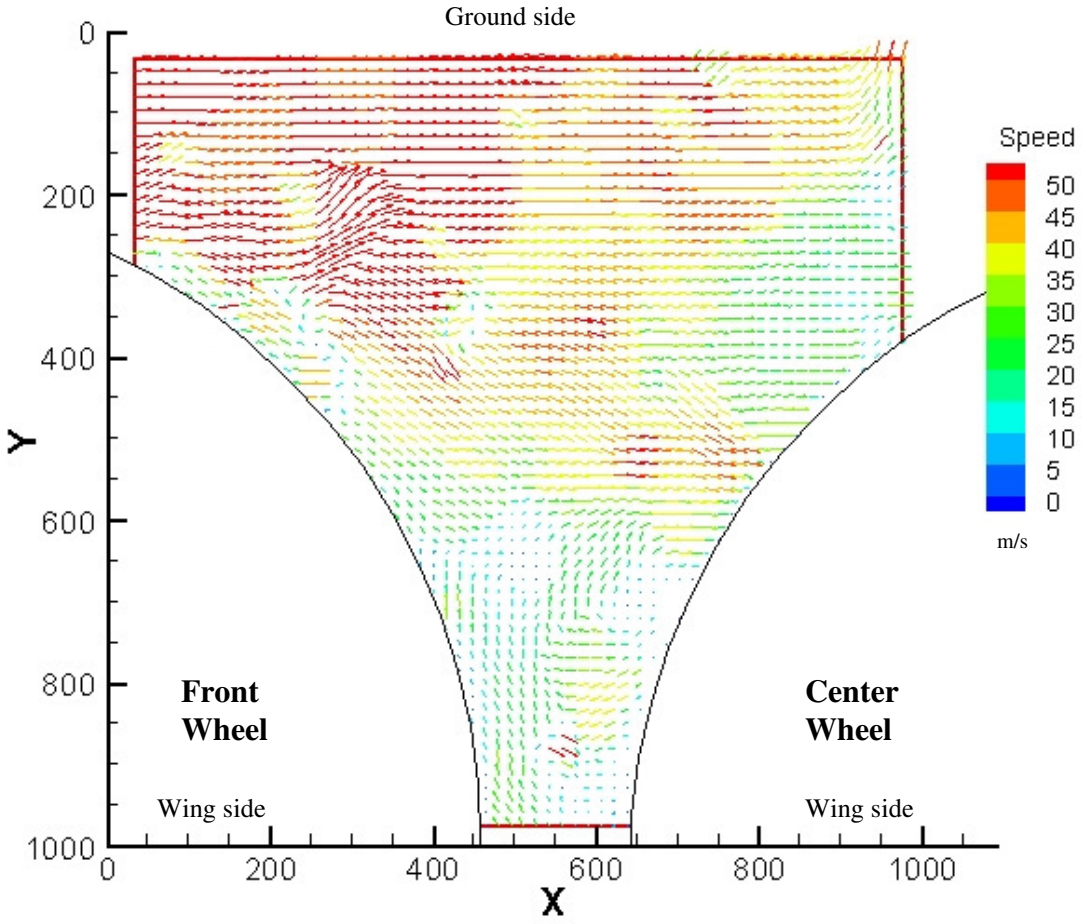

Figure 4.43: Instantaneous Velocity Vectors for 'Vertical Plane Wheels View' (3.5- by 3.5-inch Window)

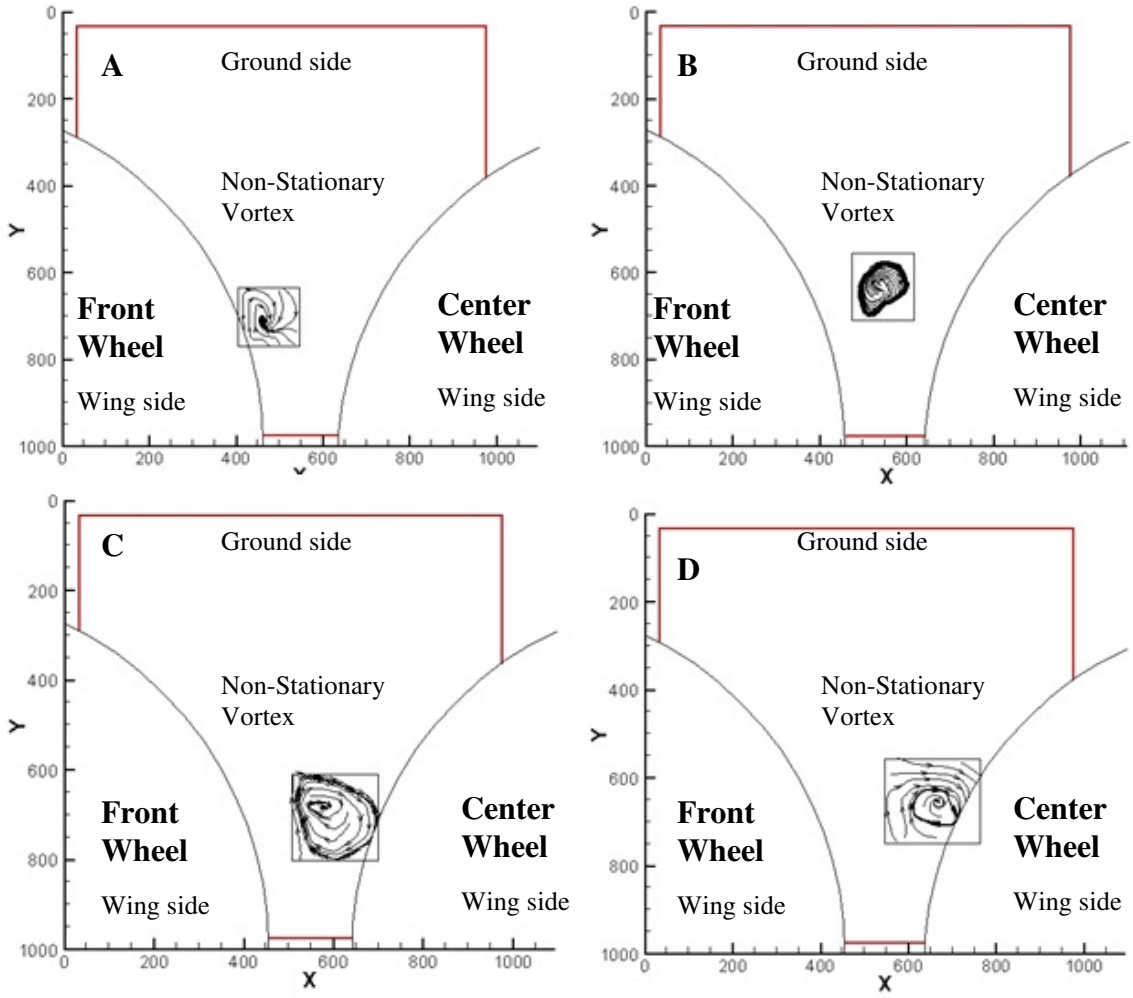

Figure 4.44: Non-Stationary Instantaneous Vortex at Different Locations Between the Wheels as seen in 'Vertical Plane Wheels View' (3.5- by 3.5-inch Window)

Figure 4.45 shows a contour map of the mean vorticity field in the mid-plane of wheels presented by Lazos [10-12] which was compared with the mean vorticity calculated from 300 samples acquired at the VT-SWT (Figure 4.46). The vortex roll-up, attachment and separation zones are similar even with differences in tunnel dimensions and free-stream velocities.

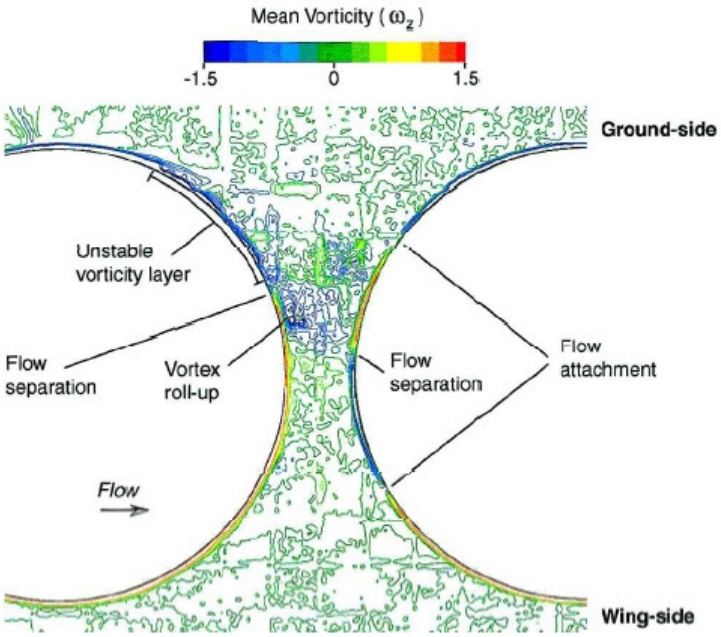

Figure 4.45: Mean Vorticity Field in the Mid-Plane of Wheels from Lazos (NASA Langley, 2002)

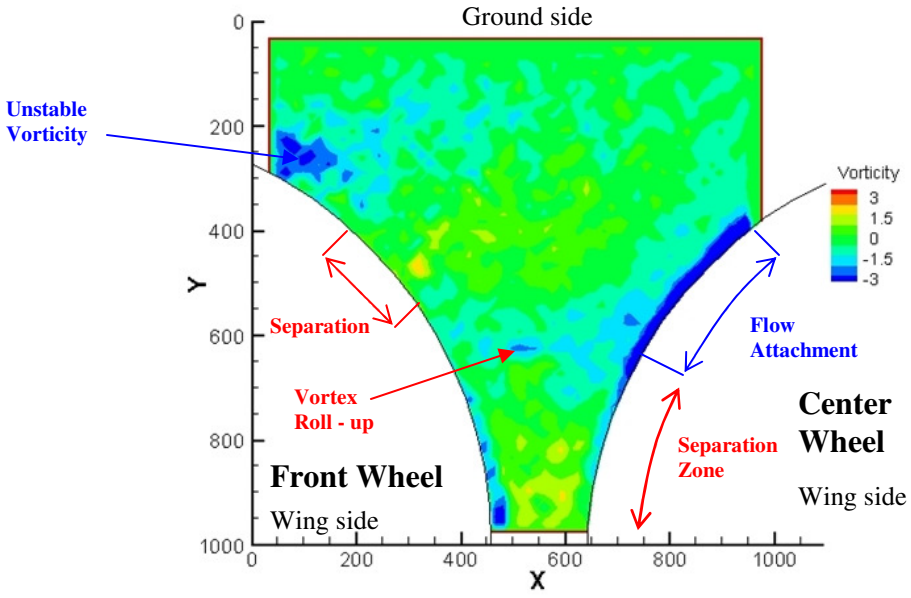

Figure 4.46: Mean Vorticity Calculated from 300 Instantaneous Samples of 'Vertical Plane Wheels View' (VT-SWT Data)

Figure 4.47 shows average velocity contours with streamlines in the 3.5- by 3.5-inch 'Back Wheel Vertical View' measurement plane. The 1000- by 1000-pixels image plane is vertical in the direction of the flow and the truck angle during acquisition was zero degrees. The free-stream flow was from left to right in the x-direction. The flow over the

back wheel curves over the aft of the wheel and flows towards the wing side. Streamline tracing points out to the region of onset of separation which was also noticed in flow visualization using tuft over the back wheel (even though the truck angle was different). A small part of the image (blanked out in white) had laser reflections from the tunnel walls and resulted in loss of correlations.

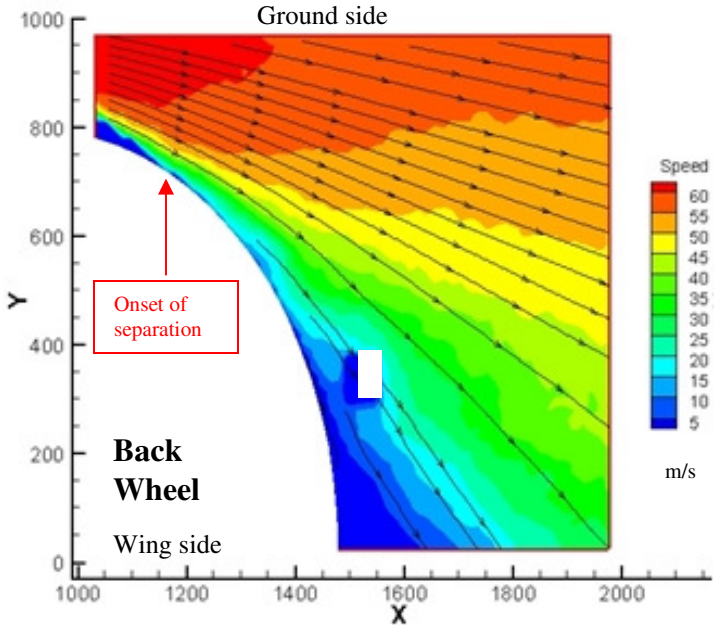

Figure 4.47: Average Velocity Contours (with Streamlines) and Average Velocity Vectors for 'Back Wheel View Vertical Plane' (3.5- by 3.5-inch Window)

Figure 4.48 shows the root mean square velocities in the u and the v-direction calculated over 300 samples. The results are similar to those presented by Lazos [10-12]. The region of flow separation is characterized by velocity fluctuation (high mean square values) which can be noticed in Figure 4.48 and seen to match with the region marked in Figure 4.47.

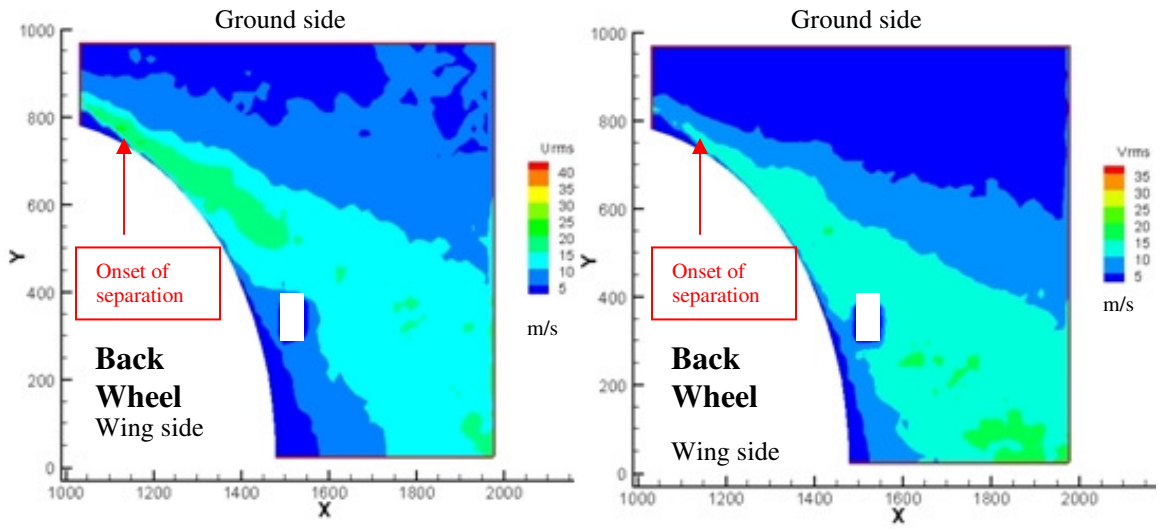

Figure 4.48: Root Mean Square Velocity contours calculated from 300 samples. U_{RMS} (left) and V_{RMS} (right) for 'Back Wheel View Vertical Plane' (3.5- by 3.5-inch Window)

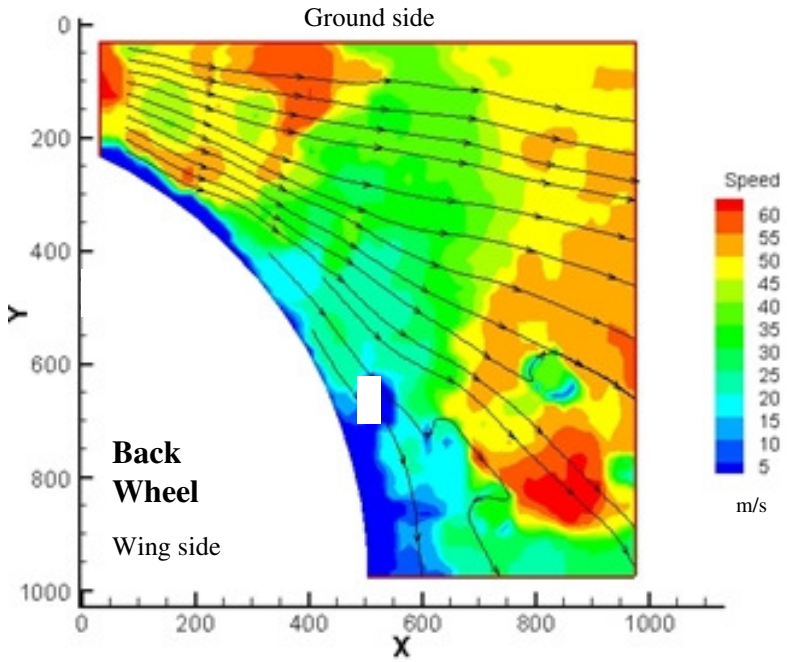

Figure 4.49: Instantaneous Velocity Contours (with Streamlines) for 'Back Wheel View Vertical Plane' (3.5- by 3.5-inch Window)

Figures 4.49 and 4.50 show instantaneous velocity contour map and velocity vector map respectively for 'Back Wheel View Vertical Plane'.

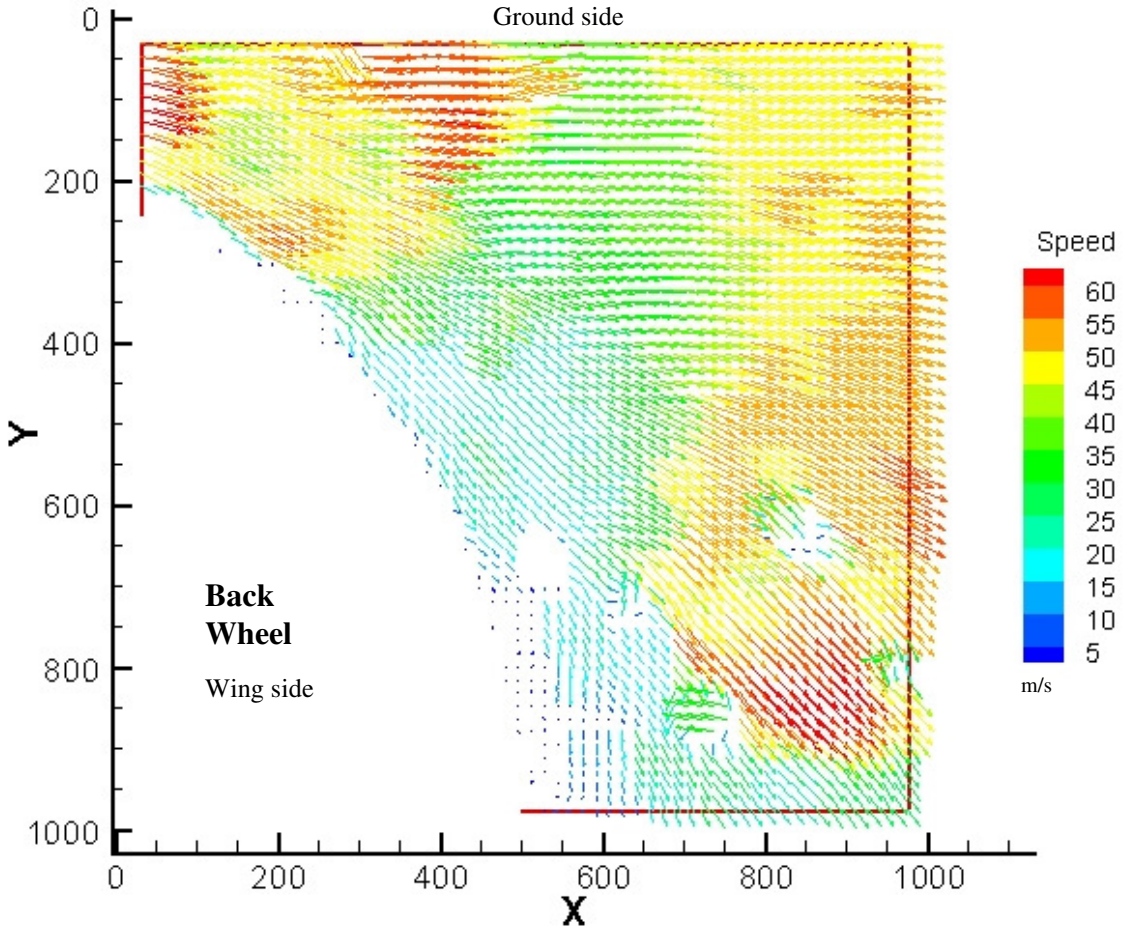

Figure 4.50: Instantaneous Velocity Vectors for 'Back Wheel View Vertical Plane' (3.5- by 3.5-inch Window)

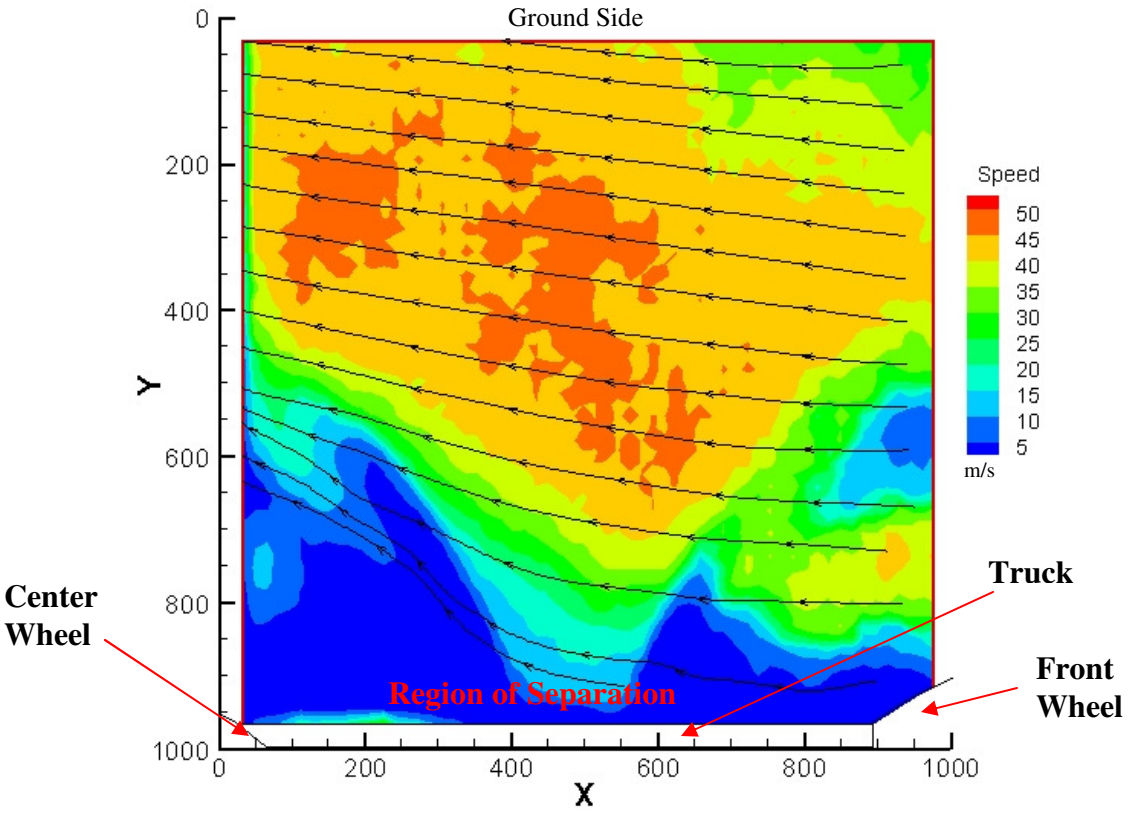

Figure 4.51: Average Velocity Contours (with Streamlines) and Average Velocity Vectors for 'Inclined Plane 13 Degrees Front' (3.5- by 3.5-inch Window)

Figure 4.51 shows a contour map of average velocity for 300 sample image pairs of 'Inclined Plane 13 Degrees Front'. The 3.5- by 3.5- inch plane is inclined at an angle of 13 degrees to the vertical and is in the truck between the first and the second wheels (shown in Figures 2.23-2.25). The front and center wheels along with the truck are marked in Figure 4.51 while the free-stream velocity is from right to left. The average velocity plot shows regions of low velocity near the truck and regions of high velocity towards the ground. The streamline tracing method shows region of separation close to the truck (as streamlines move away from the truck). The instantaneous contour and vector plots can be seen in Figures 4.53 and 4.54 respectively. Figure 4.52 shows a contour plot of the root mean square of the velocities (U_{RMS} and V_{RMS}) calculated using 300 samples.

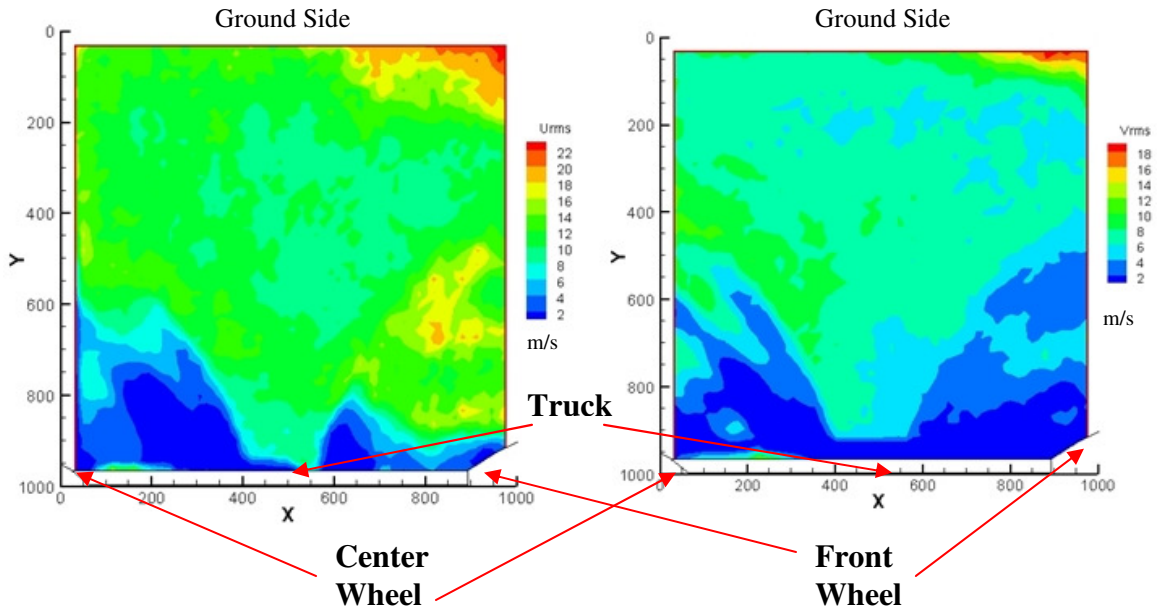

Figure 4.52: Root Mean Square Velocity contours calculated from 300 samples. U_{RMS} (left) and V_{RMS} (right) for 'Inclined Plane 13 Degrees Front' (3.5- by 3.5-inch Window)

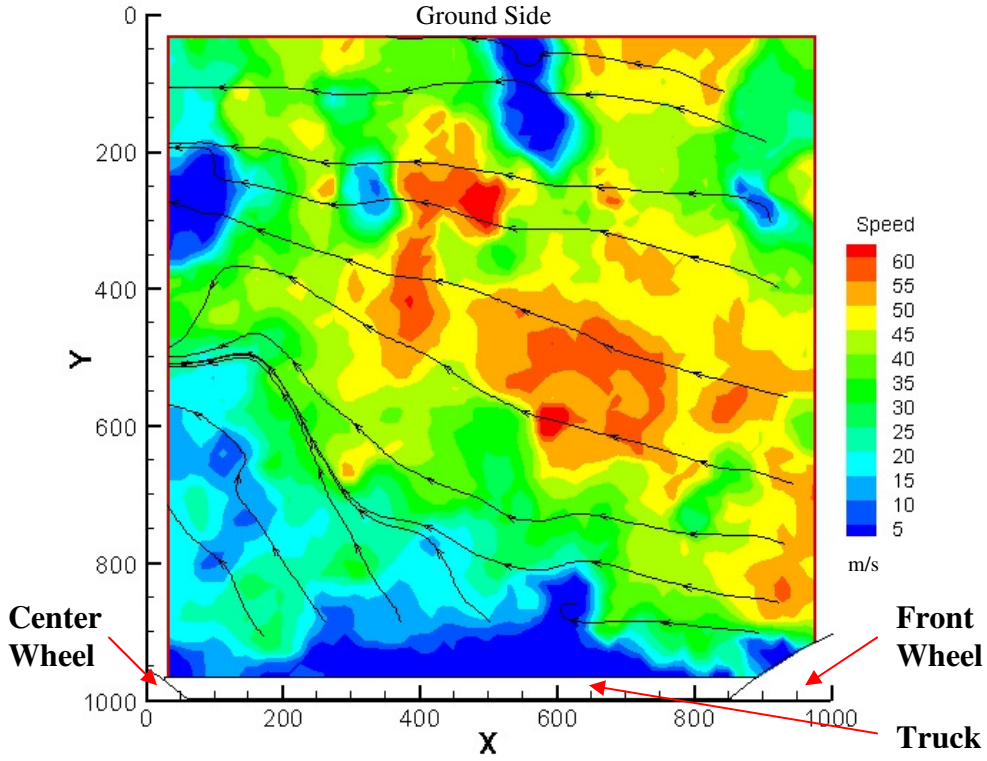

Figure 4.53: Instantaneous Velocity Contours (with Streamlines) for 'Inclined Plane 13 Degrees Front' (3.5- by 3.5-inch Window)

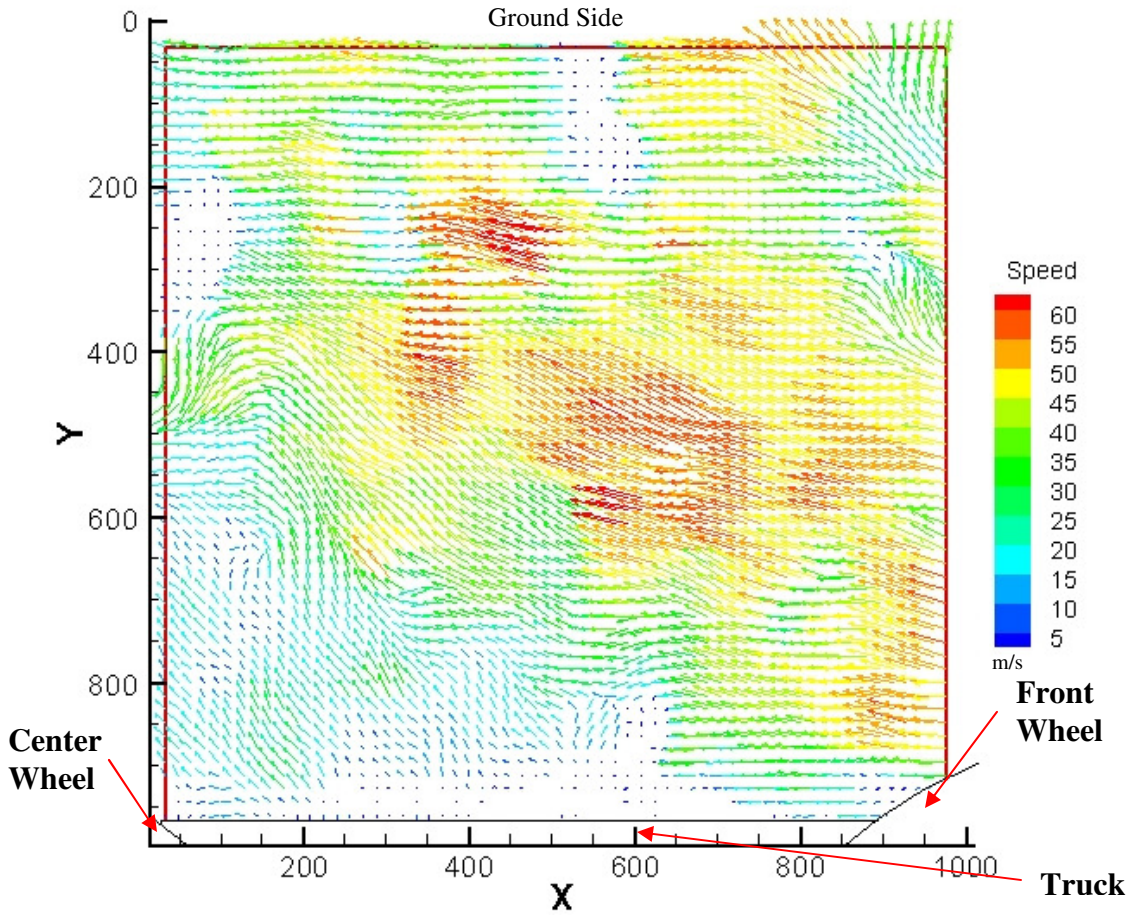

Figure 4.54: Instantaneous Velocity Vectors for 'Inclined Plane 13 Degrees Front' (3.5- by 3.5-inch Window)

Figure 4.55 shows a contour map of average velocity from 300 instantaneous samples for 'View from Top'. The free-stream flow was fro the top to the bottom. The 3.5- by 3.5-inch measurement plane is parallel to the floor of the wind tunnel. The image shows outlines of the two front wheels which were below the measurement plane. Some regions of the measurement plane had bad correlations due to reflections or loss of seeding and were blanked out. Over all the flow seems to be steady, parallel to the wheels with some regions of high velocity and unsteadiness noticed after the wheels (at the bottom of the plot). Figure 4.56 shows the root mean square velocities calculated in the u- and v-directions from 300 samples. A Sample pair of 1000- by 1000-pixels images (correlated using double pass in the DPIV software) was used to show the instantaneous velocity contours and vectors in Figures 4.57 and 4.58 respectively.

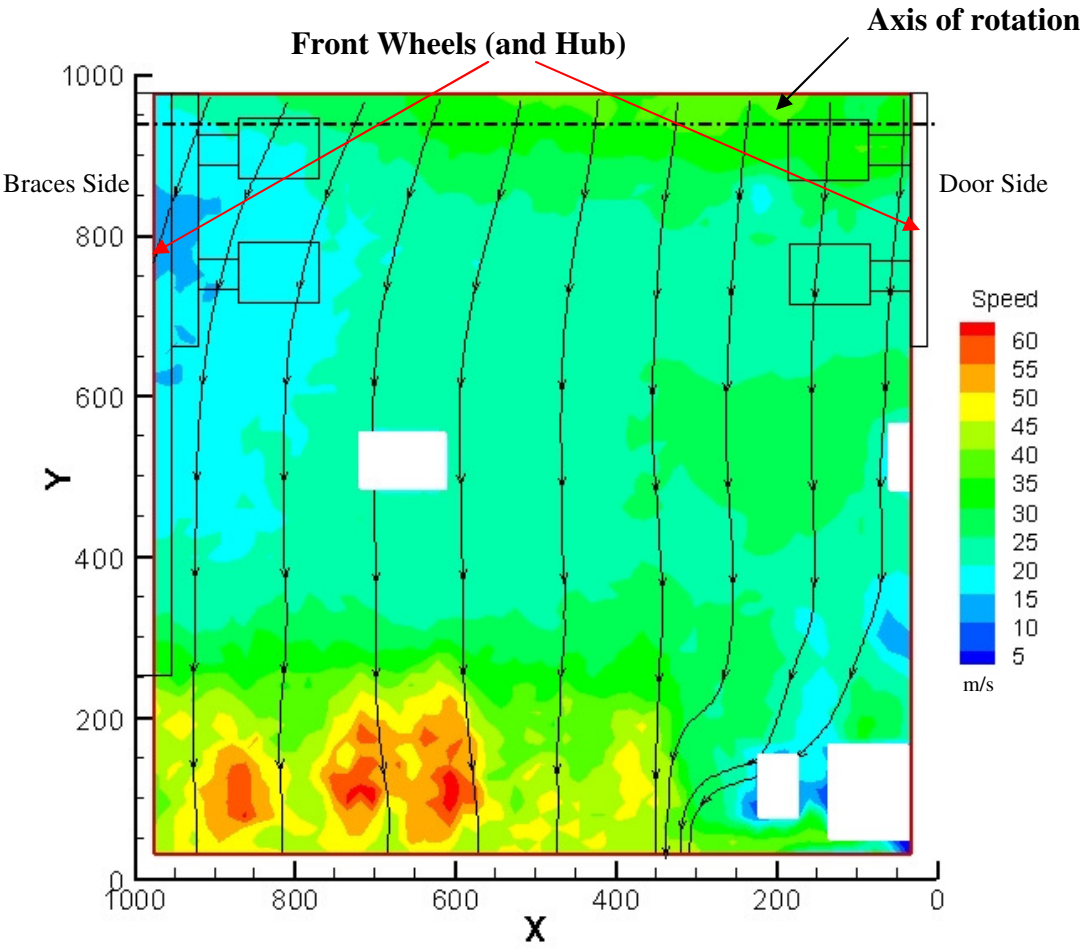

Figure 4.55: Average Velocity Contours (with Streamlines) and Average Velocity Vectors for 'View from Top' (3.5- by 3.5-inch Window)

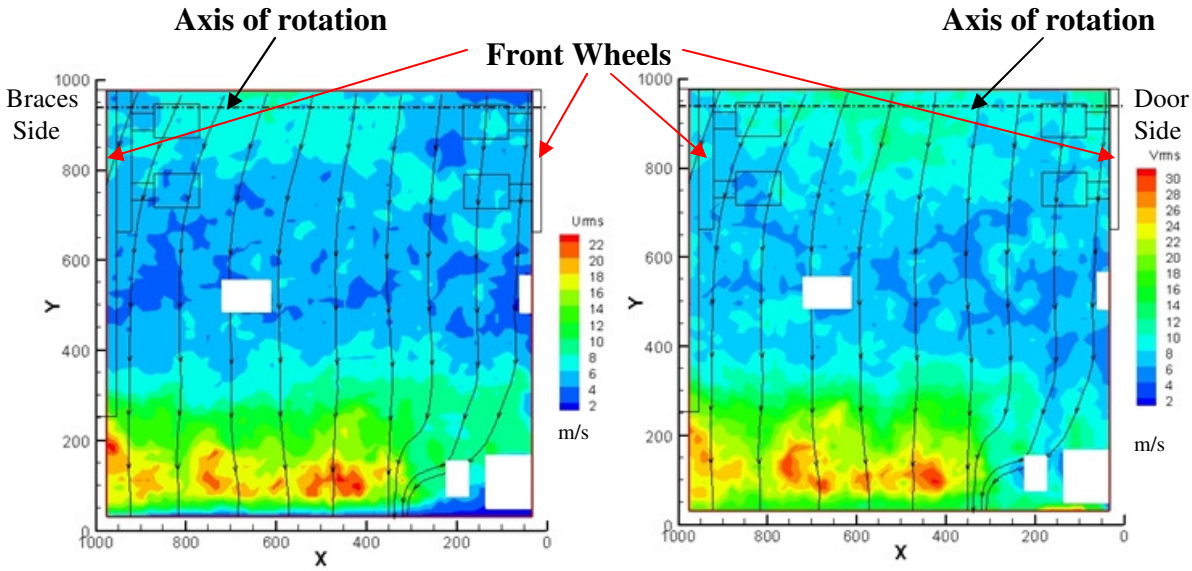

Figure 4.56: Root Mean Square Velocity contours calculated from 300 samples. U_{RMS} (left) and V_{RMS} (right) for 'View from Top' (3.5- by 3.5-inch Window)

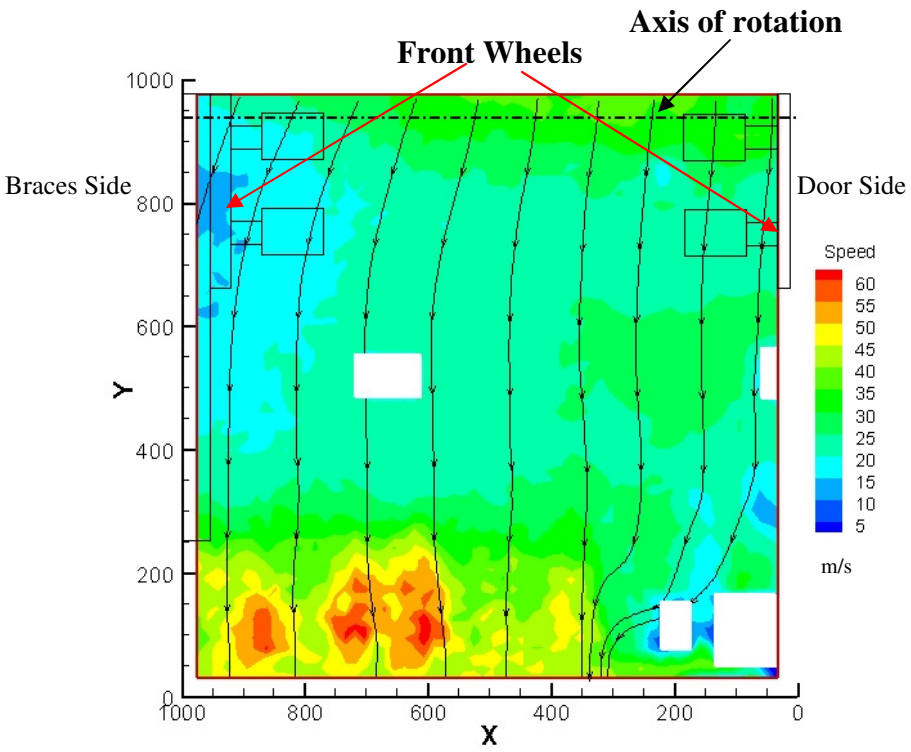

Figure 4.57: Instantaneous Velocity Contours (with Streamlines) for 'View from Top' (3.5- by 3.5-inch Window)

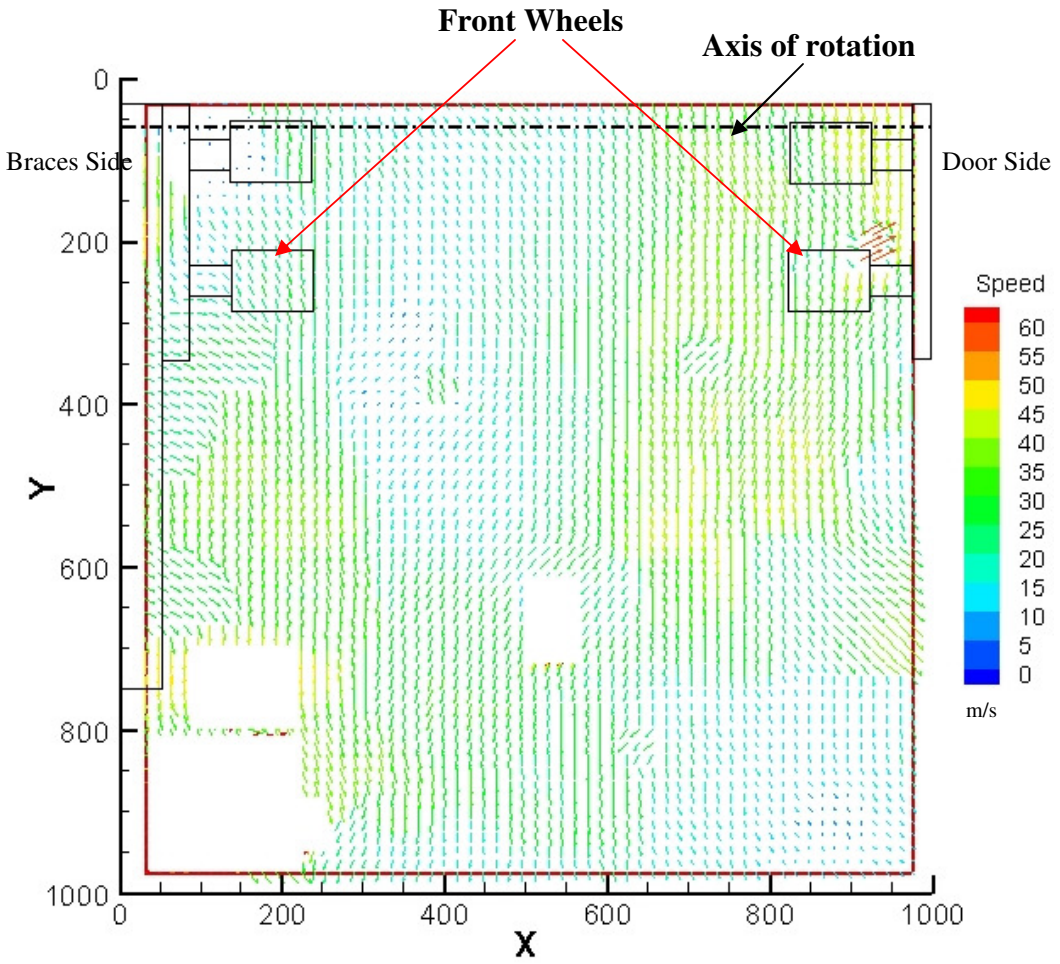

Figure 4.58: Instantaneous Velocity Vectors for 'View from Top' (3.5- by 3.5-inch Window)

4.2 Conclusions

Aerodynamic measurements were taken over an isolated 777 main landing gear in the VT-SWT. The results from hot-film and Pitot-static pressure measurements were compared between 'Baseline' and 'NCD' configurations and between the 'Baseline' configuration and the NASA Ames study conducted by Horne et al. The new technique developed here was used to process hot-film measurements as acoustic data. PIV measurements taken at six different locations over the landing gear were also presented. Flow visualization using tuft was conducted and results were presented for the 'Baseline' configuration. The following conclusions can be drawn from this study.

I. Contours of normalized wake velocity and normalized total pressure loss for the high fidelity baseline landing gear compare extremely well with the NASA Ames study given the differences in the tunnel dimensions and free-stream velocity. Contours of turbulence intensity show similar maximum turbulence levels but differences in shape. The hot-film results obtained here at VT were in good agreement with the Pitot-static measurements and flow visualization using tuft.

II. Comparisons of the normalized wake velocity, the normalized total pressure loss and the turbulence intensity between 'Baseline' and 'NCD' configurations shows that behind the braces noise control devices there was an increase in flow velocity, decrease in turbulence intensity and a decrease in the total normalized pressure loss. This means that the braces noise control device was responsible for streamlining the flow and eliminating the wake interaction between the front and the back braces. No significant effect was noticed in the contours behind the truck noise control devices between 'Baseline' and 'NCD' configurations. There was an increase in the pressure loss and a decrease in the wake velocity behind the main strut and the door between 'Baseline' and 'NCD' configurations.

III. Turbulence in frequency domain from hot-film measurements were broken into $1/12^{th}$ octave bands to be processed as acoustic data. The microphone phased

array measurements (acquired by Ravetta, [9]) were compared to hot-film measurements, behind the braces noise control devices region there was a decrease in turbulence (velocity) spectra levels of 4dB over the entire frequency range. The reduction could not be directly correlated to the MPA results since the scanning grid was 64 inches downstream of the gear. The turbulence cascade effect explained by Hinze [19] led to the loss of shedding frequency history since the turbulent field at the measurement plane was diffuse.

IV. Particle Image Velocimetry measurements taken for 'Large View between Braces' and 'Vertical Plane Close View' measurement planes show vortices shed from the front brace which collapse on the back brace. This wake interaction, responsible for higher noise levels was eliminated by using the braces noise control device. PIV measurements taken over the wheels of the landing gear for 'Vertical Plane Wheels View' were similar to results obtained by Lazos [10-12].

V. Flow visualization using tufts were analyzed for the 'Baseline' configuration. The flow over the wheels shows regions of separation on the wing side of the wheels. This result was validated in the turbulence intensity contours which show higher turbulence intensity on the wing side of the landing gear wheels as compared to the ground side.

VI. Flow visualization of the gear door showed regions of high flow turning at the mid and back-end sections. High turbulence region was noticed in the turbulence intensity measurements behind the door acquired 64 inches downstream of the landing gear.

VII. Flow visualization of the braces showed highly turbulent wake and vortices shed from the front brace collapse on the back brace. The complex, non-aerodynamic shape of the braces led to flow being separated. Also, flow visualization of the truck showed regions of higher turbulence (and hence separation) at the brakes

and axles for all the wheels and regions of lower turbulence (unsteadiness) in the center of the truck.

VIII. Flow visualization performed underneath the wheels on the main strut, the cable harness and the torque link showed little separation (lower turbulence) before the main strut (on the cable harness) but higher turbulence behind the main strut. This agreed with the tests performed on the low fidelity landing gear at NASA Ames by Horne et al. [7] which concluded that the main strut was the biggest contributor of the wake profile of the gear. The flow over the top part (ground side) of the front brace and the top trailing edge (ground side) of the door was noticed to curl and mix with the wake of the main strut under the truck.

References

[1] Delfs, J., and Heller, H. H., "Aeroacoustic Research in Europe Highlights,"*Aerospace Science and Technology*, Vol.2, No. 2, 1998, pp.145–154.

[2] Heller, H. H., and Dobrzynski, W. M., "A Comprehensive Review of Airframe Noise Research," *Proceedings of the 11th Congress of the International Council of the Aeronautical Sciences (ICAS)*, Vol. 1, edited by J. Singer and R. Staufenbiel, International Council of the Aeronautical Sciences, Lisbon, 1978, pp. 42–60.

[3] Heller, H. H., and Dobrzynski,W.M., "Unsteady Surface Pressure Characteristics on Aircraft Components and Far field Radiated Airframe Noise," AIAA Paper 77-1295, Oct. 1977.

[4] Heller, H. H., and Dobrzynski, W. M., "Sound Radiation from Aircraft Wheel-Well/Landing Gear Configurations," *Journal of Aircraft*, Vol. 14, No. 8, 1977, pp. 768–774.

[5] Heller, H. H., and Dobrzynski, W. M., "Airframe Noise: Recent Results from Experimental Studies on Landing Gears and High-Lift Devices," Aeroacoustics Workshop—Project SWING, Inst. of Acoustics and Speech Communication, Dresden Univ. of Technology, Dresden, Germany, Oct. 1999.

[6] Robert W. Stoker, and Rahul Sen, 'An experimental investigation of airframe noise using a model-scale Boeing 777,' *39th AIAA Aerospace Sciences Meeting & Exhibit*, January 2001, Reno, NV. AIAA 2001-0987

[7] W. Clifton Horne, Kevin D. James and Bruce L. Storms, 'Flow survey of the wake of a commercial transport main landing gear,' *8th AIAA/CEAS Aeroacoustics Conference and Exhibit*, June 2002, Breckenridge, CO. AIAA 2002-2407

[8] Patrocio Ravetta, Ricardo Burdisso and Wing F. Ng, 'Wind tunnel aeroacoustic measurements of a 26%-scale 777 main landing gear model,' *10th AIAA/CEAS Aeroacoustics Conference*, 2004. AIAA 2004-2885

[9] Patricio Ravetta, 'LORE approach for phased array measurements and noise control of landing gears,' PhD Dissertation, *Virginia Polytechnic Institute and State University*, 2005

[10] Lazos, B. S., 'Surface topology on the wheels of a generic four-wheel landing gear,' *AIAA Journal*, Vol. 40, No. 14, 2002, pp. 2402–2411.

[11] Lazos, B. S., 'Reynolds stresses around the wheels of a simplified four-wheel landing gear,' *AIAA Journal*, Vol. 42, No. 1, 2004, pp. 196–198.

[12] Lazos B.S., 'Mean flow features around the inline wheels of a four wheel landing gear,' *AIAA Journal*, Vol. 40, No. 2, 2002, pp. 193-198.

[13] Barker D B and Fourney M E, 'Measuring fluid velocities with speckle patterns,' *Opt. Lett.* 135, 1977

[14] Simpkins P G and Dudderar T D, 'Laser speckle measurements of transient Benard convection', *J. Fluid Mech.* 89 665, 1978

[15] Grousson R. and Mallick S., 'Study of flow patterns in a fluid by scattered laser light,' *Appl. Opt.* 16, 2334, 1977

[16] Raffel, Markus, Willert, Chris, Kompenhans J., 'Particle Image Velocimetry: A Practical Guide,' *Springer Verlag*, 1st ed. 1998.

[17] 'TSI IFA 100 Intelligent Flow Analyzer Instruction Manual', *TSI incorporated*, 1983

[18] Bearman P W, 'Corrections for the effect of ambient temperature drift on hot-wire measurements in incompressible flow,' *DISA Information* 11, 25-30, 1971

[19] Hinze, J. O., 'Turbulence', 2nd ed. New York, *McGraw-Hill*, 1975.

[20] Charles Lomas, 'Fundamentals of Hot Wire Anemometry', *Cambridge University Press*, Cambridge, 1986

[21] Collis DC and Williams MJ, 'Two-dimensional convection from heated wires at low Reynolds numbers,' *J Fluid Mech*, vol 6, 357–384, 1959

[22] Davies P. and Fisher M., *Proc. R. Soc.* 486-523, 1964

[23] Westerweel, J. Fundamentals of Digital Particle Image Velocimetry; Meas. Sci. Tech., 8, 1997; 1379-1392

Appendix A – Uncertainty Calculations

This section discusses measurement uncertainties from hot-film and Pitot-static pressure measurements. The primary quantities of concern were the hot-film velocity and the total and static measurements. The uncertainties associated with each of these measured and calculated values were calculated using the uncertainty analysis method presented in this section.

Total (Δ) uncertainty can be defined as the vector addition of the bias uncertainty (B) and the precision uncertainty (P). Bias uncertainty is a function of the calibration of transducers. Precision or random uncertainty is associated with the run to run variations in measurements. The Total uncertainty is determined by:

$$\Delta = \sqrt{B^2 + P^2}$$

The biased values were either supplied by the manufacturers or were calculated by using the calibration equations. The precision uncertainty was calculated by using measurements done at the same locations at similar test conditions.

Hot-wire Uncertainty Calculations:

The bias uncertainty for hot-film measurements from the 4^{th} calibration curve was calculated to be 0.48 %. The precision or random uncertainty was calculated by using six similar test conditions which comprised of four calibration runs (at Mach 0.16) and two free-stream measurements taken during the two configuration runs. The location of the hot-film probe for all the six runs was the same. The random uncertainty was calculated to be 2.5%. Thus, using the above formula the uncertainty in velocity measurements was found out to be 2.6%.

Pitot-Static Pressure Uncertainty Calculations:

The bias uncertainty from Pitot-static pressure measurements was found out using the linear calibration curve to be 0.15%. The precision or random uncertainty was calculated

using the same runs and was found out to be 3.4%. Therefore, the total uncertainty in pressure measurements was found out using the above formula to be 3.5%.

Uncertainty on velocity calculation from DPIV:

The velocity U (m/s) is computed using the formula $U = \Delta x / \Delta t / M$, where Δx is the displacement (pixels) of each interrogation region during Δt (sec), the time interval between the two exposures, and M is the magnification of the digital image relative to the object (pixels/m). The displacement in pixels is obtained by using peak locator algorithms (centroid) that finds the location of the peak on the correlation map obtained from cross-correlating the two images and corrects for various biases [23] and yields to sub-pixel accuracy (less than 0.1 pixels). The Δt is adjusted to yield typical displacements of greater than 10 pixels to yield an uncertainty of less than 1%. Values in the lower velocity regions however can have higher uncertainties due to the lower Δx. The maximum uncertainty in the Δt is calculated from the time interval between the two laser pulses. It was found that this uncertainty increases with lower laser power and with lower Δt. A conservative number for the typical PIV experiments using a Δt of 20 μs and powers around 20 mJ was found to be 1%. The magnification is measured using images of targets located in the laser sheet plane and it is read to better than 1%. Combining these three conservative measurements the uncertainty for typical displacements yields to a maximum error of less than 2%.

Appendix B – Basic Principles

B.1 Hot-wire Anemometry

For many years, hot-wire anemometer (HWA) has been used as a research tool in the field of experimental fluid mechanics for measuring turbulent flows. In spite of it being an intrusive measurement, HWA is still widely preferred over most non-intrusive velocity measurements due to recent improvements in computer technology and since it is the only instrument (used in fluid measurements) capable of delivering a truly analog output at high frequencies.

Hot-wire anemometry is based on the convective heat transfer from a heated wire or film element placed in a flow. Any change in the flow condition, affects the heat transfer from the heated element to the flow and hence the temperature of the sensor which can be detected instantly by a HWA system as a change in temperature. HWA can measure velocity, temperature, concentration changes in gaseous flows and phase changes in multi-phase flows.

The HWA system consists of a probe which has a small electrically heated wire (sensing element) exposed to flow and an anemometer (electronic circuit) which converts the sensor output to voltage. The anemometer has a direct influence on the probe characteristics (frequency response) and therefore forms an integral part of the HWA system.

B.1.1 Hot-wire and Hot-film Probes

A hot-wire (or film) probe typically consists of a short length of a fine diameter wire or film (as the sensing element) attached to two prongs which are usually made out of Stainless Steel or Nickel. Tungsten, Platinum or Platinum alloys are used as wire (sensing element) materials for most applications since they have high values of the temperature

coefficient of resistance and high enough tensile strength to stand the aerodynamic stresses at high flow velocities.

Depending upon the dimensions of the sensing element, hot-wire anemometry probes can be divided in to two types; hot-wire probes and hot-film probes. Hot-wire probe sensing elements are typically less than 5 μm in diameter. Thus, the thin wires are very fragile and but have good frequency response. Tungsten wire probes are normally used when the ambient temperature is less than 150 deg. Celsius. Platinum (or Platinum alloy) coated wires are usually used for flow measurements at higher temperatures. Hot-film probes consist of thin platinum or nickel films which are deposited on a substrate. The substrate is usually made up of quartz and the shape of the substrate dictates the shape of the sensor. For cylindrical probes the active element is usually 25-70 μm and less than 2 mm long. Figure A2.1 shows schematics of typical hot-wire and hot-film probes.

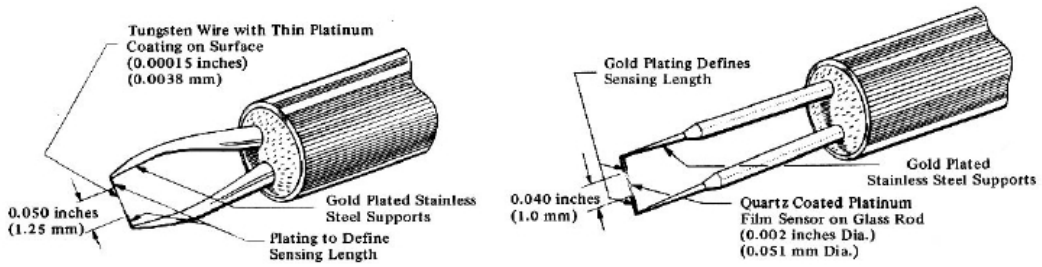

Figure B2.1: Schematic of a Hot-wire sensor (left) and a Cylindrical Hot-film Sensor (right)

A variety of hot-wire and hot-film probes are available and more can be learnt about them from the TSI IFA 100 Intelligent Flow Analyzer Instruction Manual [17].

B.1.2 Anemometer

The basic purpose of the anemometer is to detect the change in flow velocity and convert it into voltage. There are two main operating modes for a hot-wire anemometer. In constant current (CC) mode, the anemometer is responsible of providing a constant current to the probe (wire) irrespective of the flow conditions. In the more popularly used constant temperature (CT) mode, the anemometer keeps the wire temperature constant by

supplying a constant current even when the amount of heat transfer varies due to change in flow conditions. A schematic of the anemometry circuitry is shown in Figure A2.2. Lomas [20] compares both the modes of operation and discusses the advantages of working in the constant temperature mode.

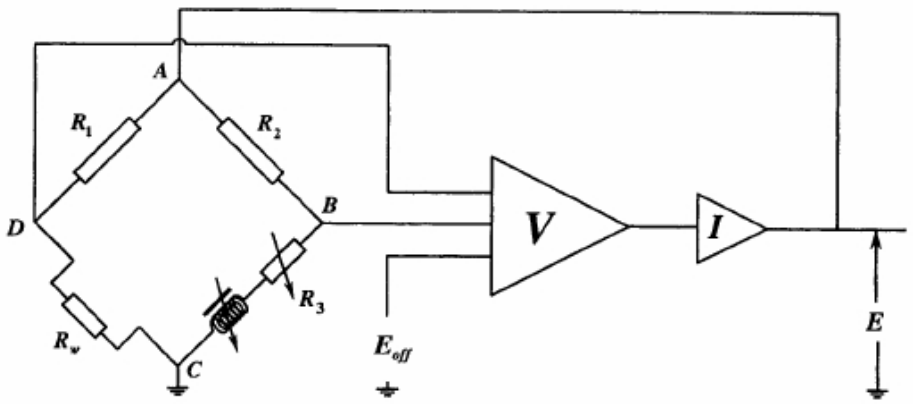

Figure B2.2: Schematic of CTA circuitry

B.1.3 Calibration

Hot-wire or hot-film probes used for turbulent measurements have to be individually calibrated before and after experiments. The calibration curve is non-linear and has higher sensitivity at low flow velocities. This has been explained by Collis and Williams [21] and Davies and Fisher [22] who discuss heat transfer from electrically heated cylinders. During calibration, the probe is held in flow while the velocity is increased in steps till the maximum expected test velocity is reached. For each flow velocity, a steady state anemometer output is recorded. Thus flow velocities and anemometer outputs are plotted against each other. Figure A2.3 shows a typical calibration curve in which a simple 4^{th} order curve fit is used. Hot-wire or hot-film probes also follow King's Law which states that the output voltage E, from an anemometer can also be expressed in the form of a simple power law given by;

$$E^2 = A + BV^n$$

Where V is the effective flow velocity and A, B and n are constants which are determined for a given probe geometry and test conditions.

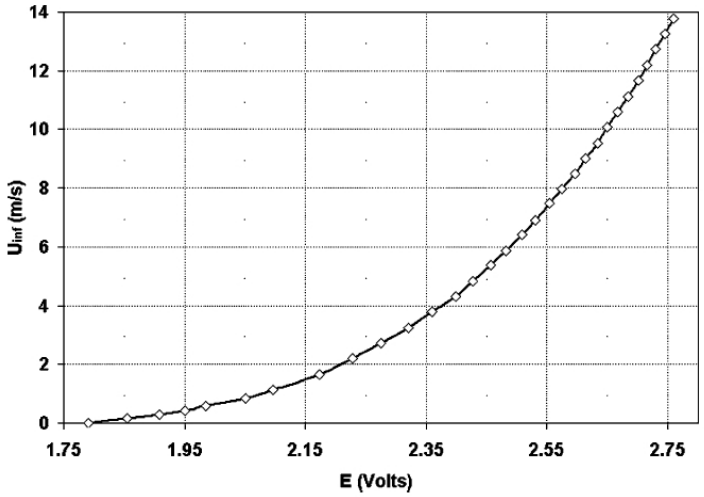

Figure B2.3: Typical 4th Order Hot-wire (film) Calibration Curve

B.2 Pitot-static Pressure Measurements:

An essential part of experimental fluid mechanics is the evaluation of pressure and velocity fields. Total and static pressures are measured to determine the magnitude and the direction of the flow velocity and the surfaces forces acting on a body. The total pressure is defined as the pressure obtained by insentropically decelerating the flow to rest. The ability of a given probe to measure velocity accurately depends on the Reynolds number, the Mach number, velocity gradients, the probe geometry and the unsteadiness of the flow.

Pitot-static probes are used to measure static and total pressures. The static pressure is measured by orifices on the cylindrical tube which is parallel to the flow and the total pressure is measured through an orifice which is located at the end of the Pitot-static tube as shown in Figure A2.4.

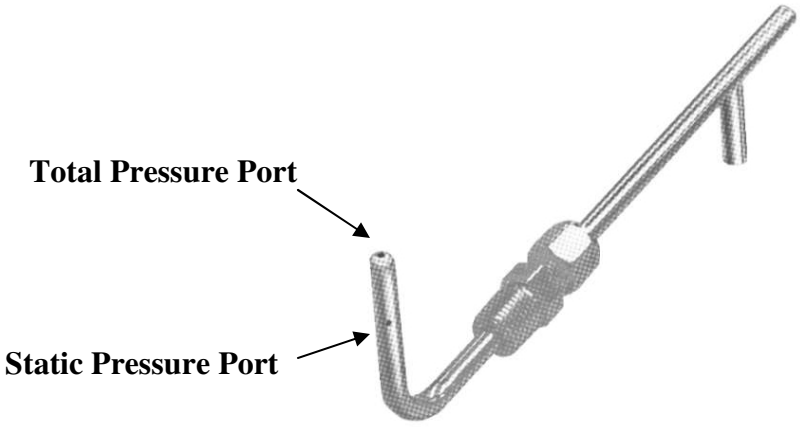

Figure B2.4: Typical Pitot-Static Probe

The probes are connected to a steady pressure transducer which converts the pressure into analog voltage. Simplest Pressure transducers consist of a diaphragm which deforms on the application of load (pressure) and an electrode that measures the deformation. One side of the diaphragm is called as the high pressure side whereas the opposing side is called as the low pressure side.

Pressure transducers can be used either in gage, absolute or differential mode. In the gage mode, the low pressure side of the transducer is kept open to atmosphere while pressure to be measured is applied to the high pressure side. In the absolute mode, the low pressure side is sealed and evacuated (vacuum) so that the diaphragm sees zero pressure on that side. During differential operation, the high pressure and low pressure sides are both connected to pressures and the net force acting on the transducer is the difference between the high pressure side and the low pressure side.

B.3 Flow Visualization

The field of flow visualization dates back to the 1400's when Leonardo da Vinci sketched images of fine particles of wood shavings which had been dropped into flowing liquid. Since then numerous techniques have been carefully developed to understand the nature of fluid flow. Recent advances in computers, digital imaging and photography have enhanced the capacity and given rise to numerous techniques. Some flow visualization

techniques currently used in the field of fluid dynamics involve the application of oil on the surfaces exposed to flow, introducing smoke in the flow upstream of the test piece, the application of tuft over the test piece, or the use of sublime chemicals or china clay over the test surfaces. In each of the above mentioned methods, the difference in the behavior (characteristics) of laminar and turbulent flow is exploited to visualize flow.

While using yarn or tuft visualization, small (about 1 to 3 inches long) pieces of thread are taped or glued to the surface of the model to be tested. The visualization can be enhanced by using fluorescent fibers, UV light or fibers soaked in UV dye and by capturing still images or digital videos. Advantages of using this method include ease of application and the ability to be used over a wide range of flow conditions (speed, position of the model, etc). Some of the disadvantages of this method include down time required to install the fibers over complex geometries and the inability to provide a detailed flow pattern since the visualization is limited to the length of the fibers.

Appendix C – 1/12th Octave Bands

Band #	Lower (Hz)	Center (Hz)	Upper (Hz)
1	1.03	1.06	1.09
2	1.09	1.12	1.16
3	1.16	1.19	1.22
4	1.22	1.26	1.30
5	1.30	1.33	1.37
6	1.37	1.41	1.46
7	1.46	1.50	1.54
8	1.54	1.59	1.63
9	1.63	1.68	1.73
10	1.73	1.78	1.83
11	1.83	1.89	1.94
12	1.94	2.00	2.06
13	2.06	2.12	2.18
14	2.18	2.24	2.31
15	2.31	2.38	2.45
16	2.45	2.52	2.59
17	2.59	2.67	2.75
18	2.75	2.83	2.91
19	2.91	3.00	3.08
20	3.08	3.17	3.27
21	3.27	3.36	3.46
22	3.46	3.56	3.67
23	3.67	3.78	3.89
24	3.89	4.00	4.12
25	4.12	4.24	4.36
26	4.36	4.49	4.62
27	4.62	4.76	4.90
28	4.90	5.04	5.19
29	5.19	5.34	5.50
30	5.50	5.66	5.82
31	5.82	5.99	6.17
32	6.17	6.35	6.54
33	6.54	6.73	6.92
34	6.92	7.13	7.34
35	7.34	7.55	7.77
36	7.77	8.00	8.23
37	8.23	8.48	8.72
38	8.72	8.98	9.24
39	9.24	9.51	9.79
40	9.79	10.08	10.37
41	10.37	10.68	10.99
42	10.99	11.31	11.65
43	11.65	11.99	12.34
44	12.34	12.70	13.07

Band #	Lower (Hz)	Center (Hz)	Upper (Hz)
45	13.07	13.45	13.85
46	13.85	14.25	14.67
47	14.67	15.10	15.54
48	15.54	16.00	16.47
49	16.47	16.95	17.45
50	17.45	17.96	18.49
51	18.49	19.03	19.58
52	19.58	20.16	20.75
53	20.75	21.36	21.98
54	21.98	22.63	23.29
55	23.29	23.97	24.68
56	24.68	25.40	26.14
57	26.14	26.91	27.70
58	27.70	28.51	29.34
59	29.34	30.20	31.09
60	31.09	32.00	32.94
61	32.94	33.90	34.90
62	34.90	35.92	36.97
63	36.97	38.05	39.17
64	39.17	40.32	41.50
65	41.50	42.72	43.97
66	43.97	45.25	46.58
67	46.58	47.95	49.35
68	49.35	50.80	52.29
69	52.29	53.82	55.39
70	55.39	57.02	58.69
71	58.69	60.41	62.18
72	62.18	64.00	65.88
73	65.88	67.81	69.79
74	69.79	71.84	73.94
75	73.94	76.11	78.34
76	78.34	80.64	83.00
77	83.00	85.43	87.93
78	87.93	90.51	93.16
79	93.16	95.89	98.70
80	98.70	101.59	104.57
81	104.57	107.64	110.79
82	110.79	114.04	117.38
83	117.38	120.82	124.36
84	124.36	128.00	131.75
85	131.75	135.61	139.59
86	139.59	143.68	147.89
87	147.89	152.22	156.68
88	156.68	161.27	166.00

Band #	Lower (Hz)	Center (Hz)	Upper (Hz)
89	166.00	170.86	175.87
90	175.87	181.02	186.32
91	186.32	191.78	197.40
92	197.40	203.19	209.14
93	209.14	215.27	221.58
94	221.58	228.07	234.75
95	234.75	241.63	248.71
96	248.71	256.00	263.50
97	263.50	271.22	279.17
98	279.17	287.35	295.77
99	295.77	304.44	313.36
100	313.36	322.54	331.99
101	331.99	341.72	351.73
102	351.73	362.04	372.65
103	372.65	383.57	394.81
104	394.81	406.38	418.28
105	418.28	430.54	443.16
106	443.16	456.14	469.51
107	469.51	483.27	497.43
108	497.43	512.00	527.01
109	527.01	542.45	558.34
110	558.34	574.70	591.54
111	591.54	608.88	626.72
112	626.72	645.08	663.99
113	663.99	683.44	703.47
114	703.47	724.08	745.30
115	745.30	767.14	789.62
116	789.62	812.75	836.57
117	836.57	861.08	886.31
118	886.31	912.29	939.02
119	939.02	966.53	994.85
120	994.85	1024.01	1054.01
121	1054.01	1084.90	1116.69
122	1116.69	1149.41	1183.09
123	1183.09	1217.76	1253.44
124	1253.44	1290.17	1327.97
125	1327.97	1366.88	1406.94
126	1406.94	1448.16	1490.60
127	1490.60	1534.28	1579.23
128	1579.23	1625.51	1673.14
129	1673.14	1722.17	1772.63
130	1772.63	1824.57	1878.04
131	1878.04	1933.07	1989.71
132	1989.71	2048.01	2108.02

Band #	Lower (Hz)	Center (Hz)	Upper (Hz)
133	2108.02	2169.79	2233.37
134	2233.37	2298.82	2366.18
135	2366.18	2435.51	2506.88
136	2506.88	2580.33	2655.94
137	2655.94	2733.77	2813.88
138	2813.88	2896.33	2981.20
139	2981.20	3068.55	3158.47
140	3158.47	3251.02	3346.28
141	3346.28	3444.33	3545.26
142	3545.26	3649.15	3756.07
143	3756.07	3866.13	3979.42
144	3979.42	4096.03	4216.05
145	4216.05	4339.59	4466.75
146	4466.75	4597.64	4732.36
147	4732.36	4871.03	5013.76
148	5013.76	5160.67	5311.89
149	5311.89	5467.54	5627.75
150	5627.75	5792.66	5962.40
151	5962.40	6137.11	6316.94
152	6316.94	6502.04	6692.56
153	6692.56	6888.67	7090.53
154	7090.53	7298.29	7512.15
155	7512.15	7732.27	7958.85
156	7958.85	8192.06	8432.10
157	8432.11	8679.18	8933.50
158	8933.50	9195.28	9464.72
159	9464.72	9742.06	10027.52
160	10027.52	10321.35	10623.79
161	10623.79	10935.09	11255.51
162	11255.51	11585.32	11924.80
163	11924.80	12274.22	12633.89
164	12633.89	13004.09	13385.14
165	13385.14	13777.35	14181.06
166	14181.06	14596.60	15024.31
167	15024.31	15464.56	15917.70
168	15917.70	16384.13	16864.22
169	16864.22	17358.38	17867.02
170	17867.02	18390.56	18929.45
171	18929.45	19484.12	20055.05
172	20055.05	20642.71	21247.59
173	21247.59	21870.19	22511.04
174	22511.04	23170.66	23849.61
175	23849.62	24548.46	25267.79
176	25267.79	26008.19	26770.29

Appendix D – Hot film and Pitot Scanning Plane and Truck and Braces Grid Locations

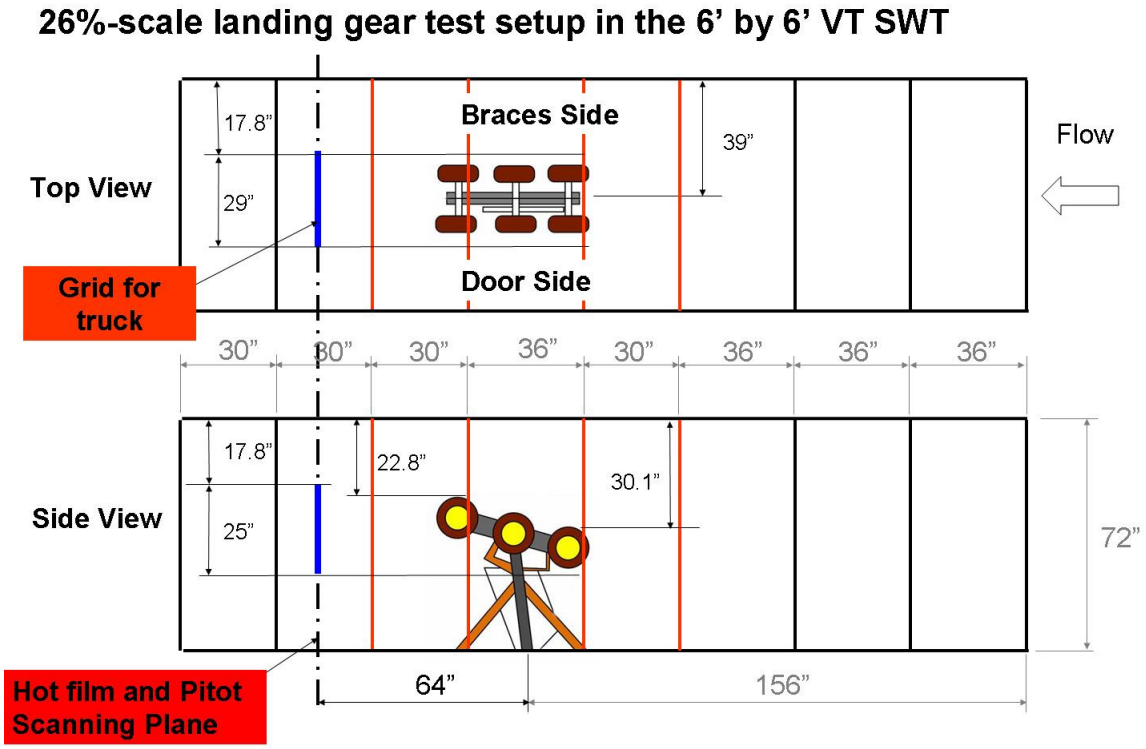

Figure D4.1: Hot film and Pitot-static Probe Scanning Plane and Grid Location for Truck NCD

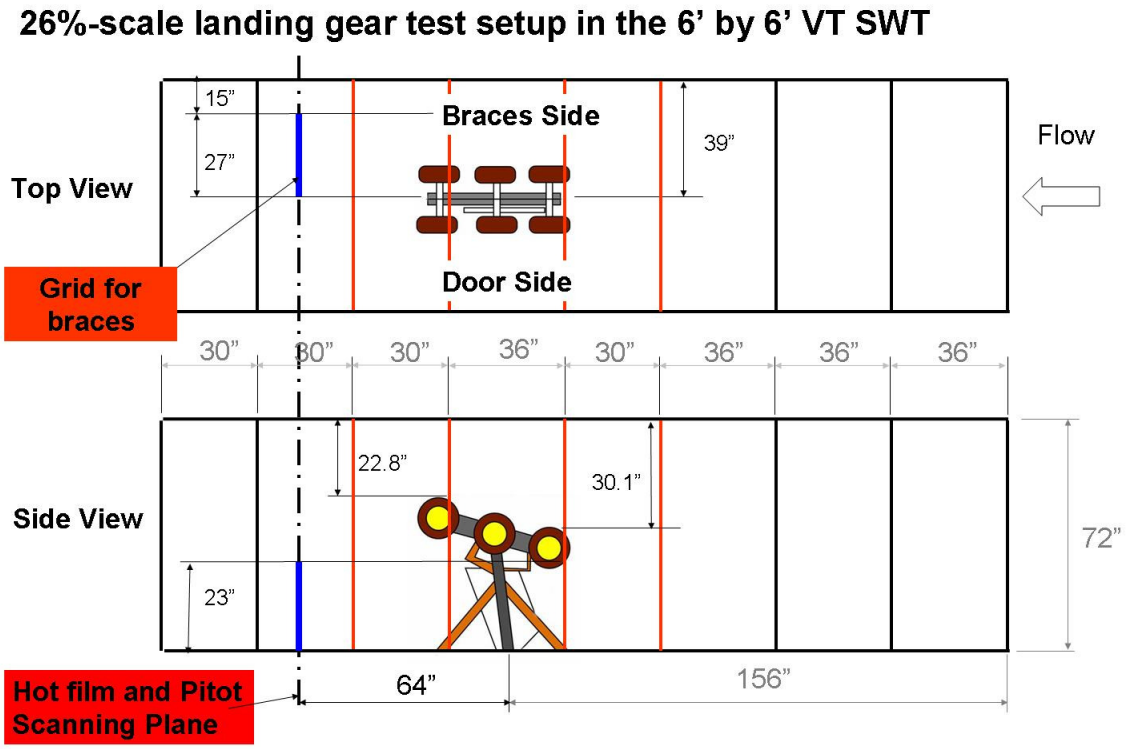

Figure D4.2: Hot film and Pitot-static Probe Scanning Plane and Grid Location for Braces NCD